UNIVERSIDADE FEDERAL DE MINAS GERAIS
Instituto de Ciências Exatas
Programa de Pós-graduação em Física

Gabriel de Albuquerque Silva

CRITICAL BEHAVIOR STUDY OF CLASSICAL FERROMAGNETIC MODELS WITH DZYALOSHINSKII-MORIYA INTERACTIONS THROUGH MONTE CARLO SIMULATIONS

Belo Horizonte
2024

Gabriel de Albuquerque Silva

CRITICAL BEHAVIOR STUDY OF CLASSICAL FERROMAGNETIC MODELS WITH DZYALOSHINSKII-MORIYA INTERACTIONS THROUGH MONTE CARLO SIMULATIONS

Tese apresentada ao Programa de Pós-Graduação em Física do Instituto de Ciências Exatas da Universidade Federal de Minas Gerais como requisito parcial para obtenção do título de Doutor em Ciências.

Orientador: João Antônio Plascak

Coorientador: David Paul Landau

Belo Horizonte
2024

Dados Internacionais de Catalogação na Publicação (CIP)

S586c Silva, Gabriel de Albuquerque.
Critical behavior study of classical ferromagnetic models with Dzyaloshinskii-Moriya interactions through Monte Carlo simulations / Gabriel de Albuquerque Silva. – 2024.
123 f. : il.

Orientador: João Antônio Plascak.
Coorientador: David Paul Landau.
Tese (doutorado) – Universidade Federal de Minas Gerais, Departamento de Física.
Bibliografia: f. 82-89.

1. Método de Monte Carlo. 2. Transições de fases. 3. Ferromagnetismo. I. Título. II. Plascak, João Antônio. III. Landau, David Paul. IV. Universidade Federal de Minas Gerais, Departamento de Física.

CDU – 531.19 (043)

Ficha catalográfica elaborada por Romário Martins Ribeiro – CRB6 3595
Biblioteca Professor Manoel Lopes de Siqueira – Departamento de Física - UFMG

UNIVERSIDADE FEDERAL DE MINAS GERAIS

INSTITUTO DE CIÊNCIAS EXATAS

PROGRAMA DE PÓS-GRADUAÇÃO EM FÍSICA

FOLHA DE APROVAÇÃO

A presente tese, intitulada **"Critical Behavior Study of Classical Ferromagnetic Models with Dzyaloshinskii-Moriya Interactions through Monte Carlo Simulations"** de autoria de **GABRIEL DE ALBUQUERQUE SILVA** submetida à Comissão Examinadora, abaixo-assinada, foi aprovada para obtenção do grau de **DOUTOR EM CIÊNCIAS**, em sete de agosto de 2024.

Belo Horizonte, 07 de agosto de 2024.

Prof. João Antônio Plascak
Orientador do estudante
Departamento de Física/UFMG

Prof. David Paul Landau
Coorientador do estudante
Universidade da Georgia

Prof. Von Braun Nascimento
Departamento de Física/UFMG

Prof. Antônio Sérgio Teixeira Pires
Departamento de Física/UFMG

Prof. Afrânio Rodrigues Pereira
Departamento de Física/UFV

Prof. Per Arne Rikvold
Universidade de Oslo

Prof. Mark Novotny
Universidade Estadual do Mississippi

Documento assinado eletronicamente por **Afranio Rodrigues Pereira**, **Usuário Externo**, em 08/08/2024, às 15:41, conforme horário oficial de Brasília, com fundamento no art. 5º do Decreto nº 10.543, de 13 de novembro de 2020.

Documento assinado eletronicamente por **Von Braun Nascimento**, **Professor do Magistério Superior**, em 08/08/2024, às 15:43, conforme horário oficial de Brasília, com fundamento no art. 5º do Decreto nº 10.543, de 13 de novembro de 2020.

Documento assinado eletronicamente por **João Antonio Plascak**, **Membro**, em 08/08/2024, às 18:14, conforme horário oficial de Brasília, com fundamento no art. 5º do Decreto nº 10.543, de 13 de novembro de 2020.

Documento assinado eletronicamente por **David Paul Landau**, **Usuário Externo**, em 08/08/2024, às 22:36, conforme horário oficial de Brasília, com fundamento no art. 5º do Decreto nº 10.543, de 13 de novembro de 2020.

Documento assinado eletronicamente por **Antonio Sergio Teixeira Pires**, **Professor do Magistério Superior**, em 12/08/2024, às 09:01, conforme horário oficial de Brasília, com fundamento no art. 5º do Decreto nº 10.543, de 13 de novembro de 2020.

Documento assinado eletronicamente por **Per Arne Rikvold**, **Usuário Externo**, em 02/09/2024, às 15:44, conforme horário oficial de Brasília, com fundamento no art. 5º do Decreto nº 10.543, de 13 de novembro de 2020.

Documento assinado eletronicamente por **Mark Alan Novotny**, **Usuário Externo**, em 09/10/2024, às 12:30, conforme horário oficial de Brasília, com fundamento no art. 5º do Decreto nº 10.543, de 13 de novembro de 2020.

A autenticidade deste documento pode ser conferida no site https://sei.ufmg.br/sei/controlador_externo.php?acao=documento_conferir&id_orgao_acesso_externo=0, informando o código verificador **3448780** e o código CRC **F4108EAF**.

Referência: Processo nº 23072.244014/2024-71 SEI nº 3448780

Acknowledgements

I would like to acknowledge Brazilian society, which is, in some sense, the main backer of the good federal teaching institutions throughout the country. Despite the country's several problems, there are also good, honest people in this very beautiful and multicultural place, who work hard every day seeking some better future for their lives.

I thank my mother Corácia, my stepfather Geraldo and my sister Gabriela, who have always helped me. They were very important so that I could dedicate and drive this work. I also thank my grandmother Maria Alves who unfortunately has passed away and left really good memories in our minds. Of course, I thank my children, Vallentina and Bernardo. They are very nice and happy kids who make home have a happy atmosphere with those children-presence traces.

I am very grateful to Professor João and Professor David for having given me the opportunity of working with them and supervising me during this work. They are excellent professionals and doctoral supervisors, as well as very kind, nice and patient. I believe that many other people who had even more contact with them, would have much more good things to say. Certainly, being supervised by these two great professors was an honor.

I acknowledge Universidade Federal de Minas Gerais (UFMG), Instituto de Ciências Exatas da UFMG and Departamento de Física for providing educational, computational and researching resources, besides a high-qualified faculty which somehow contributed to my learning. I also thank Professor Gerald for the invaluable assistance in the use of the Statistical Mechanics Computer Lab facilities at UFMG. I cannot forget the Alexander's help with extra simulations by using the resources and technical expertise from the Georgia Advanced Computing Resource Center (GACRC). I thank for this cooperation.

I am grateful to the Brazilian agencies CAPES, CNPq and FAPEMIG for their support, which was extremely important for accomplishing the present work.

Resumo

Simulações de Monte Monte Carlo (MC) foram intensivamente empregadas no estudo dos efeitos das interações de Dzyaloshinskii-Moriya (DM) nas transições de fase no modelo do rotor rígido bidimensional (2d) numa rede quadrada e no modelo de Heisenberg tridimensional (3d) numa rede cúbica simples. Ambos os modelos incluem interações de troca ferromagnética (J) e de troca DM (D) isotrópicas entre spins clássicos mais próximos. Estas interações juntas levam a uma modulação dos vetores de spin ao longo dos eixos principais da rede de maneira a depender da razão das interações $d = D/J$. Isto faz com que os vetores de spin se arranjem em uma forma *espiral*. Dependendo do valor de d, uma *incomensurabilidade* pode ocorrer nestes modelos com o uso de redes finitas com a *condição de contorno periódica* (PBC). Como consequência, não seria possível extrair resultados plausíveis de análise de escala de tamanho finito (FSS) para estimar temperaturas críticas e expoentes críticos para valores arbitrários de d. As incomensurabilidades foram solucionadas pelo uso de *condição de contorno flutuante* (FBC) e, de um novo tipo de condição de contorno, chamada *condição de contorno transladado* (SBC). Dados de energia interna e parâmetro de ordem puderam então ser obtidos das simulações de MC e usados com técnicas de histograma simples para calcular funções termodinâmicas de interesse em intervalos convenientes de temperatura. Assim, o uso da FSS na criticalidade dos modelos produziu resultados consideravelmente precisos. O modelo rotor rígido 2d com a interação DM mostrou-se equivalente ao modelo rotor rígido bidimensional puro com uma interação de troca reescalada dependente de d. Neste caso, a modulação na orientação dos spins devido à interação DM pôde ser apropriadamente revertida para recuperar o arranjo típico de spins do modelo rotor rígido bidimensional puro. O comportamento crítico do modelo é ainda ditado pela transição de fase de Berezinskii-Kosterlitz-Thouless (BKT), na qual a estrutura topológica de vórtices está presente tanto nas configurações com a modulação dos spins revertida como nas configurações espirais reais. O modelo de Heisenberg 3d com a interação DM mostrou-se passar por uma transição de fase de segunda ordem como no modelo de Heisenberg isotrópico puro. As configurações de spins mudam da fase espiral para a fase paramagnética desordenada quando a temperatura crítica é transpassada. Cálculos de fator de estrutura em uma rede cúbica simples na transição reforçam que ainda ocorre o ordenamento magnético de longo alcance dos vetores de spin, embora a classe de universalidade do modelo de Heisenberg isotrópico não permaneça mais no modelo com interação DM. No entanto, o modelo de Heisenberg com a interação DM obedece a *universalidade fraca*. Esta universalidade fraca mostrou-se ser a mesma do modelo XY.

Palavras-chave: Modelo rotor rígido 2d, Modelo de Heisenberg 3d, Interação Dzyaloshinskii-Moriya, Incomensurabilidade, Simulação de Monte Carlo, Transição de fase.

Abstract

Monte Carlo (MC) simulations were intensively employed in the study of the effects of Dzyaloshinskii-Moriya (DM) interactions on phase transitions in the two-dimensional (2d) planar rotator model on a square lattice and the three-dimensional (3d) Heisenberg model on a simple cubic lattice. Both models included isotropic ferromagnetic exchange (J) and DM isotropic exchange (D) interactions between nearest-neighbor classical spins. These interactions together lead to a modulation of the spin vectors along the principal axes of the lattices in a manner that depends upon the ratio of the interactions $d = D/J$. This makes the spin vectors arrange themselves in a *spiral* fashion. Moreover, an *incommensurability*, depending on the value of d, may take place in these models when finite lattices are used together with the standard *periodic boundary condition* (PBC). As a consequence, no meaningful results from finite-size scaling (FSS) analyses could be extracted and FSS analyses would not be useful for estimating critical temperatures and critical exponents for arbitrary values of d. The incommensurabilities were circumvented by using both fluctuating boundary conditions (FBC) and a new type of boundary condition, *shifted boundary condition* (SBC). Internal energy and order parameter data could then be obtained from MC simulations and used with single histogram techniques to calculate thermodynamic functions of interest at convenient temperature intervals. As a result, FSS at the critical points of the models leads to quite precise results. The 2d planar rotator model with DM interactions was found to be equivalent to the pure planar rotator model with a rescaled exchange term which depended upon d. In this case, the modulation of the spin orientations caused by the DM interaction could be undone to recover the typical spin arrangement of the pure planar rotator model. As a result, the critical behavior of the model is dictated by the Berezinskii-Kosterlitz-Thouless (BKT) phase transition. The topological structure of vortices of the pure planar rotator model is present both in the configuration with the transformed modulation of the spins and in the actual spiral configuration. The 3d Heisenberg model with DM interaction was shown to undergo a second-order phase transition like the pure isotropic Heisenberg model. The spin configurations change from an ordered spiral phase into a disordered paramagnetic phase above the critical temperature. Structure factor calculations for a simple cubic lattice at the transition have additionally shown that the magnetic long-range ordering of the spin vectors does occur, although the universality class of the isotropic Heisenberg model no longer holds for the model with DM interaction. However, the Heisenberg model with DM interactions obeys *weak universality*. This weak universality class was shown to be the same as the XY model.

Keywords: 2d planar rotator model, 3d Heisenberg model, Dzyaloshinskii-Moriya interaction, Incommensurability, Monte Carlo simulation, Phase transition.

Contents

1 INTRODUCTION 10

2 TWO-DIMENSIONAL PLANAR ROTATOR MODEL WITH DM INTERACTION 16

2.1 Hamiltonian model 16

2.2 Computational methods 18

2.2.1 Monte Carlo algorithm 18

2.2.2 Boundary conditions 19

2.2.3 Simulation details 21

2.2.4 Thermodynamic quantities and finite-size scaling relations 22

2.3 Results 24

2.3.1 Critical temperature 24

2.3.2 Critical temperature dependence on DM interaction 28

2.3.3 Critical exponent η 30

2.3.4 Effect of the DM interactions on the configurations 33

2.3.5 Boundary condition analysis 40

2.4 Conclusion 44

3 THREE-DIMENSIONAL HEISENBERG MODEL WITH DM INTERACTION 47

3.1 Hamiltonian model 47

3.2 Computational methods 49

3.2.1 Monte Carlo algorithm 49

3.2.2 Boundary conditions 50

3.2.3 Simulation details 52

3.2.4 Thermodynamic quantities and finite-size scaling relations 53

3.3 Results 57

3.3.1 Critical temperature and universal fourth-order cumulant 58

3.3.2 Critical temperature dependence on DM interaction 63

3.3.3 Critical exponents 65

3.3.3.1 Critical exponent ν and β/ν ratio 65

3.3.3.2 γ/ν and α/ν ratios 67

3.3.4 Structure factor 69

3.3.5 Boundary condition analysis 74

3.4 Conclusion 77

4 GENERAL CONCLUSION 80

BIBLIOGRAPHY 82

APPENDIX 90

APPENDIX A – AVERAGES AND UNCERTAINTIES OF THE THERMODYNAMIC QUANTITIES 91

APPENDIX B – SINGLE HISTOGRAM METHOD 92

APPENDIX C – FOURTH-ORDER BINDER CUMULANT CROSSING TEMPERATURE ESTIMATE 95

ANNEX 97

ANNEX A – PUBLISHED ARTICLES 98

1 Introduction

Some materials, like magnets, exhibit a property to attract or repel each other. This occurs due to them having a nonzero magnetization in some temperature interval, for example, at room temperature for a usual magnet. They are called *ferromagnetic* (FM) materials. Other systems do not exhibit this property, unless they are exposed to some external magnetic field. In this case, while an external field is acting on them, their magnetization becomes different from zero and in the same direction of the field. They are known as *paramagnetic* materials. These are just two ubiquitous examples of a vast list of magnetic phenomena encountered in nature. One can also cite *diamagnetism*, where the induced magnetization is contrary to the magnetic field and *antiferromagnetism*, that despite having no net magnetization, the arrangements of the microscopic magnetic moments are in an antiparallel way. There is, however, an extra interesting feature which makes a fundamental difference between these types of magnetism: ferromagnetism and antiferromagnetism are originated from a *collective phenomena* due to *exchange interactions* among the magnetic moments [1–4], whereas paramagnetism and diamagnetism involve interactions of magnetic moments with the external field.[1]

Heisenberg and Dirac discovered the quantum mechanical nature responsible for these exchange interactions [2]. In particular, Heisenberg [1] showed that the exchange phenomenon is described through the Coulomb interaction together with the Pauli Exclusion Principle. An application from this discovery is a model describing the magnetism produced by localized magnetic moments[2], known as *Heisenberg model* and defined by the Hamiltonian [2–4]

$$\mathcal{H}_H = -\sum_{\langle i,j \rangle} J_{ij} \boldsymbol{S}_i \cdot \boldsymbol{S}_j, \tag{1.1}$$

where $\boldsymbol{S}_i = (S_i^x, S_i^y, S_i^z)$ is a quantum spin vector operator at a site i in an n-dimensional lattice, $\langle i, j \rangle$ specifies that the sum is taken over the interactions of nearest-neighbors sites, and J_{ij} is the *exchange term*, with $J_{ij} > 0$ for ferromagnetic and $J_{ij} < 0$ for *antiferromagnetic* (AFM) systems. When quantum effects are not as important as thermal fluctuations, the above model can be treated as a *classical model*, [3, 5, 6] with the spin vectors simply having real scalar components, i.e. $\boldsymbol{S}_i \in \mathbb{R}^3$.

In general, the exchange interactions in a real magnet are not isotropic and may depend on the crystalline directions. For example, in a three-dimensional anisotropic lattice, J_{ij} can be specified as J_{ij}^x, J_{ij}^y and J_{ij}^z, which are the *anisotropic* exchange interactions. In

[1] A brief historical review about the development of the theory for magnetic phenomena in materials can be found in reference [3].

[2] This is the case for insulator materials [2].

this case, Hamiltonian (1.1) is generalized as

$$\mathcal{H}_H = -\sum_{\langle i,j\rangle} \left(J_{ij}^x S_i^x S_j^x + J_{ij}^y S_i^y S_j^y + J_{ij}^z S_i^z S_j^z \right). \tag{1.2}$$

Of course, when $J_{ij}^x = J_{ij}^y = J_{ij}^z$, one recovers the *isotropic* case (1.1). In addition, different models are achieved according to different exchange interaction assumptions. For example, if $J_{ij}^x = J_{ij}^y = 0$ and $J_{ij}^z \neq 0$, one has the *Ising model* Hamiltonian $\mathcal{H}_I$ [7]. On the other hand, if $J_{ij}^x \neq 0$, $J_{ij}^y \neq 0$ and $J_{ij}^z = 0$, one has the anisotropic *XY model* Hamiltonian $\mathcal{H}_{XY}$ and, by still removing the z-component of the spins, one gets what is called *planar rotator model* Hamiltonian $\mathcal{H}_R$ [8–11].

The Heisenberg model and the variations presented above have succeeded in explaining ferromagnetism and antiferromagnetism of several materials. Even more, the study of a simple two-dimensional planar rotator model has revealed an unknown and new kind of spin arrangements: *vortices* and *antivortices*, [9,10] opening a new era of *topological phases* and topological phase transitions. However, some types of "weak" ferromagnetism in certain AFM materials could not be plainly explained only on the basis of the exchange interactions [12, 13]. This phenomena was initially observed when measurements of the magnetic moment of some AFM compounds indicated the presence of some residual magnetization below the critical temperature [13], as shown in Figure 1. The resulting magnetic moments when the temperature tended to zero had values considerably greater than zero, as opposed to what would be expected for usual antiferromagnets. In contrast, if these compounds exhibited some FM behavior below the critical temperature, the expected magnetic moment values in this case would be much greater than the measured ones. Without any effects from FM impurities contributing to the measurements, a plausible explanation was that the magnetization vectors of the sublattices of these antiferromagnets were not exactly antiparallel to each other, but were inclined at a small angle.

This statement would be confirmed after Dzyaloshinskii and Moriya proposed an explanation for the observed weak ferromagnetism in such antiferromagnets. Dzyaloshinskii [14] demonstrated that this weak ferromagnetism had origin from relativistic interactions rather than from the usual exchange interaction. In turn, Moriya [15] proposed a mechanism to explain the weak ferromagnetism by defining an interaction of the form $\boldsymbol{D} \cdot (\boldsymbol{S}_1 \times \boldsymbol{S}_2)$, where $\boldsymbol{D}$ is a vector. This interaction is nowadays called *Dzyaloshinskii-Moriya* (DM) interaction.

Similarly to the Heisenberg model (1.1), DM interactions can be put into a Hamiltonian formalism and, for a lattice model reads

$$\mathcal{H}_{DM} = -\sum_{\langle i,j\rangle} \boldsymbol{D}_{ij} \cdot (\boldsymbol{S}_i \times \boldsymbol{S}_j), \tag{1.3}$$

where $\boldsymbol{D}_{ij}$ is the *DM vector* for the interaction of the spin at a site i with other spin at a site j. Unlike the exchange term J_{ij}, which is symmetric under permutation of the

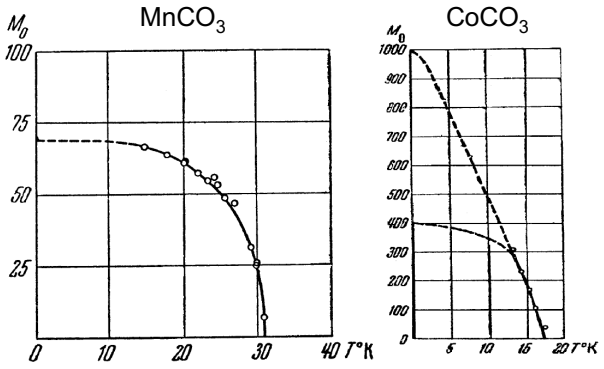

Figure 1 – Magnetic moment (emu/mole) as a function of the temperature of the two antiferromagnets indicated on the top of the corresponding graphs. At $T = 0$, the obtained magnetic moments were 68 emu/mole for the $MnCO_3$ and 400 emu/mole for the $CoCO_3$, which are much smaller than the values of magnetic moment to be expected at ferromagnetic saturation, namely 32000 emu/mole and 27200 emu/mole, respectively. (Adapated from Reference [13].)

indices i and j, the DM vector is antisymmetric, i.e. $\boldsymbol{D}_{ji} = -\boldsymbol{D}_{ij}$[3]. While the exchange interaction tends to align the spin vectors either parallel or antiparallel to each other, the DM interaction tends to align the spin vectors perpendicular to each other. Of course, the DM interaction acts as a secondary mechanism to the exchange interactions, leading to a kind of competition between them. Figure 2 shows an example of the effects of this competition on two spin vectors. For FM interaction between the spins, the addition of the DM interaction makes one of the spin vectors rotates clockwise by a certain angle ϕ. In the AFM interaction case, the DM interaction makes one of the spin vectors rotates counter-clockwise a ϕ angle. This angle depends on the ratio of the DM to the FM interaction intensities and plays a key role in models where the DM interaction is present.

Nevertheless, since the discovery of the DM interaction in antiferromagnets, they have also been observed in symmetry breaking at a surface of some materials [16], crystals with a chiral magnetic structure [17–20], and magnetic thin films in multilayers [21–24]. In these cases, different magnetic phases to the usual ferromagnetic phase can emerge, such as *helical*, *conical*, *solitons*, *spiral phases*, and even phases with more exotic spin arrangements, like *skyrmions* [24, 25].

From a theoretical point of view, a Hamiltonian combining $\mathcal{H}_H$ and $\mathcal{H}_{DM}$ above, and written as

$$\mathcal{H} = -\sum_{\langle i,j \rangle} J_{ij} \boldsymbol{S}_i \cdot \boldsymbol{S}_j - \sum_{\langle i,j \rangle} \boldsymbol{D}_{ij} \cdot (\boldsymbol{S}_i \times \boldsymbol{S}_j)\,, \tag{1.4}$$

is able to reproduce helical and spiral phases and, by adding to this equation an extra term when there is an external magnetic field (*Zeeman* interaction), conical, solitons and skyrmions phases can also arise, besides induced ferromagnetic and paramagnetic

[3] Due to this property, the DM interaction is sometimes referred to as *antisymmetric exchange interaction*.

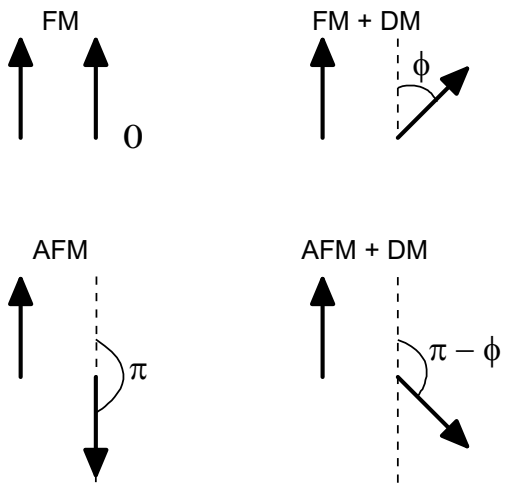

Figure 2 – A simple illustration showing the ground-state relative orientation of two nearest spin vectors according to the type of interaction between them. Top illustrations for the ferromagnetic (FM) case with and without Dzyaloshinskii-Moriya (DM) interactions. Bottom illustrations for the antiferromagnetic (AFM) case with and without DM interaction. The angle ϕ originates from the competition between the FM interaction (AFM interaction) and the DM interaction.

phases [20, 24]. The presence of each of these magnetic phases will depend, of course, on temperature and magnetic field.

The way which spins organize in any magnetic phase can cause important modifications on the electronic, thermal, elastic and optical properties [4] of the compound. In special, for some materials containing DM interactions, such modifications have shown potential applications in the technologic area. As an example, studies about skyrmions [24, 25] have suggested possibilities for use in logic devices, transistors, magnetic tunnel junctions, nano-oscillators, as microwave devices or magnonic devices, besides other applications, like quantum computing. In a broad view, thermodynamic properties, critical behavior, magnetic structures and magnetic excitations present in systems with DM interactions have been studied by theoretical approaches [26–32] as well as by Monte Carlo (MC) simulations [33–42].

Although the theoretical approaches are very important not only in trying to describe real systems, but also guide experimental and computational studies, there may be situations which they are not able to reveal some new physical mechanism or reproduce an already known one[4] [39]. Moreover, the Hamiltonian representing a model could really have complicated terms and make the theoretical treatment impracticable, mainly when there are competing interactions and they all are involved in a phase transition [6]. In this sense, MC simulations can be a powerful tool to deal with such theoretically unsolvable situations.

[4] It could happen the model itself is not appropriate for describing the experiment or the model is appropriate but has been solved too approximately [4].

As mentioned previously, the studies by MC simulations have covered several important points about models based on the Hamiltonian (1.4), some of them including additional terms, like interactions due to anisotropies and crystal asymmetries. Despite the purposes of each of these studies, detailed finite-size scaling (FSS) analyses in these models have not been considered, so often, in order to determine their critical quantities in the thermodynamic limit regime. Furthermore, FSS analysis allows verifying whether the DM interaction could change the universality class into a new one or to any other already known universality class, which has also been another little explored point. However, an *incommensurability* due to the presence of DM interactions may take place in the model when finite lattices are used together with the standard *periodic boundary condition* (PBC) [42]. This can prevent FSS analysis from providing any meaningful results.

To give an idea what this incommensurability is, Equation (1.4) will be assumed having isotropic FM interactions and isotropic DM interactions. The competition between these interactions will cause a modulation of the spin vectors along the lattice lengths according to the value of the ratio of the DM to the FM interaction intensities at low temperatures. The incommensurability will be defined as a mismatch between integer multiples of the modulation length and the lattice size. Conversely, a match in place of mismatch will be defined as *commensurability*. In the incommensurability, PBC induces frustration of the spin alignments at the borders of the finite lattice and the energy of the system turns out to be significantly enhanced [42]. To eliminate this problem, a different boundary condition, called *fluctuating boundary condition* (FBC) [43], have been used in the MC simulations [42]. It has enabled to do FSS analysis correctly and provide good results for the critical behavior in the cases where there is incommensurability.

The purpose of this work is to study the classical Heisenberg model with DM interactions described by the Hamiltonian (1.4) through Monte Carlo simulations and provide results related to its critical behavior and universality class of the phase transitions. Two different cases will be considered, namely the two-dimensional planar rotator model and the three-dimensional Heisenberg model, both of them with DM interactions. This work will be mainly concerned in estimating critical temperatures and critical exponents, which will be computed in the thermodynamic limit through FSS analysis. As pointed out, in order to make the FSS analyses useful, the incommensurability problem should require the necessity of a special attention with respect to the boundary conditions, when arbitrary values of ratio of the DM to the FM interaction intensities are considered in the simulations. This is a fact which has not been observed in the other works, except in reference [42]. By adopting the approach of this reference as the starting point, the application of FBC and its consequences will be studied in more detail. The phase diagram will be obtained over a wide range of the DM interaction strength, including the limiting case with only DM interaction in the model. The universality class of the models will also be analyzed for both models.

The plan of this thesis is as follows. In the next chapter, the two-dimensional planar rotator model with DM interactions will be studied. The phase diagram and the character of the topological phase transition will be analyzed. Chapter 3 will discuss the three-dimensional Heisenberg model with DM interactions. In this case, the universality class of the second-order phase transition will be addressed. In the last chapter, some conclusions and future works will be presented. The Appendices are devoted to some more technical aspects of obtaining the averages, uncertainties, and extrapolations from single histograms procedures.

2 Two-dimensional planar rotator model with DM interaction

2.1 Hamiltonian model

The two-dimensional planar rotator model, also referred to as two-dimensional XY model in the literature (with no z-spin component), is considered here as a classical system. It is defined on a square lattice where at each site there is a spin vector, given by $\boldsymbol{S}_i = S(\cos\varphi_i, \sin\varphi_i)$, where i labels the sites of the lattice. In this case, $\boldsymbol{S}_i$ is represented in polar coordinates, where S corresponds to the spin magnitude and φ_i to the polar angle. By using these definitions in the Hamiltonian $\mathcal{H}_H$ in Equation (1.2), with the exchange terms $J^x = J^y = J \neq 0$, the Hamiltonian $\mathcal{H}_R$ of planar rotator model can be written as [10]

$$\mathcal{H}_R = -JS^2 \sum_{\langle i,j \rangle} \cos\left(\varphi_i - \varphi_j\right). \tag{2.1}$$

For convenience, J has been placed outside of the sum and will be set $J > 0$, i.e. FM interactions. By keeping the previous definition of $\langle i, j \rangle$ in (1.1), the sums are restricted to the interactions of nearest-neighbor sites. Applications of this model can be found in studies of real systems such as superfluidity in two dimensions [44] and in superconductor-insulator transition in two-dimensional films [45]. The above model shows an unusual phase transition, discovered by Berezinskii [8] and Kosterlitz and Thouless [9, 10], then being called *Berezinskii-Kosterlitz-Thouless* (BKT) phase transition. For temperatures below the critical temperature, the system has a mechanism described as pairs of spin vortices and antivortices tightly bonded to each other. Above the critical temperature, each vortex-antivortex pair unbinds and they move independently around the lattice. In fact, this is a topological phase transition, where topological defects (vortices) play the main role [46].

In addition to the above Hamiltonian, the Hamiltonian $\mathcal{H}_{DM}$ in Equation (1.3) is considered here in the two-dimensional planar rotator model setup. In principle, $\mathcal{H}_{DM}$ can have the DM vector interaction $\boldsymbol{D}$ with its three components different from zero. However, as the spin vectors are restricted to lie in the plane of the lattice, the only possibility is $\boldsymbol{D}$ to be defined in the perpendicular direction to the lattice, so that all the interactions are not identically equal to zero. Furthermore, homogenous DM interactions are assumed in the model, i.e. they do not change with the position in the lattice. With these assumptions, $\mathcal{H}_{DM}$ results in

$$\mathcal{H}_{DM} = DS^2 \sum_{\langle i,j \rangle} \sin\left(\varphi_i - \varphi_j\right) \tag{2.2}$$

and, similarly to $\mathcal{H}_R$ in Equation (2.1), D has been placed outside of the sum and the interactions are taken only for nearest-neighbors sites.

The final Hamiltonian shown in Equation (1.4), which is here a particular combination of $\mathcal{H}_R$ and $\mathcal{H}_{DM}$, becomes

$$\mathcal{H}(d) = -JS^2\sqrt{1+d^2}\sum_{\langle i,j\rangle}\cos\left[\varphi_i - \varphi_j - \phi(d)\right], \tag{2.3}$$

where $d = D/J$ and $\phi(d) = \tan^{-1} d$. This equation can be obtained either by using a property of a linear combination of cosine and sine functions having the same argument or using the transformation proposed in reference [47].

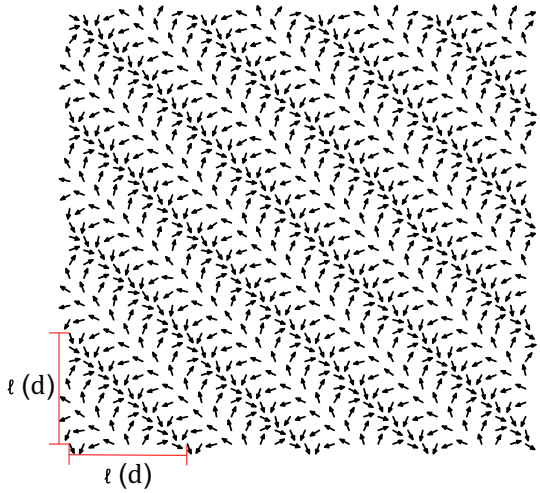

Figure 3 – A typical ground state configuration of the two-dimensional planar rotator model with DM interactions. $\ell(d)$ is the modulation length of the spin vectors. d is the ratio of the DM to the FM interaction intensities. This is a configuration for $d = 1$ with $\ell(1) = 8$.

In the ground state all the spin vectors arrange themselves in a spiral configuration in the plane of the lattice. Two adjacent spin vectors have an angular difference equal to $\phi(d)$, and one lattice spacing displacement implies in a $\phi(d)$ rotation of the next spin vector, which causes a modulation of the x- and y-spin components along the x- and y-lattice directions. In this sense, $\phi(d)$ is the *pitch angle*. Figure 3 shows how this modulation occurs in a typical ground-state configuration of the model. The modulation length $\ell(d)$ is defined as

$$\ell(d) = \frac{2\pi a}{\phi(d)}, \tag{2.4}$$

where a is the lattice spacing. As the smaller the value of d, the greater is $\ell(d)$ and, it tends to $4a$ as d tends to infinity. Here, it becomes clear that if $La/\ell(d)$, where La is a longitudinal dimension of the lattice, results in an integer number, the modulation length is commensurate with this lattice length, and incommensurate otherwise. Exactly this

possible incommensurability that requires more subtle boundary conditions when the model is simulated with DM interaction on finite lattices.

In this chapter, the model defined by the Hamiltonian (2.3) will be studied through MC simulations and FSS analyses. For convenience, the lattice spacing is set as $a = 1$ and the finite system is represented as $L \times L$ square lattices, having $N = L^2$ sites. Furthermore, in Equation (2.3) is fixed $S = 1$. The following section presents brief descriptions of the used computational methods.

2.2 Computational methods

2.2.1 Monte Carlo algorithm

A hybrid Monte Carlo algorithm was used, which combines the standard single-spin Metropolis update [48] and the Swendsen-Wang cluster-spin update [49]. The first step of the algorithm is defined by a sequential sweep of all the spins of the lattice using the standard Metropolis algorithm. A site i is chosen and its spin angle φ_i^{old} gains a little random increment $\Delta\varphi$. As shown in Equation (2.5), a new angle φ_i^{new} will be accepted if the total energy becomes smaller than the total energy for the previous angle φ_i^{old} or if the Boltzmann probability of the energy difference ΔE is greater than a random number u uniformly distributed between 0 and 1. If this last condition does not occur, the spin angle φ_i^{old} remains unchanged.

$$\varphi_i^{old} \rightarrow \varphi_i^{old} + \Delta\varphi \Rightarrow \varphi_i^{new} = \begin{cases} \varphi_i^{old} + \Delta\varphi & \text{if} \quad \Delta E < 0 \text{ or } e^{-\Delta E/(k_B T)} \geq u \\ \varphi_i^{old} & \text{if} \quad e^{-\Delta E/(k_B T)} < u \end{cases} \tag{2.5}$$

The second step consists in the Swendsen-Wang algorithm. To use this cluster algorithm in a continuous spin model, the spin angle at each site is transformed as [33]

$$\varphi_i = \varphi_i^{new} - \frac{\pi}{2}\left(1 + \sigma_i\right), \tag{2.6}$$

where to the new angle φ_i^{new}, coming from the Metropolis update, is added a second term that can be equal to 0 or π, assuming $\sigma_i = \pm 1$. This transformation makes the Hamiltonian (2.3) have an Ising-type form

$$\mathcal{H} = -\sum_{\langle i,j \rangle} J_{ij}\sigma_i\sigma_j, \tag{2.7}$$

with J_{ij} describing an effective anisotropic exchange interaction given by

$$J_{ij} = -J\sqrt{1 + d^2}\cos(\varphi_i^{new} - \varphi_j^{new} - \phi), \tag{2.8}$$

and remembering that $\phi = \tan^{-1} d$.

The Swendsen-Wang algorithm becomes then clearly applicable. For all the sites it is made $\sigma_i = 1$ and J_{ij} is assumed to be greater than zero. If J_{ij} is greater than zero, it

means that the value of σ of the neighbor is also equal to one. Then, a bond is formed with this neighbor site if its occurrence probability is greater than a random number u uniformly distributed between 0 and 1. Conversely, if J_{ij} is smaller than zero, no bond is formed. These statements are reduced in the following equation

$$bond\,(i,j) = \begin{cases} yes & \text{if} \quad J_{ij} > 0 \text{ and } 1 - e^{-2J_{ij}/(k_B T)} \geq u, \\ not & \text{if} \quad e^{-2J_{ij}/(k_B T)} < u, \end{cases} \tag{2.9}$$

which defines how to form a bond between two adjacent sites i and j in the lattice. Figure 4 provides a simple visualization for the bond of two sites.

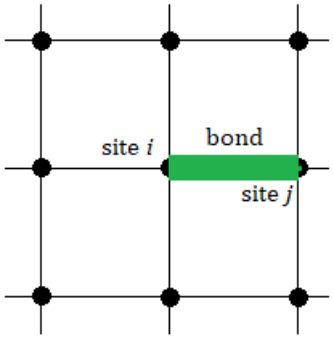

Figure 4 – Illustration of a bond between two spins (they have been omitted, for simplicity) in a portion of a square lattice as defined in the Swendsen-Wang algorithm. The bond is formed according to the prescription given by Equation (2.9). When the spins are connected to each other, they define a cluster.

The use of this procedure on all the sites defines spin clusters in the lattice, as can be seen in Figure 5. The clusters are labeled as $cluster_k$, which represents the kth cluster. Each one contains the spin angles $\varphi_{cluster_k(i)}$, where $cluster_k(i)$ keeps the site index which forms the cluster. The index i ranges according the number of spins that define the cluster. After all the clusters are constructed, they are sequentially chosen and the spin angles which they are made of, have 50% chance to rotate 180° or rely unchanged. These statements are mathematically written as

$$\varphi_{cluster_k(i)} = \begin{cases} \varphi^{new}_{cluster_k(i)} - \pi & \text{if} \quad p_{cluster_k} \geq 1/2, \\ \varphi^{new}_{cluster_k(i)} & \text{if} \quad p_{cluster_k} < 1/2, \end{cases} \tag{2.10}$$

where $p_{cluster_k}$ is again a random number uniformly distributed between 0 and 1. This finishes a lattice sweep using Swendsen-Wang algorithm.

2.2.2 Boundary conditions

As shown in Section 2.1, there is a modulation of the spin vectors having length $\ell(d) = 2\pi/\phi(d)$, which is given by Equation (2.4) with $a = 1$. In an $L \times L$ square lattice,

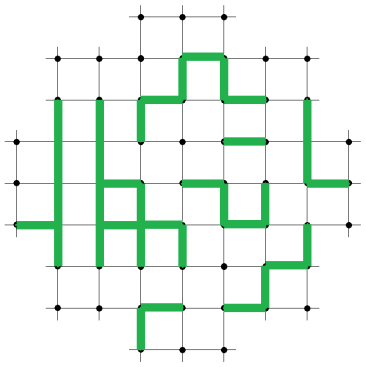

Figure 5 – An illustrative example of spin clusters, shown as green line segments. The spin vectors have been omitted. The clusters are formed in a portion of a square lattice after a lattice sweeping by using the Swendsen-Wang algorithm.

the periodic boundary condition (PBC), defined as

$$\varphi_{x,L+1} = \varphi_{x,1},\ x = 1, 2, ..., L, \tag{2.11a}$$

$$\varphi_{L+1,y} = \varphi_{1,y},\ y = 1, 2, ..., L, \tag{2.11b}$$

is used in the simulations when $L/\ell(d)$ results in an integer number. This is the case when spin structure and lattice are commensurate. Additionally, whenever $\ell(d)$ is equal to an integer number, commensurability will depend on lattice size choice. The resulting integer gives the minimum lattice size, which is the own modulation length $\ell(d)$. Then, to hold the commensurability, larger lattice sizes must be integer multiples of $\ell(d)$. Exactly for the ground state configuration, one has

$$\Delta = \sum_{i=1}^{L} (\varphi_{i,y} - \varphi_{i+1,y}) = \sum_{i=1}^{L} (\varphi_{x,i} - \varphi_{x,i+1}) = 2\pi m \Rightarrow L\phi = 2\pi m, \tag{2.12}$$

where Δ is the sum of the angular differences between two spin vectors at neighbor sites along x- or y-directions, and m is an integer number. As an example, it is assumed $d = 1$. To have commensurability, the minimum lattice size corresponds to $L = \ell(1) = 8$, leading to $\Delta = 2\pi$. On the other hand, when $\ell(d)$ is different from an integer number, implying $\Delta \neq 2\pi m$, there is an unavoidable incommensurability. Since L assumes only integer values, there are not any lattices to match the ground-state spin structure.

To match spin structure and lattice, a *phase shift angle* Δ is added to the angular differences at the boundary of the lattice as follows

$$\varphi_{x,L} - \varphi_{x,1} \to \varphi_{x,L} + \Delta - \varphi_{x,1}, \tag{2.13a}$$

$$\varphi_{L,y} - \varphi_{1,y} \to \varphi_{L,y} + \Delta - \varphi_{1,y}, \tag{2.13b}$$

with $0 \leq \Delta < 2\pi$. If the ground state configuration is the case and, restricting Δ from Equation (2.12) in $0 \leq \Delta < 2\pi$ interval, one obtains $\Delta = \mathrm{mod}\,(L\phi, 2\pi)$, where "mod" is

the modulo operation. However, this may not be valid for configurations in states with temperature greater than zero. In this case, Δ is calculated by using an extra Metropolis algorithm. Additional sweeps are performed over all sites at the boundary of the lattice and the energy variation ΔE_b after an attempt of changing the phase shift angle Δ is evaluated. Similarly to the prescription given by Equation (2.5), the phase shift angle update may be written as

$$\Delta^{old} \to \Delta^{old} + \delta \Rightarrow \Delta^{new} = \begin{cases} \Delta^{old} + \delta & \text{if} \quad \Delta E_b < 0 \text{ or } e^{-\Delta E_b/(k_B T)} \geq u, \\ \Delta^{old} & \text{if} \quad e^{-\Delta E_b/(k_B T)} < u, \end{cases} \tag{2.14}$$

where δ is a little random increment and u is a random number uniformly distributed between 0 and 1. This procedure defines the fluctuating boundary condition (FBC) [43], which is applied in the incommensurable cases.

2.2.3 Simulation details

Because of the possibility of incommensurability for finite lattices, the MC simulations were split into two types. Table 1 shows the definition of one Monte Carlo step per spin (MCS) for PBC and FBC. Both of them use a sweep in the whole lattice with Metropolis algorithm followed by one sweep with Swendsen-Wang algorithm and, for FBC, an extra sweep with Metropolis algorithm of the spin vectors of the boundary to update the phase shift angle Δ.

Table 1 – One Monte Carlo step per spin (MCS) definition according to the used boundary condition, which may be periodic (PBC) or fluctuating (FBC).

One MCS (PBC)	**One MCS (FBC)**
One sweep with Metropolis algorithm	One sweep with Metropolis algorithm
One sweep with Swendsen-Wang algorithm	One sweep with Swendsen-Wang algorithm
—	One sweep with Metropolis algorithm in the boundary

The MC simulations were performed on $L \times L$ square lattices, with L ranging from $L = 8$ to $L = 128$. The amount of discarded MCS to reach the thermal equilibrium depends on L, and ranged from 10^4 to 10^6 MCS. For larger lattices ($L \geq 64$), at least two simulations at a same temperature, but with different random number generator seeds, were performed to check whether stable configurations had been obtained in the thermal equilibrium. This was done by observing the internal energy and order parameter distributions after the simulations had finished. Then, their final configurations were used as initial configurations in other simulations at closely temperatures. This procedure decreases the amount of discarded MCS and saves computational time, besides to avoid getting stuck in meta-stable states.

Departing from stable configurations for larger lattices and random configurations for smaller lattices, one MC simulation per lattice (MCSL) has been defined as 10^7 MCS

after equilibration, with the measurements taken every 10 MCS. This jump in MCS is to reduce the correlation between the configurations in the MCS sequence [6]. When a MCSL finishes, all the measurements remain stored in a file, which consists of 10^6 rows containing energy, order parameter and phase shift angle (the latter for simulations using FBC). The random number generator of L'Ecuye was used in the simulations, implemented as the algorithm "ran2" in [50].

For finer analyses, single histogram reweighting [6] techniques were used with data from sets of MCSL performed at same values of temperature and DM interactions, but running on different processor cores and starting with different random number generator seeds. The data consist of all the generated files from all the MCSL. In this way, for any lattice, the total amount of data, e.g. energy, is equal to the number of MCSL times 10^6. A total of 50 MCSL was done for $L = 8$ and, as L increased, the number of MCSL was increased up to 300 MCSL for $L = 128$, which corresponds to the data from 3×10^8 configurations.

2.2.4 Thermodynamic quantities and finite-size scaling relations

The generated data from the MC simulations consist basically of the energy, order parameter, and the phase shift angle, as mentioned in the previous section. The energy can be calculated by using the own Hamiltonian (2.3). Normally, the order parameter in the two-dimensional planar rotator model is defined by the vectorial modulus of the magnetization per spin $\mathcal{M}$ [51, 52], which reads

$$\mathcal{M} = \frac{1}{N}\left\|\sum_{i=1}^{N} \boldsymbol{S}_i\right\|, \tag{2.15}$$

remembering that $\boldsymbol{S}_i = (\cos\varphi_i, \sin\varphi_i)$ and $N = L^2$. At $T = 0$, where all spin vectors are arranged in the ground state shown in Figure 3, $\mathcal{M}$ can be computed as a function of L and ϕ. The result is

$$\mathcal{M}(L,\phi) = \left[\frac{\sin(L\phi/2)}{L\sin(\phi/2)}\right]^2. \tag{2.16}$$

Clearly, $\mathcal{M}(L,\phi) \to 0$ as $L \to \infty$ for any finite ϕ. As $\phi \to 0$ one has $\mathcal{M}(L,\phi) \to 1$, as expected, because, in this case, one has $d = 0$ and the DM interaction is suppressed. It becomes evident that the magnetization per spin $\mathcal{M}$ does not play the role of an order parameter in the present system. Instead, a different order parameter is defined as follows

$$m = \frac{1}{N}\sqrt{\left\{\sum_{i=1}^{N}\cos\left[\varphi_i + (x_i + y_i)\phi\right]\right\}^2 + \left\{\sum_{i=1}^{N}\sin\left[\varphi_i + (x_i + y_i)\phi\right]\right\}^2}, \tag{2.17}$$

where (x_i, y_i) are the coordinates of the ith spin and $x_i, y_i \in [1, L]$. Thus, $m = 1$ in the ground state and, for finite lattices, m should decrease as the temperature increases.

The order parameter m can be used to calculate its fourth-order cumulant, as originally suggested by Binder to analyze the critical properties of the Ising model [53]. In its reduced form, the cumulant can be written as

$$U_4 = 1 - \frac{\langle m^4 \rangle}{3\langle m^2 \rangle^2}, \tag{2.18}$$

where the brackets denote a thermal average. Binder showed that, for large enough lattices, there is a *fixed point* in the U_4 curves that is independent on the system size L, and the location of this fixed point gives the transition point. In other words, the Binder cumulants are scale independent at the critical point and can also be used to determine the phase transition temperature T_c. For a planar rotator model, it is expected that the fourth-order cumulants will become equal below the BKT phase transition temperature. However, corrections to FSS are sometimes still present in the cumulant crossings for the lattice sizes at hand. When these finite-size effects happen, and when the crossings have a systematic shift with L, one can extrapolate the transition temperature in the thermodynamic limit by fitting the corresponding data to [6, 10, 42]

$$T_{cross}(L, L_s) = T_c(\infty, L_s) - \frac{C}{(\ln L)^2}, \tag{2.19}$$

where $T_{cross}(L, L_s)$ is the crossing temperature of a cumulant for a lattice size L and another cumulant for a smaller lattice size L_s. $T_c(\infty, L_s)$ is an estimate for the critical temperature of the infinite system and C a non-universal constant. The cumulant crossings can be obtained by keeping L_s fixed and taking it as a reference lattice size with $L > L_s$. Since $T_c(\infty, L_s)$ could still depend on the reference lattice size L_s, one eventually obtains the critical temperature T_c in the limit $L_s \to \infty$, namely $T_c = T_c(\infty, \infty)$.

The determination of the critical temperature allows analyzing the behavior of the order parameter at the criticality. According to the FSS theory [6, 51, 54] of the BKT critical behavior, m should have a power-law scaling behavior of the type

$$m(T \leq T_c; L) \approx \ m_T L^{-x(T)}, \tag{2.20}$$

where T_c is the BKT transition temperature, m_T a non-universal constant, and $x(T)$ a temperature dependent exponent. This scaling relation holds for all temperatures T below T_c. There is no such power-law behavior for temperatures $T > T_c$. Exactly at the transition temperature $T = T_c$ the exponent $x(T_c)$ is equal to $\eta(T_c)/2$ [10, 51], where $\eta(T_c) = 1/4$ is the corresponding spin-spin correlation function critical exponent. $\eta(T)$ decreases as the temperature decreases and goes towards zero in the $T \to 0$ limit. Thus, information about the transition can be extracted in the thermodynamic limit by FSS analysis of m.

The averages and corresponding uncertainties of most of the quantities defined above have been computed using standard procedures as described in Appendix A. The histograms technique and the analysis of their validity region are discussed in Appendix B, while the process of computing the cumulant crossings and respective error bars are presented, in some detail, in Appendix C.

2.3 Results

2.3.1 Critical temperature

The crossings of the order parameter cumulants (2.18) was used to compute the BKT transition temperature T_c for several values of the DM interaction d. This is a very convenient quantity because it is not necessary, *a priori*, the knowledge of any exponent, even when one has to use Equation (2.19). The T_c computing details will be presented here for the pure planar rotator model with $d = 0$, in order to compare the transition temperature obtained from this work with previous estimates from the literature. Then, the same procedure is extended to other d values. Here, and in the remaining of this work, the temperature T is measured in units of k_B/J.

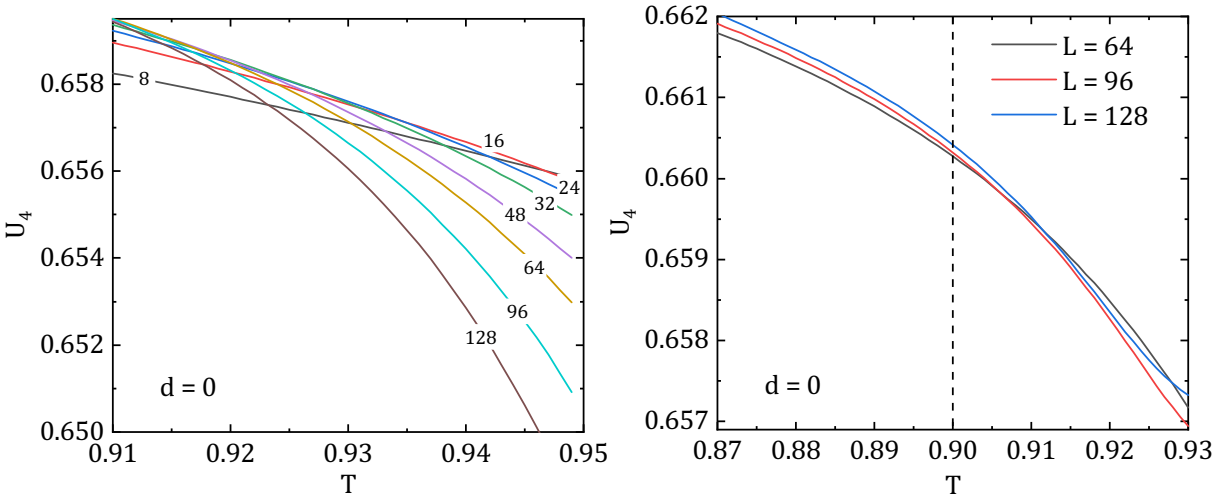

Figure 6 – On the left, the Binder cumulant U_4 of the order parameter as a function of the temperature T for different lattice sizes for the planar rotator model (i.e. $d = 0$) is shown. These are results from simulations with PBC. The lattice sizes are indicated on each curve, which were constructed by using the single histogram reweighting with data from MC simulations. In the graph on the right, only the larger lattices have been considered with new data taken at $T = 0.9$ (dashed line) and also analyzed with single histograms.

The U_4 dependence on temperature T was obtained from the single histogram reweighting to calculate the moments of the order parameter powers in Equation (2.18). The details of this technique is presented in Appendix B. A set of MCSL (definition is found in Subsection 2.2.3) are performed at a temperature T_0, with each simulation generating a file containing 10^6 rows of energy-order parameter pairs. By using these data with the single histogram reweighting, U_4 can be extrapolated from T_0 to other values of T. Figure 6 shows an application of this method for $d = 0$, where the left panel shows U_4, as function of the temperature T, for different values of the lattice size L. For $d = 0$, the order parameter definition (2.17) is, in fact, the magnetization per spin (2.15). The

data was taken at different temperatures T_0 for each lattice, with T_0 within the interval $0.91 < T_0 < 0.94$. As the lattice size increased, the amount of MCS which had to be discarded also increased (consequently, even more MCS had to be taken for the averages) in order to get reliable estimates of U_4. Then, the energy probability distribution at the crossing points (which were different from the temperature where the histograms were taken) for the larger lattices was always tested to ensure that it had not suffered any deformations when compared with the distribution at $T = T_0$. One example is given in Appendix B.

In the left panel of Figure 6 the cumulant crossings are apparently still quite dependent on the lattice sizes. However, taking as reference the minimum size $L_s = 8$, there is a clear systematic decrease in the temperature crossing $T_{cross}(L, L_s)$ as the other sizes increase from $L > 8$, making the use of Equation (2.19) quite suitable in this case. Although not clearly seen in Figure 6, the same qualitative crossings happen when the minimum lattice sizes $L_s = 16$ and $L_s = 24$ are used.

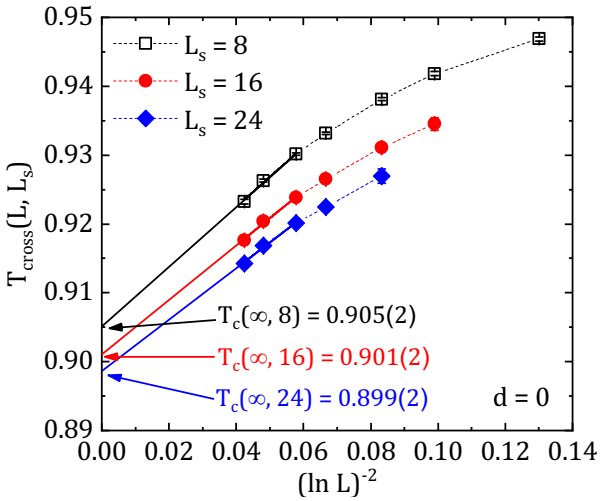

Figure 7 – Temperature of the crossings of the Binder cumulant of the order parameter $T_{cross}(L, L_s)$ as a function of different reference lattice sizes L_s when $d = 0$ (planar rotator model) using PBC. The upper, middle, and lower sets of data points correspond to crossings with $L_s = 8$, $L_s = 16$, and $L_s = 24$, respectively. The dashed lines are just guides to the eye, while the solid lines are linear fits using Equation (2.19) for lattice sizes $L \geq 64$. The extrapolated transition temperatures in the $L \to \infty$ limit, $T_c(\infty, L_s)$, are indicated by the arrows.

In fact, it would be expected the cumulants to be all the same for temperatures lower than the crossing points, since the BKT transition should always be present for any $T < T_c$. For instance, the right panel of Figure 6 shows the order parameter cumulants for the larger lattices and lower temperatures. While the cumulants still cross for $L = 64$ and $L = 96$ (this crossing value is actually compatible with the extrapolated evaluation of the BKT transition temperature, which is shown up ahead in the text), the cumulants

for $L = 96$ and $L = 128$ seem to be almost parallel in this region of temperature, a fact that can signal a possible BKT transition. For this reason, one can consider the crossing temperatures as an indication of the BKT transition T_c.

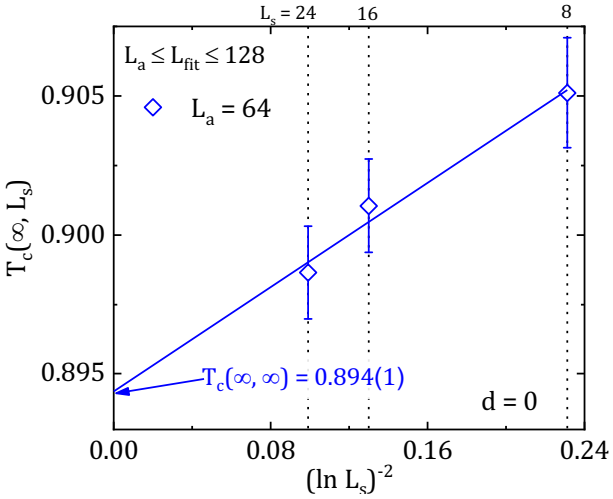

Figure 8 – Extrapolated temperature in the $L \to \infty$ limit, $T_c(\infty, L_s)$, as a function of different reference lattice sizes L_s when $d = 0$ (planar rotator model) using PBC. $T_c(\infty, L_s)$ comes from fit result for $L_s = 8$, $L_s = 16$, and $L_s = 24$, as indicated in Figure 7. The vertical dashed lines locate the reference lattice sizes L_s and the solid line is a linear fit using Equation (2.19). L_a is the smallest lattice size considered in the fit interval $L_a \leq L \leq 128$ of Figure 7. The extrapolated transition temperature in the $L_s \to \infty$ limit is indicated by the arrow, labeled as $T_c(\infty, \infty)$.

The temperatures of the cumulant crossings $T_{cross}(L, L_s)$, obtained from the data of the left panel of Figure 6, taking as reference the cumulants for $L_s = 8$, $L_s = 16$, and $L_s = 24$ are shown in Figure 7 as a function of $(\ln L)^{-2}$. The error bars of the crossings were estimated as described in the Appendix C. The size of the lattices involved in this step seem to be quite important, since in the present data the scaling regime predicted by Equation (2.19) starts to be only achieved for the lattice sizes greater than $L \geq L_a$, with the smallest size $L_a = 64$.

In addition, in the $L \to \infty$ limit, the temperature $T_c(\infty, L_s)$ resulting from each linear fit, still depends on the reference lattice size L_s. For this reason, an extra assumption can be defined about $T_s(\infty, L_s)$, by supposing that it should follow the same scaling behavior given by Equation (2.19), where this time one has $L_s \to \infty$. The result is shown in Figure 8, from which, with an additional fit, leads to $T_c(\infty, \infty) = T_c = 0.894(1)$, a value that compares very well to $T_c = 0.8935(1)$ and $T_c = 0.8935(5)$ obtained in References [55] and [56], respectively. These values are also listed in Table 2 where $T_c \equiv T_c(0)$.

Following the same procedure as above, the transition temperature can be computed for other values of the d. As an example, Figure 9 shows, on the left side, the partial results of $T_c(\infty, L_s)$ for $d = 0.5$ using FBC, $d = 1$ using PBC, and a special case where

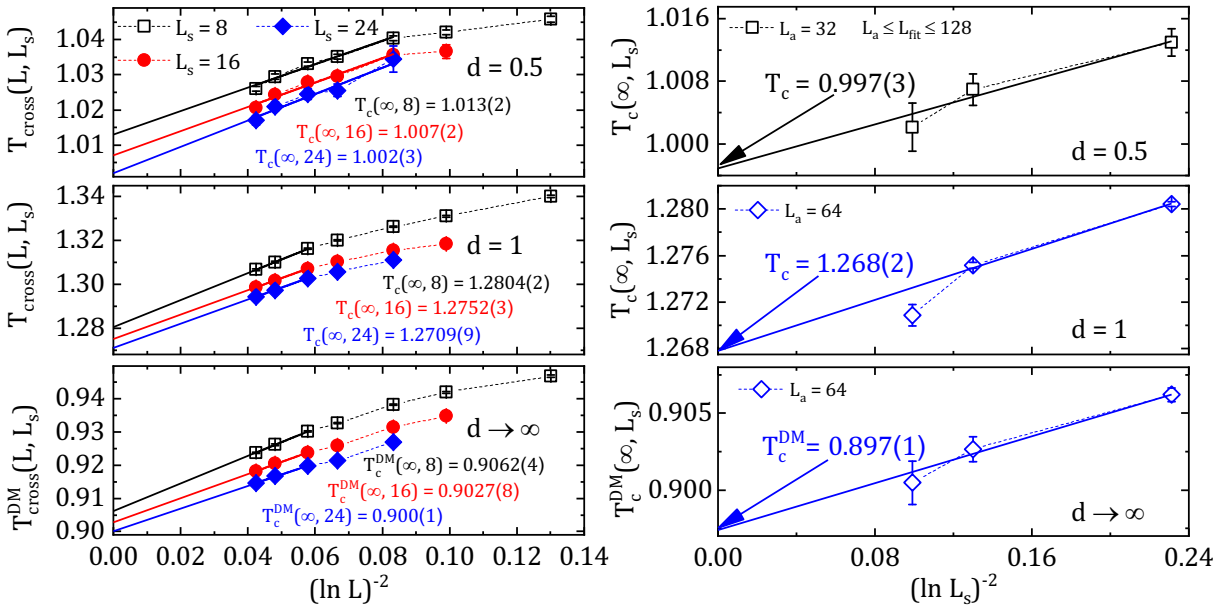

Figure 9 – The same as Figures 7 and 8, here for $d = 0.5$ using FBC (upper panels), $d = 1$ using PBC (middle panels), and the $d \to \infty$ limit using PBC, which is defined an effective temperature T^{DM}_{cross} in this case. The extrapolated transition temperatures $T_c(\infty, L_s)$ are also indicated in the graphs on the left side for the three reference lattice sizes. Then, $T_c(\infty, L_s)$ (T^{DM}_c for $d \to \infty$) is plotted as function of L_s, as shown by the graphs on the right side. L_a is the smallest lattice size considered in the fit interval $L_a \le L \le 128$ defined in the graphs on the left. The extrapolated transition temperatures in the $L_s \to \infty$ limit are also indicated, which are the corresponding final estimates.

$d \to \infty$, using PBC. The latter case means that the DM interaction tends to be dominant in the model, and an effective transition temperature, T^{DM}_c, is defined as

$$T^{DM}_c = \lim_{d\to\infty} \frac{T_c(d)}{\sqrt{1+d^2}}. \tag{2.21}$$

Since for $d = 1$ the pitch angle is $\phi = \pi/4$, according to Equation (2.4) for the modulation length $\ell(d)$, the finite lattices must be multiples of $\ell(1) = 8$ in order to keep the commensurability with the spin configurations, hence allowing the use of PBC. Likewise, the case $d \to \infty$ implies $\phi \to \pi/2$, with the modulation length corresponding to $\ell(d \to \infty) \to 4$, requiring the lattices to be integer multiples of 4 to keep the commensurability. As for the case of the pure planar rotator model, $d = 0$, one can see that the scaling regime in these three examples has been only reached for the largest lattices. In fact, this is a general trend for all values $d > 0$. $T_c(\infty, L_s)$ from the graphs on the left side are shown as a function of $(\ln L_s)^{-2}$ in the graphs on the right side. The additional extrapolation can still improve the estimate of the BKT temperature T_c slightly.

Table 2 gives the BKT transition temperature $T_c(d)$ so obtained for some additional values of the DM interaction d together with some available values previously obtained from the literature [34, 42, 55, 56]. The transition temperatures for $d = 0.5$ and $d = 1$ are

Table 2 – BKT transition temperature $T_c(d)$ and the ratio $T_c(d)/\sqrt{1+d^2}$ for some values of the DM interaction d, besides the boundary condition and the largest lattice used in the MC simulations. For a comparison, in the three last columns there are some results from the literature. The last line gives the average of $\overline{T_c(d)/\sqrt{1+d^2}} \equiv \overline{T}(0)$ for all values of d (including $d \to \infty$).

	In this work				**In other works**		
d	$T_c(d)$	$T_c(d)/\sqrt{1+d^2}$	Boundary condition	L_{max}	$T_c(d)$	Boundary condition	L_{max}
0	0.894(1)	0.894(1)	PBC	128	0.8935(1) [55]	PBC	512
					0.8935(5) [56]	PBC	4096
0.05	0.9018(7)	0.901(1)	FBC	128	≈ 0.896 [34]	PBC	32
0.25	0.930(2)	0.902(2)	FBC	128	—	—	—
0.5	0.997(3)	0.892(3)	FBC	128	1.013(4) [42]	FBC	96
0.75	1.1204(6)	0.896(1)	FBC	128	—	—	—
1	1.268(2)	0.897(1)	PBC	128	1.292(6) [42]	PBC	96
1.25	1.4491(2)	0.9053(1)	FBC	128	—	—	—
1.5	1.6203(4)	0.8988(2)	FBC	128	—	—	—
∞	—	0.897(1)	FBC	128	—	—	—
	$\overline{T}(0)$	0.898(4)					

comparable to the previous estimates from reference [42]. However, the present ones are expected to be more accurate due to the greater statistics obtained from the simulations. One can also note that the BKT transition temperatures from reference [42] are higher than the present ones. This is a consequence of the results in [42] being obtained by using all lattice sizes in the fits, which leads in a smaller slope for the data extrapolation.

In Table 2 there is also the transition temperature for a smaller value of d, namely $d = 0.05$, in order to seek whether the transition temperature starts first decreasing as d increases from zero before having a positive slope for higher values of d, as reported in References [34, 38] for the square and triangular lattices, respectively. For a comparison, a rough estimation of T_c for $d = 0.05$ from Reference [34] is also presented, which shows to be smaller than the correspondent T_c estimated in the present work. In fact, the present result for $d = 0.05$ indeed increases and $T_c(d)$ has a monotonic behavior for larger values of the DM interaction. The decreased value of T_c for small d obtained in References [34, 38] could be related to the use of PBC instead of FBC, the latter adopted in part of the MC simulations of this work. The expected behavior of the transition temperature as d increases will be better elucidated in the following subsection.

2.3.2 Critical temperature dependence on DM interaction

The corresponding phase diagram of the model in the DM interaction d versus the BKT transition temperature $T_c(d)$ plane, using the values from Table 2, is shown in the upper inset of Figure 10. It should be noted that as $d \to \infty$ the pitch angle goes to $\phi \to \pi/2$ and the transition frontier becomes a straight line. Thus, taking Equation (2.3) and considering $\phi = \pi/2$, an extra simulation can be performed to obtain an effective transition temperature $T_c^{DM} = T_c(d)/d$. This result gives, in fact, the asymptotic slope of

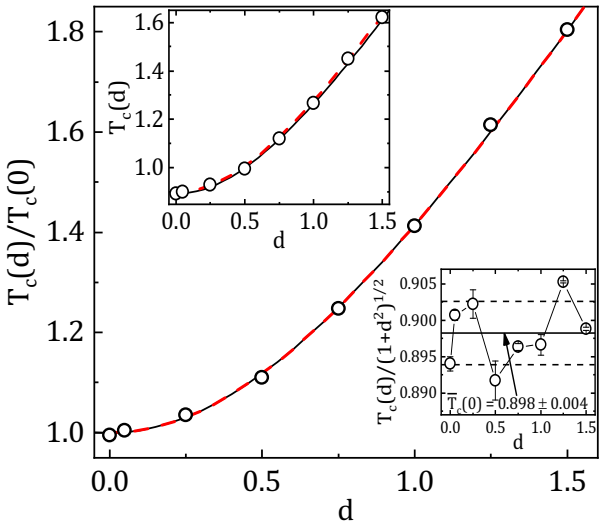

Figure 10 – The main graph is the phase diagram in the DM interaction d versus the reduced transition temperature $T_c(d)/T_c(0)$ plane. The circles are the results from Table 2 with $T_c(0) = 0.898(4)$. The solid line is the function $\sqrt{1+d^2}$ and the dashed line a fit with $\sqrt{r+d^2}$ with r given in the text (both lines are almost coincident to each other in the scale of the figure). The top inset shows $T_c(d)$ versus d where the solid line comes from Equation (2.24) with $T_c(0) = 0.894(1)$ and the dashed line is the hyperbola using Equation (2.25) with the parameters in the text. The bottom inset shows values of $T_c(d)/\sqrt{1+d^2}$ from the third column in Table 2 as a function of d. In this case, the solid line locates the mean value and the dashed lines the error bars.

the transition line as $d \to \infty$. Strikingly, the result is, within the error bars, the same as the transition temperature of the pure planar rotator model (as one can see in Table 2).

To better understand this behavior, and motivated by the definition of the order parameter in Equation (2.17), the following Hamiltonian can be considered, which reads

$$\tilde{\mathcal{H}}(d) = -\tilde{J}(d) \sum_{\langle i,j \rangle} \cos\left[\tilde{\varphi}_i(d) - \tilde{\varphi}_j(d)\right], \tag{2.22}$$

where

$$\tilde{\varphi}_i(d) = \varphi_i - (x_i + y_i)\phi(d), \tag{2.23a}$$

$$\tilde{\varphi}_j(d) = \varphi_j - (x_j + y_j)\phi(d). \tag{2.23b}$$

Since j is a nearest-neighbor of i, one has always $(x_i+y_i)-(x_j+y_j) = 1$, and $\tilde{\varphi}_i(d)-\tilde{\varphi}_j(d) = \varphi_i - \varphi_j - \phi(d)$. This means that Hamiltonian (2.22) above is equivalent to Hamiltonian (2.3). From (2.22) the transition temperature is thus given by

$$T_c(d) = T_c(0)\sqrt{1+d^2}. \tag{2.24}$$

The above equation gives the exact transition line of the planar rotator model with DM interaction. It is the equation of a hyperbola, which is symmetric regarding d, as should

be. This is the same result previously obtained for the one-dimensional version of the model [47].

Equation (2.24) also makes it clear that the ratio $T_c(d)/\sqrt{1+d^2}$ is a constant equivalent to the BKT transition of the pure planar rotator model. The third column in Table 2, and the corresponding data in the bottom inset in Figure 10, show this trend. The mean value $\overline{T}(0) = 0.898(4)$ is also quite comparable to the $T_c(0)$ obtained in the previous subsection and from values in the literature.

On the other hand, the ratio $T_c(d)/T_c(0) = \sqrt{1+d^2}$ is the equation of a rectangular hyperbola with equal semi-axis. Figure 10 also shows $T_c(d)/T_c(0)$, with $T_c(0) = \overline{T}(0) = 0.898(4)$, plotted together with the function $\sqrt{1+d^2}$ (solid line) and a fit with $\sqrt{r+d^2}$, where r is a fitting parameter (dashed line). In both cases one gets a quite nice agreement with the simulations and the value $r = 1.000(2)$ resulting from the fit, which is very close to the expected value $r = 1$.

The solid line in the upper inset of Figure 10 is obtained from Equation (2.24) with $T_c(0) = 0.894(1)$ and the dashed line is a fit of the simulation results with the hyperbole function

$$T_c(d) = T^*\sqrt{r+d^2}, \tag{2.25}$$

where T^* and r are the fitting parameters. Again, in both cases, a good agreement has been achieved with the simulation results, and the fitting parameters $T^* = 0.906(4)$ and $r = 0.99(1)$ are also comparable to the expected ones.

2.3.3 Critical exponent η

The BKT transition is expected to keep for any value of d and temperatures $T < T_c(d)$, since the transformed Hamiltonian (2.3) is, in essence, just another planar rotator model with renormalized exchange interaction. For the particular example of the pure model shown by the graph on the left side in Figure 6, one can see that the lattice sizes are still a little too small to fully reflect this behavior, because the cumulants are not all the same for temperatures lower than the crossing points, as clearer shown by the graph on the right in Figure 6. This same tendency is also seen for other values of the DM interaction. For this reason, in order to confirm the BKT transition at lower temperatures, the order parameter m, defined in Equation (2.17), was studied in conjunction with its scaling behavior (2.20).

As an example, Figure 11 shows a log-log plot of the order parameter m as a function of L for $d = 0.5$ with FBC and for temperature values ranging from $T = 0.87$, with constant increment $\Delta T = 0.01$, to $T = 1.04$. Most of the points (L, m) in the graph were obtained from extrapolations by using the histogram method (Appendix B). Whenever the power law given by Equation (2.20) is obeyed, the points will be aligned in a straight line. The solid lines in the graph are just a guide to the eyes and help observe the trend of

the data. The thicker dashed line is a reference curve and has a slope value equal to -0.125, which corresponds to Equation (2.20) having $\eta(T_c) = 1/4$. It is partly superimposed with the points of m for $T = 1.01$. Below this temperature value, all the data are along straight lines whose absolute values of the slopes decrease as T decreases. Conversely, the behavior of m starts to deviate from straight lines when $T \gtrapprox 1.01$, signifying that the scaling regime of Equation (2.20) is no longer valid and the system has been driven above the BKT transition.

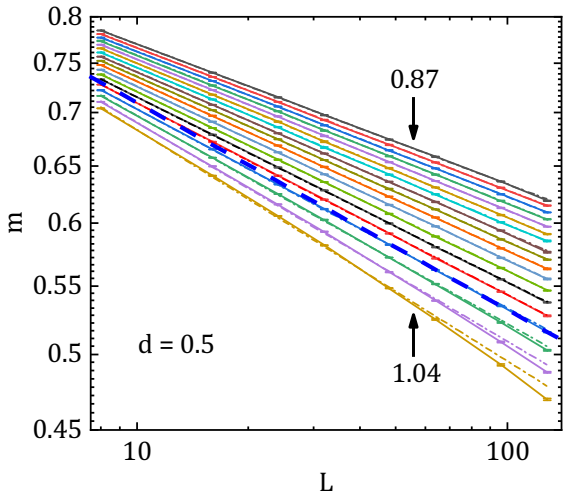

Figure 11 – Order parameter m as a function of the lattice size L for $d = 0.5$ at temperatures ranging from $T = 0.87$ to $T = 1.04$. Both axes are in logarithmic scale. The data are shown by the error bars of m. The solid lines are just a guide to the eyes. The dotted-dashed lines almost covered by the solid lines are straight lines fitted to the data. The thicker dashed line is a reference curve for the m dependence on L at $T = T_c$, representing the threshold of the transition exponent $\eta(T_c) = 1/4$.

The dotted-dashed lines in Figure 11, which some of them are almost coincident with the solid lines, are straight line fitted to the data corresponding to each temperature. As previously mentioned, from some value of T slightly above $T = 1.01$, m follows a power law on L as T decreases. In this case, the slopes obtained from the line fits are used to compute the spin-spin correlation critical exponent $\eta(T)$ for $T \leq T_c$. The results are shown in Figure 12 as a function of the temperature T. There are also some additional estimates of η not shown in Figure 11 for still lower temperatures, i.e. for $T < 0.87$. One can clearly see by Figures 11 and 12 that the transition is indeed of BKT type and the exponent $\eta \to 0$ as the temperature $T \to 0$, as expected.

Some selected values of the exponents of Figure 12 are displayed in Table 3. A rough estimate for the BKT transition temperature can be obtained from this table, resulting in $T_c = 1.011(1)$, quite consistent with the transition temperature $T_c = 0.997(3)$ given in Table 2. To verify the consistency of this method, the same analysis was applied to

$d = 0$ and provided $T_c = 0.9045(1)$, which is to be compared with the previous estimate $T_c = 0.894(1)$. In general, estimating T_c from the spin-spin correlation function critical exponent may demand even larger lattices so that the estimates become closer to those ones coming from the cumulant crossings analysis. These results are similar for other values of d.

Table 3 – Spin-spin correlation function critical exponent η for some values of temperature T for $d = 0.5$.

T	η	T	η
1.012	0.2516(9)	0.88	0.1724(2)
1.011	0.2502(9)	0.87	0.1692(2)
1.01	0.2486(9)	0.83	0.1570(2)
1.009	0.2498(9)	0.82	0.1542(2)
1	0.2318(4)	0.81	0.1514(2)
0.99	0.2238(4)	0.8	0.1488(2)
0.98	0.2168(4)	0.79	0.1460(2)
0.97	0.2102(2)	0.78	0.1434(2)
0.96	0.2046(2)	0.77	0.1408(2)
0.95	0.1996(2)	0.63	0.1068(2)
0.94	0.1952(4)	0.62	0.1058(2)
0.93	0.1902(2)	0.61	0.1038(2)
0.92	0.1866(2)	0.6	0.1016(2)
0.91	0.1828(2)	0.59	0.0996(2)
0.9	0.1792(2)	0.58	0.0976(2)
0.89	0.1756(4)	0.57	0.0956(2)

The data in Figure 12 can be further analyzed. The red solid line is a fit by using an approximate result for the temperature dependence of η, given by [57, 58]

$$\eta(T) \approx \frac{1}{4} - C\left(1 - \frac{T}{T_c}\right)^{1/2}, \tag{2.26}$$

which has been obtained theoretically for $T \leq T_c$, but with T close to T_c, being fixed as $T_c = 1.011$. C is a non-universal constant and is the only fitting parameter in this case. Since this equation is valid for T values slightly smaller than T_c, the fit was performed in the $0.97 \leq T \leq 1.01$ interval, as indicated by the red bar in Figure 12, providing $C = 0.189(3)$. Although a good agreement has been obtained close to T_c, the fitted curve is far from the simulation results in an extended region of lower temperatures. By supposing that may there be higher order contributions in Equation (2.26), another function $\tilde{\eta}(T)$ is defined as follows,

$$\tilde{\eta}(T) = \frac{1}{4} - C_0\left(1 - \frac{T}{T_c}\right)^{1/2} + C_1\left(1 - \frac{T}{T_c}\right) + C_2\left(1 - \frac{T}{T_c}\right)^{3/2}, \tag{2.27}$$

where C_0, C_1 and C_2 are fitting parameters and keeping $T_c = 1.011$. One can see a quite good agreement, in the entire temperature range, with fit parameters $C_0 = 0.179(3)$,

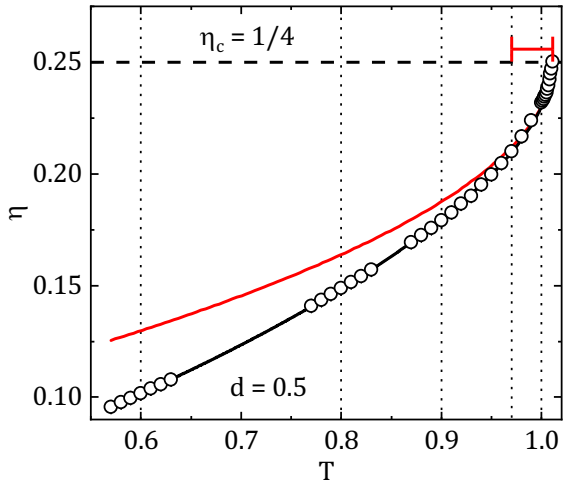

Figure 12 – Spin-spin correlation function critical exponent η as a function of the temperature T for $d = 0.5$. The vertical dotted lines locate the temperature at which the data were taken for constructing the histograms (Appendix B) and the horizontal dotted line is the threshold of the critical exponent $\eta_c = 1/4$. The full line passing through all the points is a fit according to Equation (2.27) with the parameters given in the text. The upper line (red color) is a fit with Equation (2.26) and considering only data for $T > 0.97$, which are delimited within the small bar on the upper right side of the graph.

$C_1 = -0.12(1)$ and $C_2 = 0.06(1)$, as shown by the black solid line in Figure 12. Moreover, at low temperature values, i.e. those ones close to zero, by considering a theoretical result from the spin-wave phase for the pure planar rotator model [57, 58] and rescaling the exchange term as $J \to J\sqrt{1+d^2}$, one obtains

$$\eta(T,d) \approx \frac{T}{2\pi\sqrt{1+d^2}}, \tag{2.28}$$

which results in $\eta(T, 0.5) \approx 0.14T$. For T much smaller than T_c in Equation (2.27), one has $\tilde{\eta}(T) \simeq 0.01(1) + 0.12(4)T$ for $d = 0.5$, having a good agreement with the theoretical prediction for low temperatures (2.28) for $d = 0.5$. These results show that Equation (2.27) may be adequate in representing the η dependence on T in the $0 \leq T \leq T_c(d)$ interval for some given d.

2.3.4 Effect of the DM interactions on the configurations

It is interesting to see the topology of the spin arrangements when the system passes by the present BKT transition. As discussed previously, at zero temperature the system orders with neighboring spins having angular differences equal to the pitch angle ϕ, which leads to a spiral ordering of the spins. However, as the temperature increases, there are fluctuations in these angular differences. Figure 13 depicts the corresponding spin configuration for $d = 0.5$ with FBC and lattice size $L = 48$ at three different values

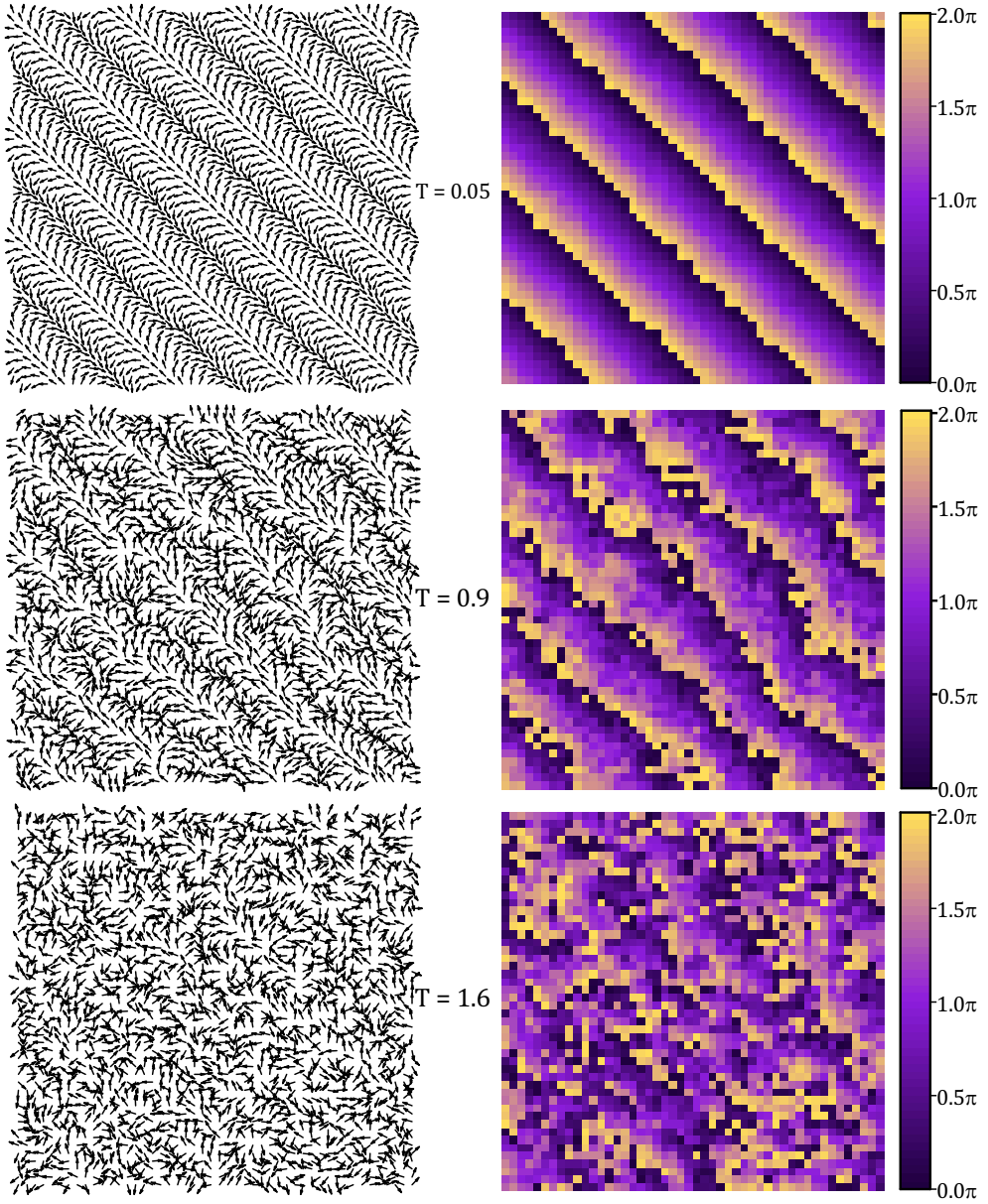

Figure 13 – Typical spin configurations given by the arrows (left panels) and color gradient of the spin orientation angle in radians (right panels) for $d = 0.5$ and lattice size $L = 48$ with FBC. Low temperature in the two upper panels; just below the BKT transition temperature in the two middle panels; and high temperature in the two bottom panels. The BKT transition temperature is estimated as $T_c = 0.997(3)$.

of temperature, as indicated between the graphs. All the panels on the left side of the figure show the spin configurations as vectors whereas the panels on the right side show them in an angular representation as color gradients for the spin angle in radians. The striped ordering of the spins may be better seen in the color gradient structure of the right panels: At low temperatures, such as $T = 0.05$, the order is well defined; Just below the BKT transition temperature, e.g. $T = 0.9$, the order still persists with larger fluctuations;

And, eventually, the disordered state is achieved for higher temperatures, as shown in the configuration at $T = 1.6$.

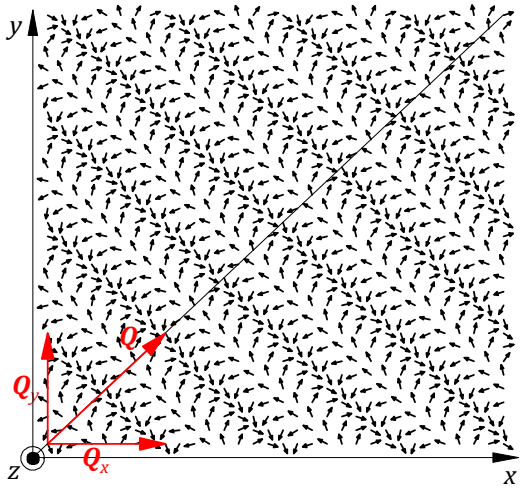

Figure 14 – Spin configuration for $d = 1$ at low temperature. $\boldsymbol{Q}_x$ and $\boldsymbol{Q}_y$ are spiral vectors that indicate how much the angle of a spin vector must rotate relative to the spin vector at the site which one moved in x- or y-direction, respectively. The sum of both vectors results in a vector $\boldsymbol{Q}$, giving rise to a spiral pattern along the diagonal directions parallel to the $\boldsymbol{Q}$ direction.

In section 2.1, the DM vector was defined to be perpendicular to lattice plane, i.e. $\boldsymbol{D} = D\boldsymbol{e}_z$, with $\boldsymbol{e}_z$ being a unit vector pointing in the positive z-direction of a rectangular coordinate system. Figure 14 shows a configuration at low temperature and the coordinate system for $d = 1$. In the ground state, after a displacement $\ell(d) = 2\pi a/\phi(d)$ along x- or y-directions of the lattice, the spin vectors are arranged as a flattened spiral in the plane, where every lattice spacing a the spin vector rotates clockwise (for $D > 0$) according to the pitch angle $\phi(d)$ when one moves in the positive x- or y-directions. As one can see in Figure 14, this pattern may be described by adopting an analogous definition of wave vector, with a wave vector in the x-direction and another in the y-direction, defined as

$$\boldsymbol{Q}_i(d) = \frac{2\pi}{\ell(d)}\boldsymbol{e}_i = \frac{\phi(d)}{a}\boldsymbol{e}_i, \tag{2.29}$$

with $i = x, y$, and $\boldsymbol{e}_i$ is a unit vector pointing in the positive i-direction. By definition, $Q_x(d) = Q_y(d)$. For convenience, $\boldsymbol{Q}_i(d)$ will be called *spiral vector*. Thus, these vectors give the angular shifting in the spirals along the x- and y-lattice directions. The sum of $\boldsymbol{Q}_x(d)$ with $\boldsymbol{Q}_y(d)$ yields a resulting spiral vector $\boldsymbol{Q}(d)$ parallel to the diagonal line shown in Figure 14, which has an angular slope equal to 45° relative to the x axis. $\boldsymbol{Q}(d)$ gives rise to spin spirals along directions parallel to this diagonal direction, while along the diagonal directions perpendicular to this one (or those diagonals having angular slope equal to 135° relative to the x axis) the spin vectors stay parallel to each other. In this case, all the spin vectors along a perpendicular direction to the $\boldsymbol{Q}$ direction rotate equally. The modulus

of $\boldsymbol{Q}$ is $Q = \sqrt{2}\phi/a = \phi/(a/\sqrt{2})$, where the factor $a/\sqrt{2}$ is one half the diagonal length of an $a \times a$ square plate in the lattice. In this way, when only the diagonal directions perpendicular to the $\boldsymbol{Q}$ direction are looked at, the effect of moving in the $\boldsymbol{Q}$ direction from a diagonal line to the next one introduces an angular difference of ϕ between the spin vectors in the previous diagonal line and the spin vectors in the next diagonal line.

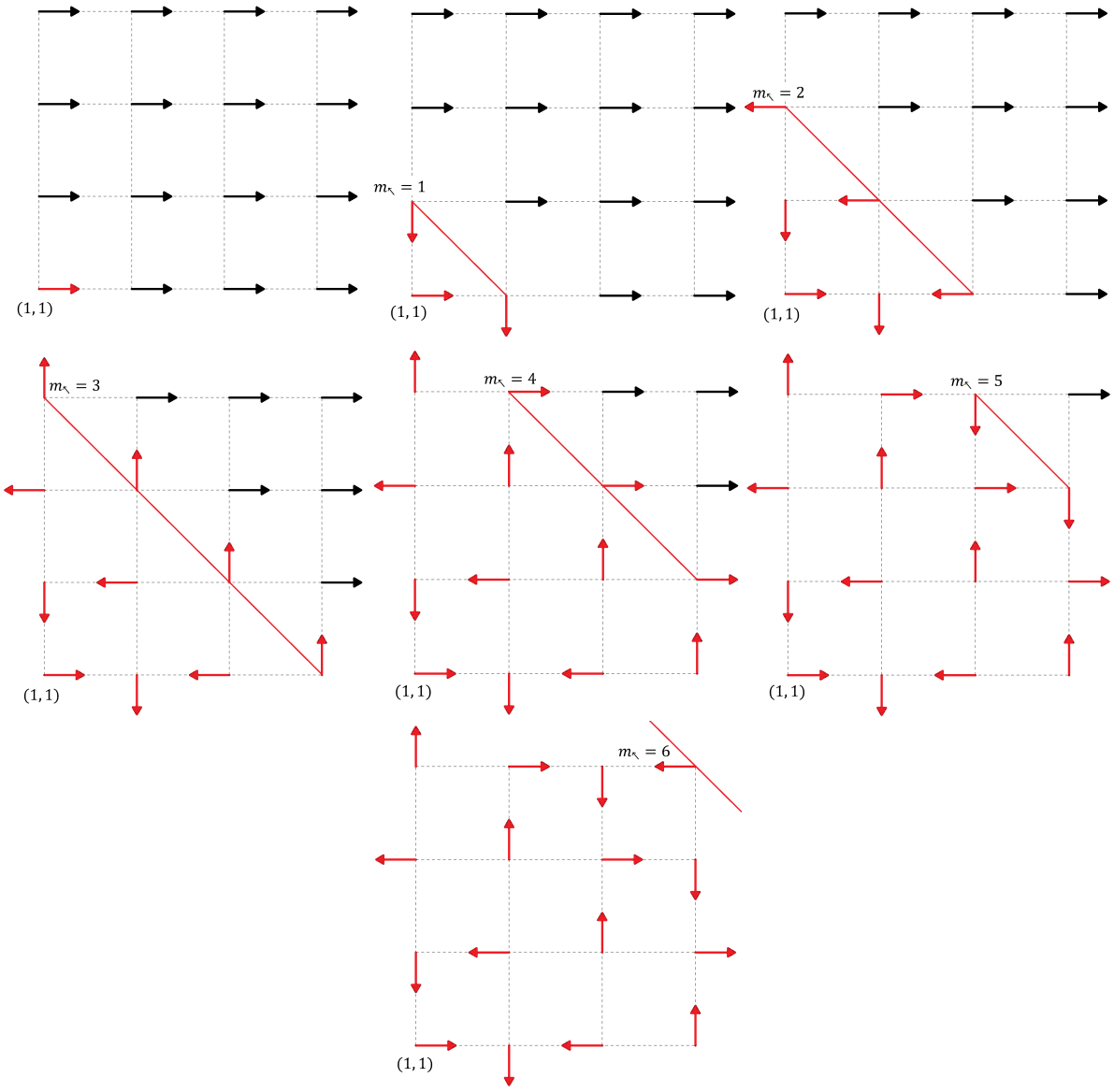

Figure 15 – Effect of the DM interaction upon the spin vectors. This is a limiting case where $d \to \infty$, which implies $\phi = \pi/2$, with $T = 0$. As the figure is read from the upper left panel in the sequence that $m_{\nwarrow}$ increases in each panel, the spin vectors along the indicated diagonal line rotates relative to the one at the position $(1, 1)$. The angular change is given by Equation (2.35).

As an instructive example about the action of the spiral vector $\boldsymbol{Q}$ on the spin configurations, Figure 15 shows a sequence of panels describing the spin angular shifting

throughout a lattice 4×4, for $d \to \infty$ limit, implying $\phi = \pi/2$. $T = 0$ is assumed and, initially, all the spin vectors are aligned and pointing in the same direction, due only to the FM interaction present in the model, while there is no DM interaction yet, as can be seen in the first panel (on the upper left corner of the figure). Once the DM interaction is "turned on" in the model, the two spin vectors linked by the diagonal line shown in the second panel (just on the right of the first panel) rotates $\pi/2$ relative to the spin at the site $(1,1)$, taken to be fixed and to be the reference spin vector where all the remaining ones rotate relative to. From the second panel on, as the diagonal line linking the spin vectors advances through the lattice, the spin vectors rotate as integer multiples of $\pi/2$ relative to the spin at the site $(1,1)$. The referred diagonal line with the spins will be symbolically represented as "diagonal $\nwarrow$" and the position of the sites along it is given by

$$\begin{aligned}\boldsymbol{r}\left(m_{\nwarrow}, n_{\nwarrow}\right) = &\left[\left(m_{\nwarrow} - n_{\nwarrow} + 1\right) H\left(L - m_{\nwarrow} - 1\right) + \left(L - n_{\nwarrow}\right) H\left(m_{\nwarrow} - L\right)\right] a\boldsymbol{e}_x \\ &+ \left[\left(n_{\nwarrow} + 1\right) H\left(L - m_{\nwarrow} - 1\right) + \left(m_{\nwarrow} + n_{\nwarrow} - L + 2\right) H\left(m_{\nwarrow} - L\right)\right] a\boldsymbol{e}_y,\end{aligned} \tag{2.30}$$

where $m_{\nwarrow}$ labels each diagonal $\nwarrow$, as shown in Figure 15, and $n_{\nwarrow}$ labels the sites of the $m_{\nwarrow}$th diagonal $\nwarrow$. Explicitly, $m_{\nwarrow}$ and $n_{\nwarrow}$ are written as

$$\begin{aligned} m_{\nwarrow} &= 1, 2, ..., 2(L-1), \\ n_{\nwarrow} &= \begin{cases} 0, 1, ..., m_{\nwarrow}, & \text{if} \quad m_{\nwarrow} \leq L - 1. \\ 0, 1, ..., 2(L-1) - m_{\nwarrow}, & \text{if} \quad m_{\nwarrow} > L - 1. \end{cases} \end{aligned} \tag{2.31}$$

Still in Equation 2.30, $H(x)$ is the Heaviside function, defined as

$$H(x) = \begin{cases} 0, & \text{if} \quad x < 0. \\ 1, & \text{if} \quad x \leq 0. \end{cases} \tag{2.32}$$

The angle $\varphi(\boldsymbol{r})$ of the spin vector at a site indicated by the position vector $\boldsymbol{r} = \boldsymbol{r}\left(m_{\nwarrow}, n_{\nwarrow}\right)$ will be referred to as $\varphi\left(m_{\nwarrow}, n_{\nwarrow}\right)$. Furthermore, a vector $\boldsymbol{R}$ parallel to the spiral vector $\boldsymbol{Q}$ is defined and gives the position of each diagonal $\nwarrow$ by the point at the middle in it. Thus, one has

$$\boldsymbol{R}\left(m_{\nwarrow}\right) = m_{\nwarrow} \frac{a}{2} \left(\boldsymbol{e}_x + \boldsymbol{e}_y\right), \tag{2.33}$$

which every displacement $m_{\nwarrow} a/2$ along x- or y-direction, starting from the site $(1,1)$, indicates the $m_{\nwarrow}$th diagonal $\nwarrow$. By $\varphi\left(m_{\nwarrow}, n_{\nwarrow}\right)$ into $\varphi_{\boldsymbol{Q}}\left(m_{\nwarrow}, n_{\nwarrow}\right)$ changing, one can show how much each spin vector must rotate relative to the reference spin vector at the site $(1,1)$, where

$$\varphi_{\boldsymbol{Q}}\left(m_{\nwarrow}, n_{\nwarrow}\right) = \varphi\left(m_{\nwarrow}, n_{\nwarrow}\right) - \boldsymbol{Q} \cdot \boldsymbol{R}\left(m_{\nwarrow}\right). \tag{2.34}$$

Since $\boldsymbol{Q} = (\phi/a)\left(\boldsymbol{e}_x + \boldsymbol{e}_y\right)$ and $\boldsymbol{R}\left(m_{\nwarrow}\right)$ is specified in Equation (2.33), the obtained result is

$$\varphi_{\boldsymbol{Q}}\left(m_{\nwarrow}, n_{\nwarrow}\right) = \varphi\left(m_{\nwarrow}, n_{\nwarrow}\right) - m_{\nwarrow}\phi. \tag{2.35}$$

This equation shows more clearly how the spin angular shifting throughout the lattice may be watched, as in Figure 15, where after rotating $m_{\nwarrow}\phi$ clockwise all the spins vectors in each diagonal labeled by $m_{\nwarrow}$, the configuration shown in the last panel (i.e. the one for the model with FM and DM interactions according to the d value) will be obtained. To recover the configuration of the model with only FM interaction, as shown in the first panel of Figure 15, the angle of each spin vector must be changed from $\varphi_{\boldsymbol{Q}}(m_{\nwarrow}, n_{\nwarrow})$ into $\varphi_{-\mathbf{Q}}(m_{\nwarrow}, n_{\nwarrow})$ as follows,

$$\varphi_{-\boldsymbol{Q}}(m_{\nwarrow}, n_{\nwarrow}) = \varphi_{\boldsymbol{Q}}(m_{\nwarrow}, n_{\nwarrow}) + \boldsymbol{Q} \cdot \boldsymbol{R}(m_{\nwarrow}) = \varphi(m_{\nwarrow}, n_{\nwarrow}), \tag{2.36}$$

where this inverse transformation is done by obtaining a new equation from (2.34) after changing $\varphi(m_{\nwarrow}, n_{\nwarrow}) \to \varphi_{\boldsymbol{Q}}(m_{\nwarrow}, n_{\nwarrow})$ and $\boldsymbol{Q} \to -\boldsymbol{Q}$, then replacing $\varphi_{\boldsymbol{Q}}(m_{\nwarrow}, n_{\nwarrow})$ by the right hand side of Equation (2.34). The inverse transformation is also performed relative to the spin at site $(1, 1)$.

The strip arrangement due to the DM interaction in some sense seems to cover up the topological structure of vortices in these systems. However, this is not indeed the case. As discussed previously, the spins can be changed according to the inverse transformation (2.36) to obtain similar configurations of the pure planar rotator model. In this model, a vortex and an antivortex are defined according to the vorticity, q, calculated from the following equation [9],

$$\sum \Delta\varphi(\boldsymbol{r}) = 2\pi q, \quad q = 0, \pm 1, \pm 2, ..., \tag{2.37}$$

where the sum is performed on the angular differences $\varphi(\boldsymbol{r} + \boldsymbol{a}) - \varphi(\boldsymbol{r})$ between two consecutive spin vectors separated by a lattice spacing a, taken along a closed path on the lattice [5]. Particularly, in the case of a finite and square lattice, the path may be set as the edges of an $a \times a$ square plate, passing through four sites at the corners. Then, by using Equation (2.37) and taking the path in a counter-clockwise direction, the vorticity may result in: $q = 2\pi$, to be defined as a vortex; $q = -2\pi$, which defines an antivortex; or $q = 0$, meaning that there is neither a vortex nor an antivortex at the considered plate in the lattice.

As an example, Figure 16 shows the spin configurations, together with the location of the vortex-antivortex pairs, for $d = 0.5$. The top panels correspond to a temperature just below the transition temperature, and the bottom panels to a temperature above the transition. The left panels show the actual configurations and the right panels show the configurations after the effect of the DM interaction on the spin vectors has been undone. The dots and stars locate the vortex and antivortex cores, which are centered with the middle point of the correspondent plates that they appear. One can see that the vortex-antivortex pairs are still present even in the actual configuration of the spins due to the DM interaction.

[5] In the continuous limit, the vorticity is defined as $\oint \nabla\varphi(\boldsymbol{r}) \cdot d\mathbf{l} = 2\pi q$, $q = 0, \pm 1, \pm 2, ...$, with the integral being performed along a closed path on the lattice.

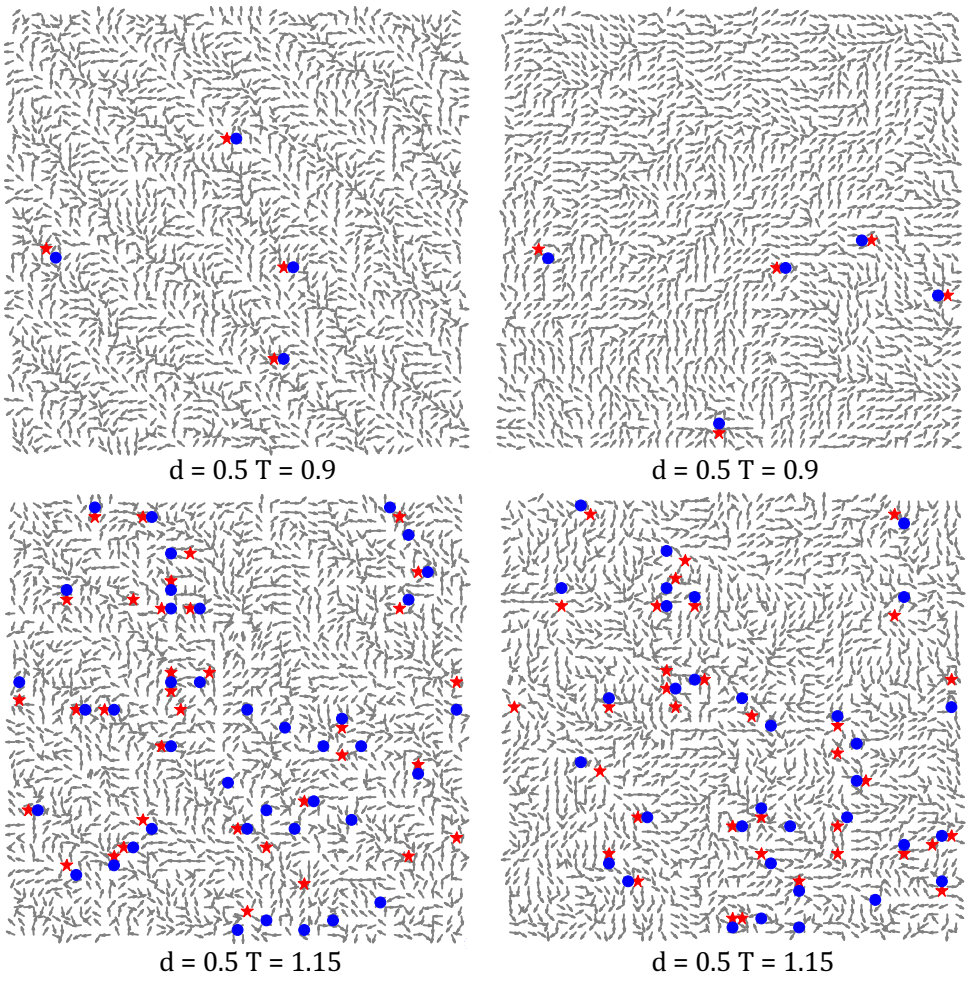

Figure 16 – Spin configurations for $d = 0.5$ just below the transition temperature in the top panels and just above the transition temperature in the bottom panels. The left panels show the actual configurations and the right panels the configurations without the effect of the DM interaction on the spins. The dots and stars locate the vortex-antivortex pairs. As the temperature increases towards the BKT transition temperature ($T_c \sim 1.0$ for $d = 0.5$), the number of bonded vortex-antivortex pairs increases. Above T_c, the vortices and antivortices unbind from each other.

In the pure planar rotator model, the vortex-antivortex pairs density (the total number of them divided by the total number of spins in the lattice) depends on the temperature, and it is given by [58]

$$\rho(T) \sim e^{-2\mu/T}, \tag{2.38}$$

where μ is the chemical potential and 2μ is the energy of a vortex-antivortex pair for $|q| = 1$, with their cores separated by a lattice spacing a. This equation is approximately valid in $0 < T \lesssim T_c$, in which the vortex-antivortex pairs are diluted throughout the lattice with each vortex tightly bonded to an antivortex. The energy of the bonded pair depends on the exchange term as $2\mu = 2\pi^2 J$ [9, 10]. As previously observed, the presence of the

DM interaction rescales the exchange term J as $J\sqrt{1+d^2}$ in the planar rotator model. Thus, the chemical potential changes into

$$\mu(d) = \mu(0)\sqrt{1+d^2}, \tag{2.39}$$

with $\mu(0) = \pi^2 J$ being the chemical potential of the pure planar rotator model. On this hand, the density of vortex-antivortex pair depends on the temperature and also the intensity of the DM interaction as follows,

$$\rho(T,d) \sim e^{-2\mu(d)/T}, \tag{2.40}$$

in the interval of $0 < T \lesssim T_c(d)$. The temperature range where the vortex-antivortex pairs remain tightly bonded to each other is extended from $T_c(0)$ to $T_c(d)$, and the DM interaction increases the energy of the bonded pairs.

As shown in Figure 16 at temperatures below T_c, the number of vortex-antivortex pairs is lower. When the temperature decreases towards zero, this number tends to be even lower, and spin waves are dominant in this case [28]. As the temperature increases towards T_c, the number of vortex-antivortex pairs increases and, eventually above T_c, the vortices and antivortices will be unbonded. This unbinding between vortices and antivortices that marks the BKT phase transition.

As an optional and extra way to illustrate the effect of DM interaction on the spins, Figure 17 shows a video[6] of the actual spin configuration (on left side) and the configuration after removing the spiral pattern of the spin vectors due to DM interaction, with the angle transformations being done with the simulation running.

2.3.5 Boundary condition analysis

For DM interactions where the lattice sizes become incommensurate with the spin orientations, the FBC have provided more reliable results than the usual PBC. Although in the previous results for $d = 0.5$ the FBC have been implemented in the same finite lattices used with PBC for commensurate values of d, one can as well investigate the behavior for *quasi-commensurate* sizes using integer multiples of the modulation length $\ell(d)$, given by Equation (2.4). For instance, for $d = 0.5$ the pitch angle is $\phi = 0.4636...$ rad and $\ell = 13.5516...$, meaning that one can choose $L = 14, 28, 42, ...$ instead of multiples of $\ell = 8$ for $d = 1$ as before. Figure 18 depicts the log-log plot of the order parameter m as a function of lattice sizes L considering both choices: $L = 8, 16, 24, 32, 48, 64, 96$ and 128 for $L = 8 \times n$; $L = 14, 28, 42, 56, 70, 84, 98$ and 126 for $L = 14 \times n$. With the data obtained from the simulations with FBC, the critical exponent at $T = 0.9$ is given by $\eta = 0.08954(4)$ and is comparable to the value $\eta = 0.0896(1)$ obtained by using only lattice sizes that are multiples of $\ell = 8$. Then, as soon as one uses FBC, the sizes of lattices are clearly not so important for getting the transition properties of the model.

[6] Video content might not be allowed in PDF/A files. The reader can eventually request a PDF version of this document by emailing gas.physics@gmail.com in case the video is disabled.

Figure 17 – (*Video visualization on Adobe Reader*). Effect of the DM interaction upon the spin vectors. The two graphs on the left are the same configuration, but represented by arrows (top graph) and color gradient of the spin orientation angle in radians (bottom graph). The effect of the DM interaction is active on the spins in the lattice in this case. Similarly, the graphs on the right show the configurations on the left after the effect of the DM interaction on the spins has been undone. The change of the configurations seen in this video occur every 500 MCS during the simulation, using only Metropolis algorithm.

Figure 18 also shows the results for all considered lattice sizes[7], but this time for data from simulations using PBC. Clearly, most of the values fall off either far below or above the fit obtained by using FBC data. Even for the quasi-commensurate lattice sizes, with PBC, the results are still rather far from the fit obtained by using FBC. Some of the points exhibit a smaller discrepancy relative to those ones obtained with FBC. These points have L values that reduce the incommensurability level, as $L = 42$. Conversely,

[7] Except $L = 126$. The rounding error due to do 9×14 and not $9 \times \left(2\pi/\tan^{-1} 0.5\right) = 121.96... \approx 122$ became relevant. Thus, $L = 126$ and $L = 128$ similarly lead to incommensurability.

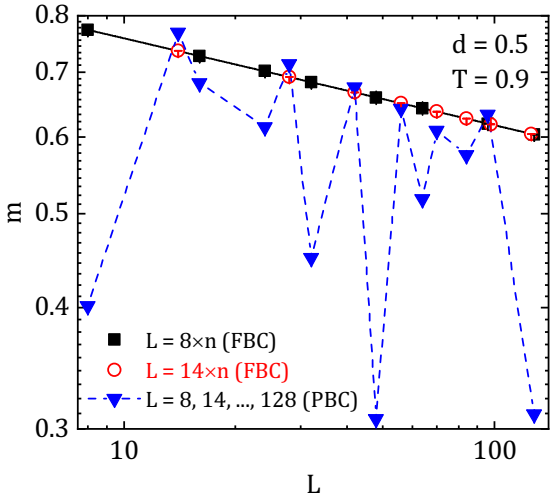

Figure 18 – Log-log plot of the order parameter m as a function of the lattice size L for $d = 0.5$ and $T = 0.9$. The squares correspond to lattice sizes that are multiples of 8 with $n \leq 16$ while the circles are optimal sizes which are multiples of 14 with $n \leq 9$. The triangles are data obtained by considering all lattices with PBC. The solid line is a fit to the scaling function given by Equation (2.20) using only the results obtained from FBC. The dashed line is just a guide to the eyes. Due to not all the n values have been used, the lattice size values are explicitly given in the text.

the points exhibiting large discrepancy are those ones with L values that yield a larger incommensurability level, as one can see for $L = 48$.

The use of quasi-commensurate lattice sizes with FBC in the incommensurate case has an important effect upon the probability distribution of the phase shift angle Δ introduced in the angular differences (2.13) and obtained from the simulations according to the prescription (2.14). Figure 19 shows the phase shift angle probability distribution $P^*(\Delta) = P(\Delta)/P(\langle\Delta\rangle)$ for several values of temperature T for $d = 0.5$, and two different lattice sizes, namely $L = 48$ and $L = 41$. To have a better visualization, in each case the actual probability $P(\Delta)$ has been divided by the computed probability $P(\langle\Delta\rangle)$ at the mean value $\langle\Delta\rangle$, so one always has $P^*(\langle\Delta\rangle) = 1$. The actual probability $P(\Delta)$ was obtained from the data generated by 10 MCSL at each temperature value. In general, almost all the $P^*(\Delta)$ distributions are Gaussian and have been fitted using

$$P^*(\Delta) = P_0 + A \exp\left[-\frac{(\Delta - \langle\Delta\rangle)^2}{2w^2}\right], \tag{2.41}$$

where P_0 and A are constants and w is the width of the distribution. Firstly, one can see that the width w decreases as T decreases. Secondly, as the temperature increases above the BKT temperature, namely $T_c = 0.997(3)$, the distribution flattens and reaches a constant value meaning that in this region the phase shift angle is not so important due to the strong thermal fluctuations. Lastly, the only difference between the quasi-commensurate size (here $L = 41$ by rounding of $3\ell = 40.65...$) and any other size will be just the mean

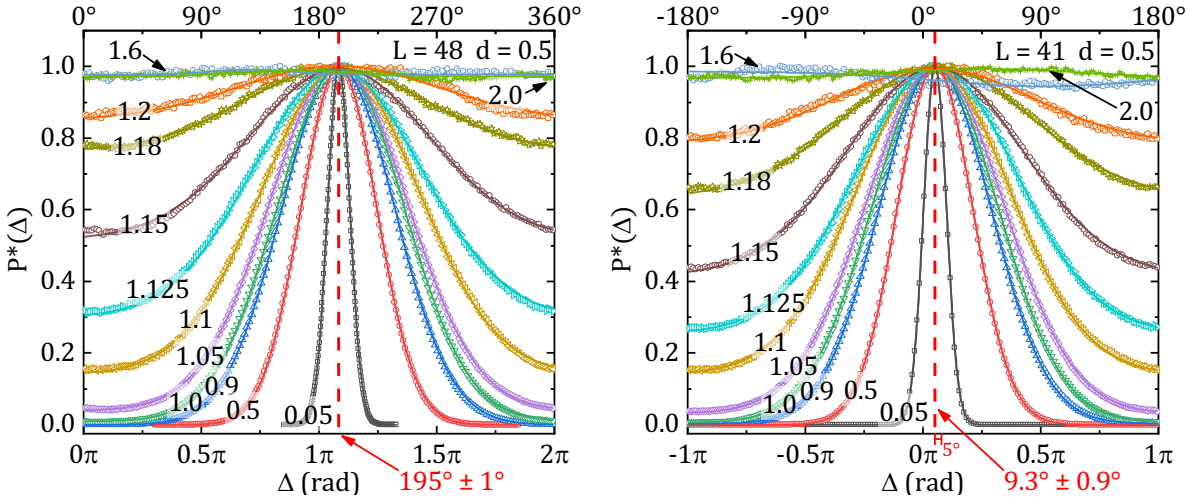

Figure 19 – Phase shift angle probability distribution $P^*(\Delta)$ for $d = 0.5$ and several values of temperature, indicated on each curve. The lattice size is $L = 48$ in the left panel and $L = 41$ in the right panel. The solid lines along the points are Gaussian fits according to Equation (2.41). In each graph, the vertical dashed line and the arrow indicate the average $\overline{\langle\Delta\rangle}$ of the mean values $\langle\Delta\rangle$ coming from the fits in the data from $T = 0.05$ up to $T = 1.2$.

value $\langle\Delta\rangle$ of the phase shift angle Δ, which for quasi-commensurate sizes will be closer to zero. If commensurate lattice sizes are used in the simulations with FBC for integer $\ell(d)$, the same qualitative behavior above described is obtained, with $\langle\Delta\rangle \cong 0$.

The vertical dashed lines in the graphs of Figure 19 indicate the average $\overline{\langle\Delta\rangle}$ of the mean values $\langle\Delta\rangle$ coming from the fits in the data from $T = 0.05$ up to $T = 1.2$ for each lattice size L. The results are $\overline{\langle\Delta\rangle} = (195\pm1)^\circ$ for $L = 48$ and $\overline{\langle\Delta\rangle} = (9.3\pm0.9)^\circ$ for $L = 41$. As discussed in section (2.13), at $T = 0$ the phase shift angle can be exactly calculated as $\Delta = \mathrm{mod}\,(L\phi, 2\pi)$, providing $\Delta = 195.12...^\circ$ and $\Delta = 9.16...^\circ$ for $L = 48$ and $L = 41$, respectively. These results show that the predicted incommensurability between the lattice and the ground state spin structure persists in the whole temperature range below T_c, even though Δ starts dispersing around $\langle\Delta\rangle$ as T increases. Furthermore, taking Δ at $T = 0$ as a measurement of the incommensurability level, even when a quasi-commensurate lattice size (as $L = 41$ for $d = 0.5$, an unavoidable incommensurability) is used, there will still be some residual incommensurability level. The maximum incommensurability level occurs when $\Delta = 180^\circ$ (as $L = 48$ does for $d = 0.5$, reflecting the large deviation of the order parameter seen in Figure 18 for the result with PBC).

The incommensurability level can be seen in Figure 20 for some d values used in this work and according to the lattice size L. The points come from the use of $\Delta = \mathrm{mod}\,(L\phi, 2\pi)$. The d value is shown between the brackets in front of Δ in the vertical axis and the L values are equally spaced by a unity step. The two horizontal dashed lines in each graph correspond to $\Delta = 0^\circ$ and $\Delta = 360^\circ$. Some lattice sizes multiple of eight are highlighted

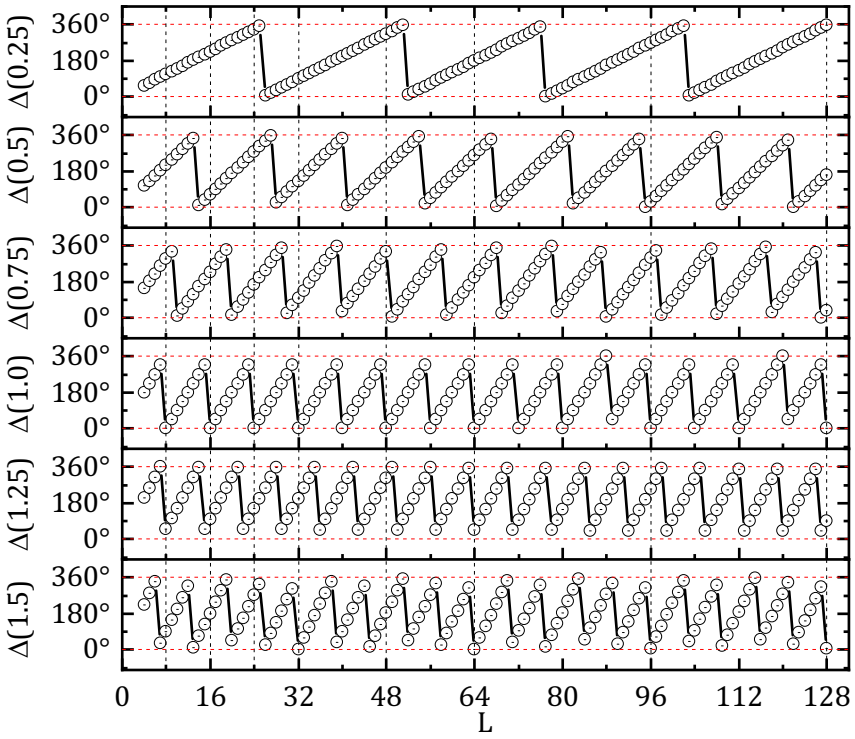

Figure 20 – Phase shift angle Δ as a function of the lattice size L for the ground state spin configuration, i.e. $T = 0$. Each graph corresponds to a different d value, shown between the brackets in the vertical labels. The horizontal dashed lines delimit the range of angles between 0° and 360° in the vertical axis of each graph. The vertical dashed lines just indicate some L values multiple of eight. If a point (L, Δ) for some value of d coincides exactly with the horizontal dashed lines, the lattice and spin structure are commensurate, otherwise, they are incommensurate.

by the vertical dashed lines. Although several points in the graphs seem to be coincident with the horizontal dashed lines, this is only true for $d = 1$, where the phase shift angle is exactly equal to 0° or 360° for the lattice sizes indicated by the vertical dashed lines. They are commensurate. The quasi-commensurate lattices are just the ones having $\Delta \approx 0°$ or $\Delta \approx 360°$, as pointed out before.

In closing, different types of boundary conditions influence the universal value of the fourth-order cumulant U_4^* in the thermodynamic limit (although the transition temperature is not affected by them), as happens in the Ising model [59]. A same feature has been observed in this work, where for $d = 0$ (the pure planar rotator model), the estimates $U_4^* = 0.6599(3)$ with PBC and $U_4^* = 0.6468(1)$ with FBC were obtained.

2.4 Conclusion

The planar rotator model with Dzyaloshinskii-Moriya (DM) interaction has been studied through extensive Monte Carlo simulations by employing a hybrid algorithm

consisting of single-spin Metropolis updates and Swendsen-Wang cluster-spin updates. Single histogram reweighting techniques have been introduced to obtain the thermodynamic variables close to the Berezinskii-Kosterlitz-Thouless (BKT) transition and finite-size scaling has been used to analyze the phase transition behavior in the thermodynamic limit. Fluctuating boundary condition (FBC) has been utilized in order to match the incommensurability between the spin structure and the finite lattice sizes due to the DM interaction. The effects of the FBC have been analyzed in detail and the BKT transition temperature, as well as the corresponding spin-spin correlation function critical exponent η, have been obtained as a function of the DM interaction and temperature.

The transition is indeed of BKT type for any value of the DM interaction, and the critical exponent η decreases from 1/4 towards zero as the temperature decreases. The spin ground-state has a spiral ordering, which may, alternatively, be seen as strips of aligned spins that lose their conformation as the temperature approaches the BKT transition temperature. A detailed exposition about the effect due to the DM interaction on the spins showed that the topological structure of vortices of the pure planar rotator model are present as in the configuration with the undone modulation of the spins as in the actual spiral configuration.

In cases of incommensurability, quasi-commensurate sizes for the finite lattices, or any other lattice sizes, furnish coherent results as soon as FBC are considered. The distribution of the phase shift angle, however, has mean values closer to zero for quasi-commensurate lattices and quite different values for other sizes. Even if a quasi-commensurate lattice is used with PBC when there is an unavoidable incommensurability in the model, some deviation can appear in the thermodynamic variables, leading to incorrect results. Although in the thermodynamic limit different types of boundary conditions should lead to same critical quantities, this has not been the case for the universal value of the order parameter fourth-order cumulant, which has shown to be dependent of the boundary condition in the planar rotator model.

Another important result in the present work is the exact analytic equation for the transition temperature of the model as a function of the DM interaction, which has been verified by simulation. Besides the fact that this relation could be used in the study of quantum versions of the planar rotator model with DM interaction, there are some important features of the present simulations that helped lead to a better understanding of the physical behavior of the model. In addition, some of these features should certainly be quite useful in studying models with other types of anisotropies, for instance, as follows:

(i) The importance of considering fluctuating boundary conditions, even to compute the exponent η, as depicted in Figure 18;

(ii) The scaling behavior of the exponent η as a function of temperature, given by Equation (2.27), which extends to the entire temperature range;

(iii) Looking at the spin configurations of Figure 13, it is not at all obvious that the model still exhibits vortex and antivortex pairs and a BKT transition. It looks, indeed, at first sight like a conventional transition. However, in Figure 16 was shown that the vortices and antivortices have been still present, which means that the transition is really of BKT type;

(iv) The Gaussian distribution of the phase shift angle in Figure 19 is expected to be the same for other models.

As a general result, the study of the planar rotator model with DM interaction could be seen as being equivalent to study the pure planar rotator model with a rescaled exchange term, dependent of the DM interaction intensity. The modulation of the spin orientations caused by the DM interaction can accordingly be undone to recover the typical spin arrangement of the pure planar rotator model.

3 Three-dimensional Heisenberg model with DM interaction

3.1 Hamiltonian model

In Chapter 1 the Heisenberg Hamiltonian $\mathcal{H}_H$ was initially presented in its quantum form by Equation (1.1). As long as the temperature is not quite low, where quantum effects start to dictate the model, the quantum Hamiltonian can be written as a classical Hamiltonian by assuming classical spin vectors. The classical model will be considered in this study, with spin vectors defined in spherical coordinates as $\boldsymbol{S}_i = S(\cos\varphi_i \sin\theta_i, \sin\varphi_i \sin\theta_i, \cos\theta_i)$ at a site i in a simple cubic lattice, with S being the spin magnitude, φ_i the azimuthal angle and θ_i the polar angle. The exchange interactions will be isotropic and the exchange terms in Equation (1.2) are set as $J^x = J^y = J^z = J \neq 0$. Thus, the Hamiltonian for the model is given by

$$\mathcal{H}_H = -JS^2 \sum_{\langle i,j \rangle} \left[\cos\left(\varphi_i - \varphi_j\right) \sin\theta_i \sin\theta_j + \cos\theta_i \cos\theta_j\right]. \tag{3.1}$$

As done in Section 2.1, J is placed outside of the sum, $J > 0$ to have FM interactions in the model, and $\langle i, j \rangle$ truncates the sums so that only interactions of nearest-neighbor sites are allowed.

Differently from the planar rotator model presented in Chapter 2, which does not have long-range ordering at any temperature (only at $T = 0$), the above model presents long-range ordering at a finite critical temperature. In this case, when the system passes by the critical temperature, it undergoes a *second-order* phase transition, in which the thermodynamic quantities of a finite-size system follow a power-law behavior that scales with its size according to a set of critical exponents. This set of critical exponents are known to be the same for models sharing the same lattice dimensionality, the same spin dimensionality, and range of interactions, defining what is called a universality class [6, 60]. Some examples of magnetic materials that have been experimentally verified to belong the Heisenberg universality class are ferromagnets such as Fe, Ni, EuO, antiferromagnets such as $FbMnFe_3$, as can be checked in Reference [61], and transition metal oxides such as $La_{0.73}Ba_{0.27}MnO_3$ [62].

The DM interactions are introduced in the above Heisenberg model by using the Hamiltonian $\mathcal{H}_{DM}$ in Equation (1.3), setting the DM vector $\boldsymbol{D}$ with just one component different from zero along positive z-direction in the coordinate system of the lattice. Homogenous DM interaction is also assumed in the model, with its intensity remaining

unchangeable as one goes through all sites of the lattice. Thus, $\mathcal{H}_{DM}$ is written as

$$\mathcal{H}_{DM} = DS^2 \sum_{\langle i,j \rangle} \sin\left(\varphi_i - \varphi_j\right) \sin\theta_i \sin\theta_j, \tag{3.2}$$

where the same conventions in Equation (3.1) have been adopted: D is placed outside of the sum and the interactions are taken only for nearest-neighbors sites.

Once the Heisenberg Hamiltonian $\mathcal{H}_H$ and the DM Hamiltonian $\mathcal{H}_{DM}$ have been specified, they are added together, as shown in Equation (1.4), to yield the combined Hamiltonian,

$$\mathcal{H}(d) = -JS^2 \sum_{\langle i,j \rangle} \left\{ \sqrt{1+d^2} \cos\left[\varphi_i - \varphi_j - \phi(d)\right] \sin\theta_i \sin\theta_j + \cos\theta_i \cos\theta_j \right\}, \tag{3.3}$$

where $d = D/J$ and $\phi(d) = \tan^{-1} d$. The two terms that depend on the azimuthal angles have been simplified into one term as a result of the linear combination of cosine and sine functions with both having the same argument. This result can also be achieved by using the transformation proposed in reference [47].

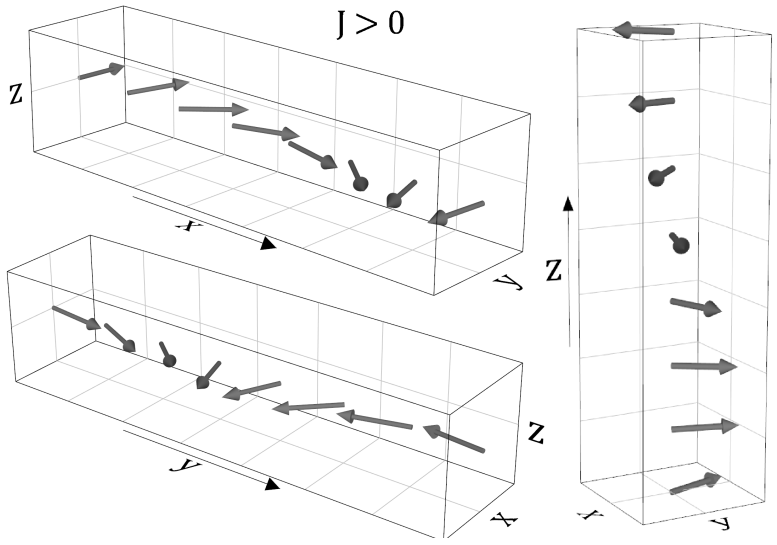

Figure 21 – Spin arrangements along x-, y- and z-directions of a typical ground state configuration of the three-dimensional Heisenberg model with DM interaction. The spin vectors are modulated according to a pitch angle $\phi(d)$, where d is the ratio of the DM to the FM interaction intensities. The modulation has a length $\ell(d)$. This is an example with $d = 0.5$, which results in $\ell(0.5) = 13.55....$

Similarly to the model studied in Chapter 2, the ground-state spin configurations associated to the Hamiltonian (3.3) have spiral ordering, as one can see in Figure 21. The spin vectors are also restricted to lie in planes perpendicular to the DM vector, with a modulation of the x- and y-spin components, which in turn extends along the x-, y- and z-directions of the lattice. In this case, the z-components of the spin vectors are quenched in the absence of thermal fluctuations. The modulation length as a function of d

previously defined by Equation (2.4), namely $\ell(d) = 2\pi a/\phi(d)$, also holds in the present model, where a is the lattice spacing and $\phi(d)$ is the pitch angle. The definitions about commensurability and incommensurability between spin structure and finite lattices are still the previous same ones: if $La/\ell(d)$, where La is a longitudinal dimension of the lattice, results in an integer number, the modulation length is commensurate with this lattice length, and incommensurate otherwise. The boundary condition choice becomes important in incommensurability cases, since an unappropriated choice may prevent finite-size scaling (FSS) from extracting any meaningful results, as addressed in Chapter 2. For such situation, fluctuating boundary conditions (FBC) have been implemented to properly accommodate incommensurabilities, enabling the FSS to be useful.

In the AFM case, i.e. $J < 0$, the ground state configuration of the model would be also restricted to lie in planes perpendicular to the DM vector, but the spin vectors now would arrange themselves in an antiparallel way, with any spin and its nearest neighbor in the lattice having an azimuthal angular difference equal to $\pi - \phi(d)$, as was depicted in the bottom sketches in Figure 2. This means that one lattice spacing displacement implies in a $\pi - \phi(d)$ rotation of the next spin vector, giving rise to a modulation of the spin vectors as discussed in the above paragraph. Some attention should be paid to the signal of $\phi(d)$ in Equation (3.3), which changes into $-\phi(d)$ in the cosine argument due to the ratio $d = D/J$.

This work will be focused only on the FM case, though the AFM case could be studied in a very similar approach and eventually leading to similar conclusions about the critical behavior of the antiferromagnetic model with DM interaction. Thus, through MC simulations and FSS analyses, this chapter will extend some of the procedures used in Chapter 2 for the two-dimensional planar rotator model with DM interaction to analyze the three-dimensional Heisenberg model with DM interaction according to the Hamiltonian (3.3). Some initial conventions is adopted here, such as setting the lattice spacing as $a = 1$ and the finite system being represented as $L \times L \times L$ cubic lattices with $N = L^3$ sites. The spin magnitude is fixed as $S = 1$ in Equation (3.3). The next section presents the MC simulation details and the boundary conditions used in the simulations.

3.2 Computational methods

3.2.1 Monte Carlo algorithm

Since the Hamiltonian (3.3) of the considered model is represented in spherical coordinates where all the spin vectors have constant magnitude, the spin orientations can be changed through their azimuthal angles and polar angles. In the simulations, the change of the spin angles was performed by using the single-spin Metropolis algorithm [48]. During one sequential sweep of all sites in the lattice it is tried to modify the angles $(\theta_i^{old}, \varphi_i^{old})$

of each spin vector into new random ones, $(\theta_i^{new}, \varphi_i^{new})$. According to Equation (3.4), the attempt of changing $(\theta_i^{old}, \varphi_i^{old})$ is done by introducing two independent random numbers uniformly distributed between 0 and 1, which are written as u_1 and u_2. The inverse cosine function is defined in the domain $[-1, 1]$ and its image is set in the interval $[0, \pi]$. This detail is important to correctly sample the polar angles from the given interval. The new angles will be accepted if the total energy difference ΔE becomes smaller than zero or if the Boltzmann probability of the total energy difference ΔE is greater than a random number u_3 uniformly distributed between 0 and 1. If this last condition does not occur, the spin angles remain unchanged, i.e $(\theta_i^{new}, \varphi_i^{new}) = (\theta_i^{old}, \varphi_i^{old})$.

$$(\theta_i^{old}, \varphi_i^{old}) \to (\theta_i^{new}, \varphi_i^{new}) = \begin{cases} (\cos^{-1}(1-2u_1), 2\pi u_2) & \text{if} \quad \Delta E < 0 \text{ or } e^{-\Delta E/(k_B T)} \geq u_3 \\ (\theta_i^{old}, \varphi_i^{old}) & \text{if} \quad e^{-\Delta E/(k_B T)} < u_3 \end{cases} \tag{3.4}$$

3.2.2 Boundary conditions

In Subsection 2.2.2 it was discussed how to properly define the boundary condition according to the match between spin structure and finite lattice. This can be easily verified from the ratio $L/\ell(d)$, as previously mentioned. Alternatively, one can check if the modulation length due to the DM interaction, measured by the parameter d, is commensurate or incommensurate with the lattice size L, by considering the phase shift angle $\Delta(d, L)$ in the interval $[0, 2\pi)$, which was already defined in Subsection 2.2.2, given by

$$\Delta(d, L) = \text{mod}[L\phi(d), 2\pi], \tag{3.5}$$

with $\phi(d)$ being the pitch angle and "mod" being the modulo operation. In the case of the ground-state spin configuration at $T = 0$, if $\Delta(d, L) = 0$ the configurations are commensurate with the lattice. Otherwise, when $\Delta(d, L)$ differs from zero, an incommensurability takes place. In fact, the phase shift angle $\Delta(d, L)$ may be seen as a measurement of the incommensurability level, as was suggested in Subsection 2.3.5 and illustrated in Figure 20, which shows $\Delta(d, L)$ as function of L for several values of d using Equation (3.5).

In the fluctuating boundary condition (FBC), adopted for the incommensurability situations in the previous chapter, the phase shift angle Δ is random valued, being calculated by an extra Metropolis sweep of the sites on the boundary of the lattice. In this case, for $0 < T < T_c$, Δ follows a Gaussian distribution, as shown in Figure 19, with its mean value being almost constant as the temperature increases in the specified temperature interval, meanwhile the distribution width increases as well. Strikingly, the constant mean value of Δ has been in a quite good agreement with the phase shift angle obtained from Equation (3.5). This finding motivates using $\Delta(d, L)$ for $T = 0$ to compensate the azimuthal angular differences $\varphi_i - \varphi_j$, for the spins i and j along the boundary of the lattice, by imposing $\varphi_i + \Delta(d, L) - \varphi_j$. If one wishes to study the AFM

version of the model, it would only be necessary to make the change $\phi(d) \to \pi - \phi(d)$ in Equation (3.5).

Based on these considerations, two different boundary conditions were defined for the simulations. One uses Δ calculated from Equation (3.5), which remains fixed during the entire simulation. The other one uses the random-value Δ calculated from the Metropolis algorithm mentioned in the previous paragraph. For convenience, the use of a constant Δ in the angular differences for spins at sites on the boundary will be referred to as *shifted boundary condition* (SBC). It should be noticed that whenever $\Delta(d, L) = 0$, SBC becomes identical to the usual periodic boundary condition (PBC), which reads

$$(\theta_{x,y,L}, \varphi_{x,y,L}) = (\theta_{x,y,0}, \varphi_{x,y,0}), \tag{3.6a}$$

$$(\theta_{x,L,z}, \varphi_{x,L,z}) = (\theta_{x,0,z}, \varphi_{x,0,z}), \tag{3.6b}$$

$$(\theta_{L,y,z}, \varphi_{L,y,z}) = (\theta_{0,y,z}, \varphi_{0,y,z}), \tag{3.6c}$$

with x, y and z varying in the interval $[0, L-1]$.

Previously, the phase shift angle for each direction of a square lattice, namely x- and y-directions, was equally determined for both directions from the FBC algorithm applied to the whole boundary, as can be seen in Equations (2.13a) and (2.13b). In the present study, for simulations with FBC, it was defined Δ_x, Δ_y and Δ_z to be added to the azimuthal angular differences on the boundary for each direction in the lattice as follows,

$$\varphi_{x,y,L-1} - \varphi_{x,y,0} \to \varphi_{x,y,L-1} + \Delta_z - \varphi_{x,y,0}, \tag{3.7a}$$

$$\varphi_{x,L-1,z} - \varphi_{x,0,z} \to \varphi_{x,L-1,z} + \Delta_y - \varphi_{x,0,z}, \tag{3.7b}$$

$$\varphi_{L-1,y,z} - \varphi_{0,y,z} \to \varphi_{L-1,y,z} + \Delta_x - \varphi_{0,y,z}, \tag{3.7c}$$

where each phase shift angle is calculated independently to each other. In this way, after one sweep with Metropolis algorithm in the whole lattice, there is one additional step to sweep all the spins on the boundary and to compute each phase shift angle based on the prescription given by Equation (2.14), in which here it turns into

$$\Delta_i^{old} \to \Delta_i^{old} + \delta_i \Rightarrow \Delta_i^{new} = \begin{cases} \Delta_i^{old} + \delta_i & \text{if } \Delta E_{i=L-1} < 0 \text{ or } e^{-\Delta E_{i=L-1}/(k_B T)} \geq u_i, \\ \Delta_i^{old} & \text{if } e^{-\Delta E_{i=L-1}/(k_B T)} < u_i, \end{cases} \tag{3.8}$$

where $i = x, y, z$ and $\Delta E_{i=L-1}$ is the energy difference relative to an attempt of changing Δ_i^{old} into $\Delta_i^{old} + \delta_i$ regarding the spins at sites in the boundary plane $i = L-1$ and their correspondent neighbors in the plane $i = 0$, according to PBC definition (3.6). Again, δ_i is a small random increment and u_i is a random number uniformly distributed between 0 and 1.

Recalling some cases of different d values studied in Chapter 2, examples of spin configurations that are commensurate with finite lattice sizes can be listed as: (*i*) $d = 0$ for any value of L because $\ell(0) = \infty$ (due to $\phi = 0$); (*ii*) $d = 1$ for $L = n \times \ell(1)$ with

$n = 1, 2, ...$ and $\ell(1) = 8$; (*iii*) $d = \infty$ for $L = n \times \ell(\infty)$ with $\ell(\infty) = 4$. In all of the above cases, SPC and PBC produce same results. However, for $d = 0.5$, for example, it implies $\ell(0.5) = 13.55...$ which leads to an unavoidable incommensurability case for any finite lattice sizes.

3.2.3 Simulation details

As can be seen in Table 4, in this study one MC step per spin (MCS) is defined by a sequential sweep of all the spins of the lattice using the single-spin Metropolis algorithm described in Subsection 3.2.2 for simulations with SBC whereas for simulations with FBC there is an additional sweep of the spins belonging to the boundary of the lattice using the Metropolis algorithm. This extra sweep is to update the phase shift angles Δ_x, Δ_y and Δ_z in the FBC by the prescription in Equation (3.8). For the SBC, all of the three phase shift angles are equal to each other, being computed through Equation (3.5) before the simulation starts.

Table 4 – One Monte Carlo step per spin (MCS) definition according to the used boundary condition, which may be shifted boundary condition (SBC) or fluctuating boundary condition (FBC).

One MCS (SBC)	**One MCS (FBC)**
One sweep with Metropolis algorithm	One sweep with Metropolis algorithm
—	One sweep with Metropolis algorithm on the boundary

Before starting the MC simulation for any $L \times L \times L$ cubic lattice, a similar procedure to those one described in Subsection 2.2.3 to obtain stable configurations in the thermal equilibrium was repeated in the simulations of this model. These configurations are kept in files to be used as initial configurations in other simulations at the same temperature in which they were obtained or in other simulations at closely temperatures. Then, they were saved in files after an amount of MCS discarding ranging between 10^5 and 10^6, which depends on the lattice size being simulated. Most of the used sizes ranged from $L = 8$ to $L = 56$. For some extra analysis, lattices with $L = 64$ were also simulated. Here, large lattices have been those ones with $L > 32$. Thus, for simulations of large lattices, the saved initial configurations were used, whereas simulations of smaller lattices started from random configurations, but with measurements only being taken after the MCS discarding.

Due to the present model being three-dimensional, the amount of MCS in one MC simulation per lattice (MCSL) had to be decreased in relation to the amount used in the two-dimensional model of Chapter 2. In this case, one MCSL consisted of 10^6 MCS after equilibration, with measurements being taken every 10 MCS. Equilibration means that the MCS discarding was done before this step. The 10-MCS skipping reduces the correlation between configurations in the MCS sequence [6]. After a MCSL finishes, the measured quantities, namely energy and order parameter, are stored in a file contained 10^5 rows

with two columns filled out with the respective quantities. Optionally, another similar file is also generated in the simulation ending, but containing the three phase shift angles of the FBC. Again, the random number generator implemented in the simulations was the algorithm "ran2" in Reference [50].

Two different approaches have been adopted to perform the MC simulations in this study:

1º approach - It refers to finer analysis by employing single histogram reweighting [6] techniques in resulting data from sets of MCSL done at the same values of temperature and DM interaction, where the MCSL run independently of each other on different processor cores and start with different random number generator seed. This approach is identical to the simulation procedure in Subsection 2.2.3. The data consist of all the files generated at just one temperature value. Here, 300 MCSL (corresponding to 3×10^7 measurements) were done for $L = 8$ and 800 MCSL (corresponding to 8×10^7 measurements) for $L = 56$.

2º approach - No histogram techniques are used here and data result from sets of MCSL done at different temperature values in some specified range, but at a same value of DM interaction. The MCSL run independently of each other on different processor cores and start with different random number generator seed. The resulting data consist of all the files generated at different temperature values. 1 MCSL (corresponding to 10^5 measurements) was done at each temperature for all considered lattice sizes, which ranged between $L = 8$ and $L = 64$.

3.2.4 Thermodynamic quantities and finite-size scaling relations

The energy E, measured during the MC simulations, is computed by using the Hamiltonian of the model, i.e. $E = \mathcal{H}$, with $\mathcal{H}$ given by Equation (3.3). The magnetization per spin $\mathcal{M}$, defined by Equation (2.15), presents a similar behavior to that one seen for the two-dimensional model version studied in Chapter 2. Once at $T = 0$ and $d \neq 0$ all spin vectors remain confined in planes perpendicular to the DM vector, for the present three-dimensional model, the magnetization per spin of the ground state configurations results in

$$\mathcal{M}(L, \phi) = \left| \frac{\sin(L\phi/2)}{L \sin(\phi/2)} \right|^3 , \tag{3.9}$$

which is a function of the lattice size L, and the pitch angle $\phi = \tan^{-1} d$. Although in this case $\mathcal{M}$ differs from zero for finite lattices, it goes to zero in the thermodynamic limit, i.e. $\mathcal{M}(L, \phi) \to 0$ as $L \to \infty$ for $d \neq 0$. In the $d \to 0$ limit, $\mathcal{M}(L, \phi) \to 1$, which is expected, since $d = 0$ is just the three-dimensional isotropic Heisenberg model.

The full line in the graph on the left in Figure 22 gives the behavior of $\mathcal{M}$ from Equation (3.9), as a function of the lattice size L, for a small pitch angle corresponding to

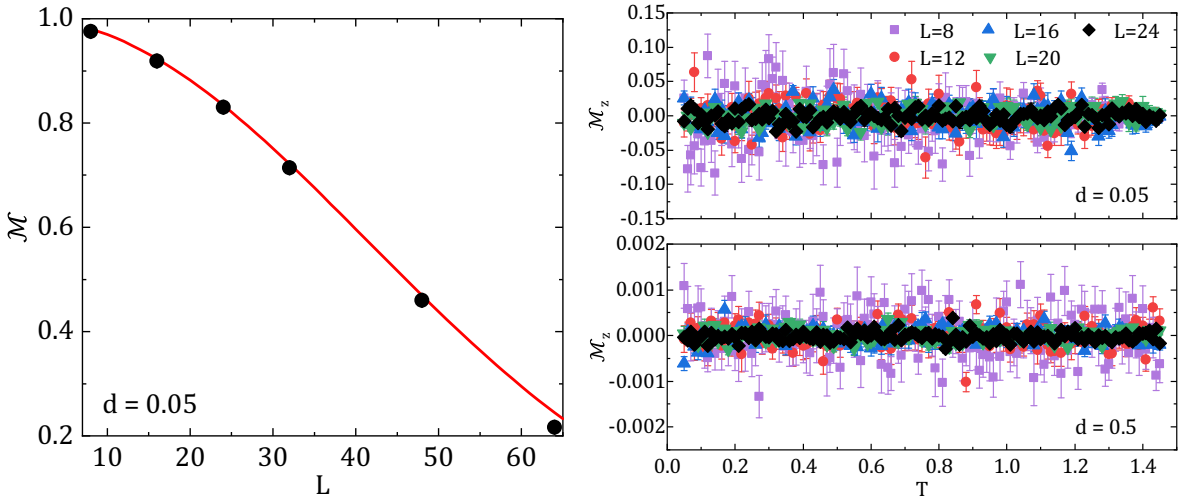

Figure 22 – (Left panel) Magnetization per spin $\mathcal{M}$ as a function of the lattice size L for a small value $d = 0.05$. The solid line corresponds to the theoretical result at $T = 0$, given by Equation (3.9) in a simple cubic lattice. The circles are MC simulation results at low temperature, namely $T = 0.025$. The error bars of the MC estimates are smaller than the symbol sizes. (Right panels) MC results of the z-component magnetization per spin $\mathcal{M}_z$, as a function of the temperature T, for different lattice sizes, at $d = 0.05$ (top panel) and $d = 0.5$ (bottom panel).

$d = 0.05$. The circles correspond to MC simulation results for the same value of d and for a very low temperature, $T = 0.025$. The adopted convention in Chapter 2 of measuring temperature in units of k_B/J is still held. The agreement seen in this figure shows that $T = 0.025$ is low enough to capture the essence of the ground state configuration.

Even when the temperature increases from such a low value, the spin vectors are still forced to closely stay in planes perpendicular to the DM vector. This can be seen from the behavior of the z-component magnetization $\mathcal{M}_z = \left(\sum_{i=1}^{L^3} S_i^z\right) \Big/ L^3$ as the temperature increases. The right panels in Figure 22 show the results from MC simulations at $d = 0.05$ and $d = 0.5$ and different lattice sizes. $\mathcal{M}_z$ fluctuates around zero with the magnitude of its fluctuation decreasing as d increases in the whole temperature range. Furthermore, $\mathcal{M}_z$ seems to tend to zero as the lattice size tends to infinity. It is also interesting to notice that the DM interaction forces the spins to stay in perpendicular planes even for smaller lattices, since the fluctuations decrease two orders of magnitude when $d = 0.5$ even for the smaller lattice $L = 8$.

As a consequence due to the presence of the DM interaction in the model, the magnetization per spin $\mathcal{M}$ no longer can be used as an order parameter (despite the fact that, as the temperature increases, the magnetization per spin falls off its value at $T = 0$ for each value of L and approaches zero).

Motivated by the previous order parameter definition shown in Equation (2.17), an

appropriate order parameter m has been defined for this model as

$$m = \frac{1}{N}\left(\left\{\sum_{i=1}^{N}\cos[\varphi_i + (x_i + y_i + z_i)\phi]\sin\theta_i\right\}^2 + \left\{\sum_{i=1}^{N}\sin[\varphi_i + (x_i + y_i + z_i)\phi]\sin\theta_i\right\}^2 + \left(\sum_{i=1}^{N}\cos\theta_i\right)^2\right)^{1/2}, \tag{3.10}$$

which depends not only on the spin spherical angles, but also on their positions in the lattice and the pitch angle ϕ. Ultimately, the terms $(x_i + y_i + z_i)\phi$ in this equation have the effect of undoing the modulations of the spin vectors caused by the presence of the DM interaction, remembering that $x_i, y_i, z_i \in [0, L-1]$. As a result, for any finite lattice $m = 1$ in the ground state and decreases to zero as the temperature increases, playing the perfect role of an order parameter.

The critical temperature of the model for some d value can be computed by using the fourth-order cumulant U_4 of the order parameter m, which was already defined in its reduced form in Equation (2.18). For sufficiently large systems and assuming a second-order phase transition, this cumulant as a function of temperature should cross at the same point T_c for different values of L. T_c is thus the critical temperature and the cumulant U_4^* at T_c has a universal value. In addition, the slopes of U_4 at T_c are proportional to $L^{-1/\nu}$, where ν is the correlation length critical exponent. These properties of U_4 allow an almost unbiased estimate of T_c, U_4^* and ν [6, 63].

As could be observed in the previous study, finite lattices that are not large enough may give rise to residual corrections to the finite-size scaling (FSS) [53], making the crossing points of the cumulant U_4 suffer a systematic shift as L varies. This also happens in the present model, as will be seen up ahead. However, if $T_{\text{cross}}(L, L_s)$ is the crossing temperature of the cumulants for lattice sizes L and L_s, where L_s is fixed and taken as a reference lattice size, the systematic deviations of this quantity can be modeled as [6, 63]

$$T_{\text{cross}}(L, L_s) = T_c(\infty, L_s) + \frac{B_T}{\log_{10}(L/L_s)}, \tag{3.11}$$

where $T_c(\infty, L_s)$ provides an estimate of the critical temperature of the infinite system and B_T is a non-universal constant.

Similarly to Equation (3.11), the cumulant values at $T_{\text{cross}}(L, L_s)$, namely $U_4^*(L, L_s)$, can be modeled as

$$U_4^*(L, L_s) = U_4^*(\infty, L_s) + \frac{B_U}{\log_{10}(L/L_s)}, \tag{3.12}$$

where $U_4^*(\infty, L_s)$ provides an estimate of the cumulant for the infinite lattice and B_U is another non-universal constant.

Since both $T_c(\infty, L_s)$ and $U_4^*(\infty, L_s)$ could still depend on the reference lattice L_s, one eventually obtains the critical temperature T_c and the fourth-order cumulant U_4^* in the limit $L_s \to \infty$, namely $T_c = T_c(\infty, \infty)$ and $U_4^* = U_4^*(\infty, \infty)$. In the present case, it

was possible to obtain reasonable resolution for the cumulant crossings with $L_s = 8$, 12, 16 and 20, where the crossings have been taken with $L > L_s$ for all values of L_s.

Once the critical temperature is determined, the critical exponents of the correlation length ν, order parameter β, susceptibility of the order parameter γ, and specific heat α, can be estimated from the FSS relations

$$\left.\frac{dU_4(\beta_T; L)}{d\beta_T}\right|_{\beta_T=\beta_{T_c}} \approx U_0 L^{-1/\nu}, \tag{3.13}$$

$$m(T = T_c; L) \approx m_0 L^{-\beta/\nu}, \tag{3.14}$$

$$\chi_{\text{peak}}(L) \approx \chi_0 L^{\gamma/\nu}, \tag{3.15}$$

$$C_{\text{peak}}(L) \approx C_\infty + C_0 L^{\alpha/\nu}, \tag{3.16}$$

where $U_0,\ m_0,\ \chi_0, C_\infty$ and C_0 are constants. Equation (3.13) corresponds to the derivative of the fourth-order cumulant with respect to the variable $\beta_T = 1/k_B T$ and is taken at the critical temperature, which may be calculated by using the following result [63],

$$\frac{dU_4(\beta_T; L)}{d\beta_T} = [1 - U_4(\beta_T; L)]\left[\langle E\rangle - 2\frac{\langle m^2 E\rangle}{\langle m^2\rangle} + \frac{\langle m^4 E\rangle}{\langle m^4\rangle}\right]. \tag{3.17}$$

Equation (3.14) is the order parameter at T_c. Equation (3.15) is the peak value of the order parameter susceptibility χ, which is defined by

$$\chi = \frac{L^3\left[\langle m^2\rangle - \langle m\rangle^2\right]}{k_B T}, \tag{3.18}$$

and Equation (3.16) is the peak value of the specific heat C given by

$$C = \frac{\langle E^2\rangle - \langle E\rangle^2}{L^3 k_B T^2}. \tag{3.19}$$

More detail about the nature of the phase transition is given by the structure factor [6], which provides information about the spin-spin correlations and the magnetic long-range ordering. This quantity is defined by the spatial Fourier transform of the time-independent pair-correlation function $\Gamma(\boldsymbol{r}_{jk}) = \langle \boldsymbol{S}_j \cdot \boldsymbol{S}_k\rangle - \langle \boldsymbol{S}_j\rangle \cdot \langle \boldsymbol{S}_k\rangle$ of the spin configurations in thermal equilibrium, with $\boldsymbol{r}_{jk} = \boldsymbol{r}_j - \boldsymbol{r}_k$ being the relative vector position of the spins at j and k sites, respectively (the lattice parameter has been normalized to unity). Accordingly, the static structure factor $\mathcal{S}(\boldsymbol{q})$ can be written as

$$\mathcal{S}(\boldsymbol{q}) = \frac{1}{L^3}\sum_{j,k}\Gamma(\boldsymbol{r}_{jk})\, e^{i\boldsymbol{q}\cdot\boldsymbol{r}_{jk}}, \tag{3.20}$$

where $\boldsymbol{q}$ is the wave vector and the double summation runs over all the spins in the lattice. This structure factor is also very useful to investigate the magnetic structures emerging from complex arrangements of the spins, as well as distinguishing different magnetic phases [64, 65].

The MC simulations following the first approach in the previous subsection were utilized to accurately estimate the critical temperature T_c and the value of the fourth-order cumulant U_4^*. For this purpose, Equations (3.10)-(3.12) have been used, plus Equation (2.18) of the fourth-order cumulant and its derivative, given by Equation (3.17). The critical exponent ν and the ratio β/ν have been estimated through the FSS relations given by Equations (3.13) and (3.14). This process was done for different values of d with SBC and FBC, taking an estimated CPU time of the order 7×10^5 core-hours.

In turn, the MC simulations described in the second approach were done in order to obtain the susceptibility of the order parameter and specific heat curves as a function of T directly from the simulations by using Equations (3.18) and (3.19). Then, the ratios γ/ν and α/ν have been estimated from the FSS relations given by Equations (3.15) and (3.16). Additional estimates of T_c, using the FSS of the temperatures where the susceptibility of the order parameter and specific heat take place, have been obtained as well. The computation of the structure factor $\mathcal{S}(\boldsymbol{q})$ has been also done following the second approach, but for lattice sizes $L \leq 24$. Again, the whole procedure was done for different values of d with SBC and FBC. Compared to the set of simulations in the above paragraph, there was less computational effort in this part, with an estimated 10^5 core-hours for simulations related to the susceptibility of the order parameter and specific heat, and only 2000 core-hours for simulations related to the structure factor.

The averages and corresponding uncertainties of the needed quantities to extract the results have been computed using standard procedures described in Appendix A. The histogram technique involved in the calculations are described in Appendix B, and shortly ahead, the process of computing the cumulant crossings and respective error bars are also specified in Appendix C.

3.3 Results

In this section, the results for three particular regimes of d will be focused on. The first one is when $d = 0$, which is the well-known Heisenberg model that has no spin modulation but only FM ordering at low temperatures. In this case, comparison of the present results with previous simulations can also be made. As an intermediate regime, $d = 0.5$ is considered, having a spin modulation length $\ell = 13.55...$, which results in an unavoidable incommensurability for any finite lattice size. In some cases, $d = 1$ will also be considered, where commensurate lattices are obtained when $L = n \times \ell$, with $n = 1, 2, ...$ and $\ell = 8$.

The third regime is when d tends to infinity and the DM interaction dominates, i.e. a three-dimensional "DM model" containing only DM interactions. This regime will be referred to as $d = \infty$, where the second term involving cosines in Equation (3.3) can be neglected. This case results in the shortest possible spin modulation length, $\ell = 4$,

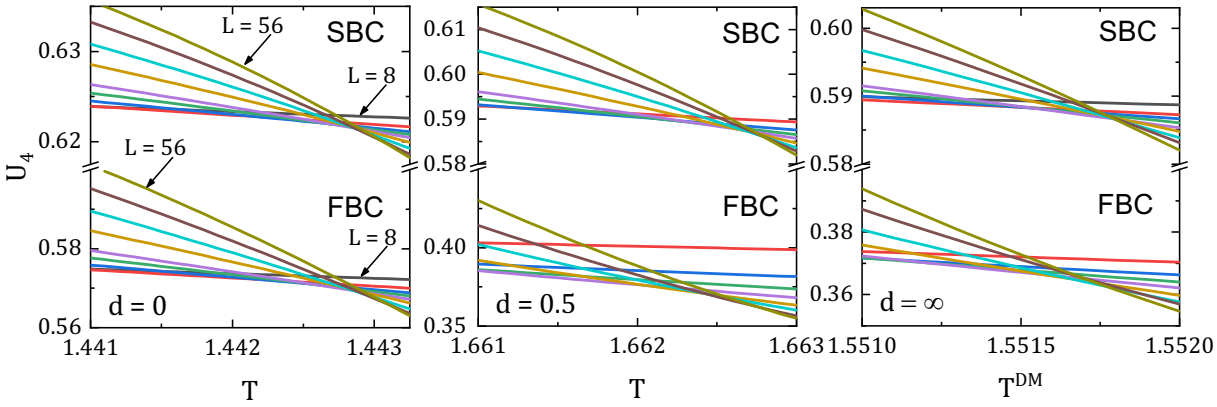

Figure 23 – Fourth-order cumulant of the order parameter U_4 as a function of temperature T for $d = 0$ (left panel), $d = 0.5$ (middle panel), and $d = \infty$ (right panel - where $T^{\mathrm{DM}} = \left[\beta_T J\sqrt{1+d^2}\right]^{-1}$ in the $d = \infty$ limit). The lattice sizes range from $L = 8$ to $L = 56$, as specified in the text. In each panel, the top curves are for SBC and the bottom curves are for FBC (there are two different scales in the vertical axes for each boundary condition). The lattice size pattern in the graph on the left also applies to the other two graphs.

corresponding to four lattice spacings. Similarly to the case $d = 1$, the incommensurability can thus be circumvented by choosing lattice sizes $L = n \times \ell$.

In the $d = \infty$ limit, where the cosines term can be neglected, the simulations provide a transition where

$$\left[\beta_{T_c} J\sqrt{1+d^2}\right]^{-1} = T_c^{\mathrm{DM}} \tag{3.21}$$

plays the role of the critical temperature of the DM model. In addition, from Equation (3.21) one has (recalling that it was fixed $k_B = 1$ and $J = 1$)

$$T_c = T_c^{\mathrm{DM}} d. \tag{3.22}$$

The above equation also gives the slope of the transition temperature line $T_c(d)$, as a function of d, in the $d = \infty$ limit. This feature will become clearer in Subsection 3.3.2, when the global phase diagram is discussed.

In all the above three different regimes, both SBC and FBC are considered and their respective results are compared.

3.3.1 Critical temperature and universal fourth-order cumulant

Figure 23 shows the order parameter fourth-order cumulants, defined in Equation (2.18), as a function of the temperature T for $d = 0$, $d = 0.5$ and $d = \infty$. The temperature T^{DM}, in the $d = \infty$ limit, is given by $T^{\mathrm{DM}} = \left[\beta_T J\sqrt{1+d^2}\right]^{-1}$. For each graph, there are two sets of curves constructed by using the histogram method and taking the data from MC simulations with SBC and FBC.

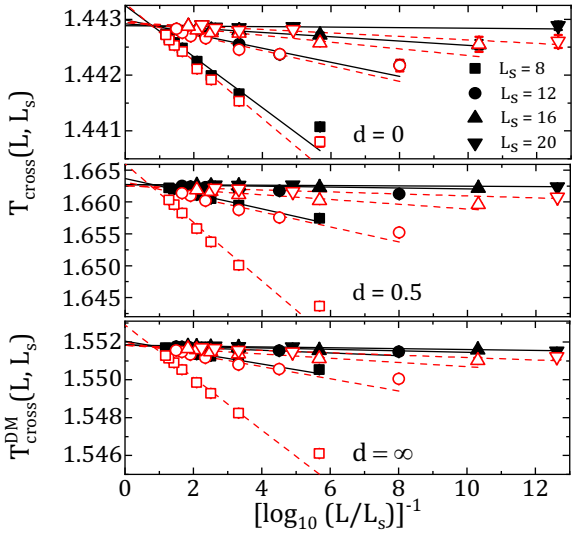

Figure 24 – Crossing temperatures $T_{\text{cross}}(L, L_s)$ and $T^{\text{DM}}_{\text{cross}}(L, L_s)$, as a function of $[\log_{10}(L/L_s)]^{-1}$, for $d = 0$ (top panel), $d = 0.5$ (middle panel) and $d = \infty$ (bottom panel). Different symbols correspond to different reference sizes L_s. Full symbols and full lines correspond to SBC, while open symbols and dashed lines to FBC. Both types of lines are linear fits according to Equation (3.11). The legend in the top panel also applies to the other panels. Where not shown, the error bars are smaller than the symbol sizes.

Independent of the chosen boundary conditions, the systematic deviations of the cumulant crossings in Figure 23 are remarkable for all considered values of d as the lattice size changes. Nevertheless, the crossing temperatures $T_{\text{cross}}(L, L_s)$ were computed for $L_s = 8, 12, 16$ and 20, with $L > L_s$. The values of $T_{\text{cross}}(L, L_s)$ and their error bars have been estimated by approximating the cumulants as linear functions of T in the regions where the crossings occur, with temperature steps $\Delta T = 0.0001$, as detailed in Appendix C. The above process has also been used in obtaining $T^{\text{DM}}_{\text{cross}}(L, L_s)$.

The results for the crossing temperatures $T_{\text{cross}}(L, L_s)$ and $T^{\text{DM}}_{\text{cross}}(L, L_s)$, as a function of $[\log_{10}(L/L_s)]^{-1}$, are depicted in Figure 24 for the three values of d with SBC and FBC. The straight lines are fits based on Equation (3.11) that provide a partial estimate of the critical temperature $T_c(\infty, L_s)$. There have been different scaling behaviors for different reference lattices L_s, as can be observed in the graphs of this figure. Although for $d = 0$ the FSS functions are comparable for SBC and FBC, for $d \neq 0$ different boundary conditions lead to different scaling behavior. The extrapolated values of $T_c(\infty, L_s)$ can be checked in Table 5. Additionally, there are results for $d = 1$ in this table, but only for SBC.

Despite the difference in the scaling functions shown in Figure 24, in all cases the extrapolated temperatures smoothly converge to a single value as the reference lattice becomes larger. This convergence can be seen in Figure 25, that depicts $T_c(\infty, L_s)$ and $T^{\text{DM}}_c(\infty, L_s)$, as a function of $1/L_s$ obtained for the values of d shown in Table 5. One can clearly see that as L_s becomes larger, the critical temperature tends to a constant,

Table 5 – Extrapolated values from the fits in Figure 24 for the critical temperature $T_c(\infty, L_s)$ in the $L \to \infty$ limit for each reference lattice size L_s. The results for both of the boundary conditions used in the simulations, SBC and FBC, are shown for each value of d, except for $d = 1$, which the simulations were performed using only SBC. For $d = \infty$, the temperature T_c must be read as T_c^{DM} instead, where it follows from the definition in Equation (3.21). The last column shows the final estimates of the critical temperature according to the d value and boundary condition, written as $T_c(d)$, resulting from the extrapolated values, as described in the text.

	Extrapolated values				**Final estimate**
d	$T_c(\infty, 8)$	$T_c(\infty, 12)$	$T_c(\infty, 16)$	$T_c(\infty, 20)$	$T_c(d)$
0 (SBC)	1.44325(2)	1.44299(2)	1.44292(2)	1.44289(2)	1.44293(5)
0 (FBC)	1.44329(2)	1.44230(2)	1.44295(3)	1.44294(3)	1.44296(2)
0.5 (SBC)	1.66376(1)	1.66297(2)	1.66282(2)	1.66280(2)	1.66281(1)
0.5 (FBC)	1.66633(3)	1.66340(3)	1.66272(3)	1.66260(4)	1.66272(3)
1 (SBC)	2.14743(2)	2.14698(2)	2.14690(3)	2.14689(4)	2.14692(5)
∞ (SBC)	1.55204(1)	1.55184(1)	1.55183(1)	1.55183(2)	1.55183(1)
∞ (FBC)	1.55289(3)	1.55199(3)	1.55181(3)	1.55181(4)	1.55181(2)

furnishing then $T_c = T_c(\infty, \infty)$, for any value of d. Considering the extrapolated values in Table 5, the final estimates of T_c as a function of d, shown as $T_c(d)$ in the table, have been obtained by discarding the smaller reference lattice $L_s = 8$ in all cases and only averaging the remaining data that have their T_c estimates agreeing with each other within the error bars. This implies that some results of $T_c(d)$ come only from the largest reference lattice $L_s = 20$. As expected, for any DM interaction d, the estimated values of $T_c(d)$ are the same, regardless of the type of boundary condition.

Evaluating the cumulants $U_4^*(L, L_s)$, and the corresponding errors at the crossing temperatures $T_{\text{cross}}(L, L_s)$ or $T_{\text{cross}}^{\text{DM}}(L, L_s)$ is now straightforward using the already-computed histograms, i.e. using Equation (B.7) to obtain the cumulants from Equation (2.18). The reference lattice L_s were chosen to compute the fourth-order cumulants $U_4^*(L, L_s)$ so that the estimates had the smallest possible errors. The results can be seen in Figure 26, showing $U_4^*(L, L_s)$, as a function of $[\log_{10}(L/L_s)]^{-1}$, at the crossing temperatures $T_{\text{cross}}(L, L_s)$. The lines are linear fits using Equation (3.12), from which one obtains the extrapolated cumulant $U_4^*(\infty, L_s)$. The numerical results are shown as extrapolated values in Table 6. Similarly to the FSS behavior of the crossing temperatures, different FSS behaviors also occur for each reference lattice L_s and for all values of d. However, in this case, the extrapolated values of cumulants not only seem to depend on the boundary conditions but also whether d is zero or non-zero.

In order to better see the effects of the boundary conditions and the DM interaction on the cumulant value at the transition, Figure 27 shows $U_4^*(\infty, L_s)$, as a function of $1/L_s$, for different values of d and also $d = 1$ with SBC. Extra linear fits were performed in

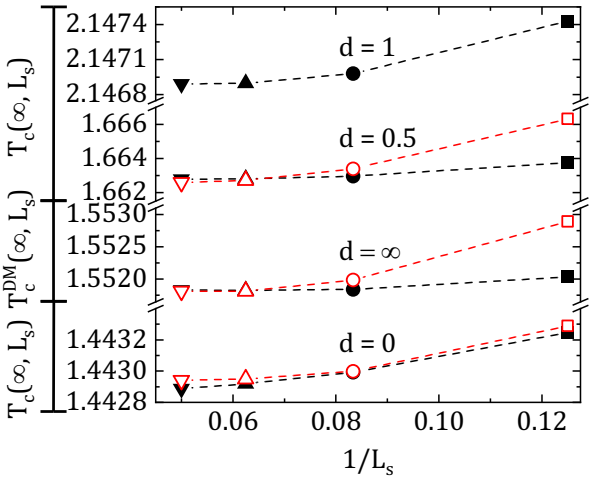

Figure 25 – Extrapolated values of the crossing temperatures $T_{\text{cross}}(\infty, L_s)$ and $T_{\text{cross}}^{\text{DM}}(\infty, L_s)$ from the fits of Figure 24, as a function of $1/L_s$, for different DM interaction d. SBC correspond to full symbols and FBC to open symbols. The numerical data in this graph can be seen in Table 5. The case $d = 1$ with only SBC has also been added in this figure. The temperature axis has different scales for different values of d. The error bars are smaller than the symbol sizes.

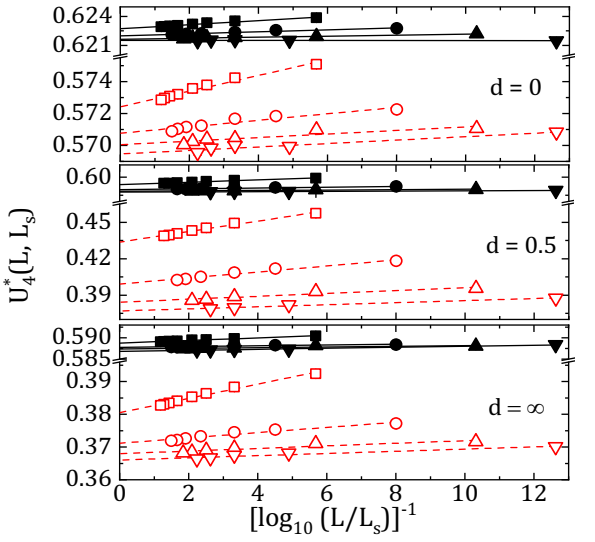

Figure 26 – Value of the cumulants $U_4^*(L, L_s)$, at the crossing temperatures $T_{\text{cross}}(L, L_s)$ or $T_{\text{cross}}^{\text{DM}}(L, L_s)$, as a function of $[\log_{10}(L/L_s)]^{-1}$, computed from the simulation data of the reference lattice of size L_s. The description of DM interaction, symbols, and lines given in Figure 24 also applies to this figure (with the linear fits coming from Equation (3.12) instead). The error bars are smaller than the symbol sizes.

Table 6 – Extrapolated values of the fixed value $U_4^*(\infty, L_s)$ in the $L \to \infty$ limit for each reference lattice size L_s. The results for both of the boundary conditions used in the simulations, SBC and FBC, are shown for each value of d, except for $d = 1$, which the simulations were performed using only SBC. The last column shows the final estimates of the universal fourth-order cumulant according to the d value and boundary condition, written as $U_4^*(d)$, resulting from straight line fits in the extrapolated values, as shown in Figure 27 and described in the text.

	Extrapolated values				**Final estimate**
d	$U_4^*(\infty, 8)$	$U_4^*(\infty, 12)$	$U_4^*(\infty, 16)$	$U_4^*(\infty, 20)$	$U_4^*(d)$
0 (SBC)	0.62272(2)	0.62200(2)	0.62163(3)	0.62153(3)	0.6208(1)
0 (FBC)	0.57241(5)	0.57077(6)	0.57006(9)	0.5695(1)	0.5679(2)
0.5 (SBC)	0.59369(3)	0.58975(4)	0.58837(8)	0.58760(9)	0.58434(9)
0.5 (FBC)	0.4336(2)	0.3988(2)	0.3838(3)	0.3768(3)	0.3488(2)
1 (SBC)	0.58998(3)	0.58817(5)	0.58745(6)	0.58712(9)	0.5854(1)
∞ (SBC)	0.58879(3)	0.58778(4)	0.58739(6)	0.58684(6)	0.5856(4)
∞ (FBC)	0.3805(2)	0.3712(2)	0.3680(2)	0.3660(2)	0.35836(4)

the data to estimate U_4^*, as can be seen by the full straight lines in Figure 27. In this procedure, the points with $L_s = 8$ have not been taken in the fits for all of the d values and boundary condition, except for $d = 0.5$ FBC, which U_4^* was obtained from the vertical axis intercept of the straight line defined by the points with $L_s = 16$ and $L_s = 20$. For this case, the error associated with the U_4^* estimate was obtained by propagating the error from the two points used to define the straight line. The corresponding numerical results from this procedure are the final estimates of $U_4^*(d)$, shown in the last column of Table 6. For $d = 0$, the results are almost independent of L_s for both boundary conditions, and the fits yield $U_4^* = 0.6208(1)$ for SBC and $U_4^* = 0.5679(2)$ for FBC. In the end of Subsection 2.3.5 was pointed out that U_4^* has different values when one uses data from MC simulations with PBC or FBC. Those results and the ones in Table 6 make it clear that, as in other models, the cumulant does depend on the boundary conditions [59].

For $d \neq 0$, the finite-size effects become stronger, mainly for FBC. Interestingly, with SBC, for different values of d the cumulants $U_4^*(\infty, L_s)$ clearly converge to the same result as L_s becomes larger. On the other hand, despite stronger finite-size behavior for FBC, the results also seem to converge to the same result, but with a different value as compared to the SBC, as one can see by the final estimates of $U_4^*(d)$ listed in Table 6. Surely the cumulants at T_c for any $d \neq 0$ seem to have the same value (within the error bars) with SBC. With FBC they are outside of the error bars, but still quite comparable. However, U_4^* for SBC and U_4^* for FBC are definitely different from each other. An average furnishes $U_4^* = 0.5851(7)$ for SBC and $U_4^* = 0.3536(69)$ for FBC. These results suggest that as soon as the DM interaction is present, the model changes its universality class. To check this point more carefully, the computation of critical exponents is valuable and will

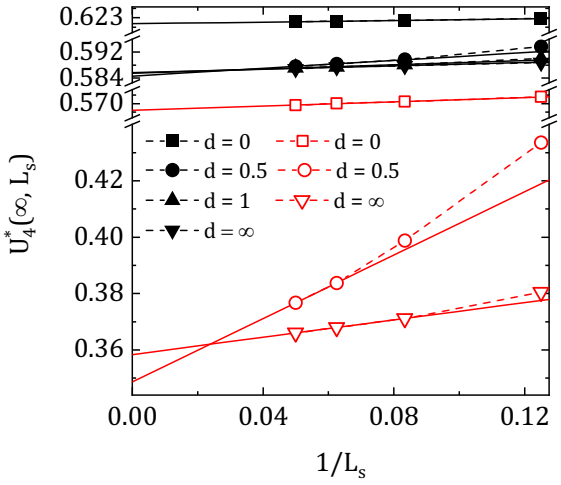

Figure 27 – Extrapolated values of the cumulants $U_4^*(\infty, L_s)$ from the fits of Figure 26, as a function of $1/L_s$, for different DM interaction d (here represented by different symbols) with SBC (full symbols) and FBC (open symbols). The numerical data in this graph can be seen in Table 6. The case $d = 1$ with only SBC has also been added in this figure. The cumulant axis has different scales for different values of d as well as for different boundary conditions. The full lines are linear fits, except for $d = 0.5$ FBC, which the straight line is defined by the two points which it passes through them. The dashed lines are just guides to the eyes and the error bars are smaller than the symbol sizes.

be considered in Subsection 3.3.3.

3.3.2 Critical temperature dependence on DM interaction

Shorter simulations were done just to locate the transition temperature for further values of d. These transitions were estimated using cumulant crossings between lattices $L = 32$ and $L = 24$ only, with SBC (FBC gives similar estimates). Although such estimates are, in fact, underestimated in comparison to estimates for the infinite system, the error in the values of T_c are relatively small when viewed in the whole temperature range under consideration. With this additional data, a good picture of the global phase diagram in the T-d plane could be obtained, as depicted in Figure 28, which has a similar layout to the phase diagram shown in Figure 10 for the model studied in the previous chapter.

The main figure shows the reduced temperature $T_c(d)/T_c^{DM}$ as a function of d. With this definition, the asymptotic behavior of $T_c(d)/T_c^{DM}$, in the $d = \infty$ limit (given by the dashed line), has a declivity of 45°. The top inset shows $T_c(d)$ as a function of d for comparison. In this case, the asymptotic behavior of the transition line is such that $\tan\psi_\infty = T_c^{DM}$.

The results in the previous chapter could show that the two-dimensional planar rotator model with DM interaction has an exact hyperbolic expression for the critical

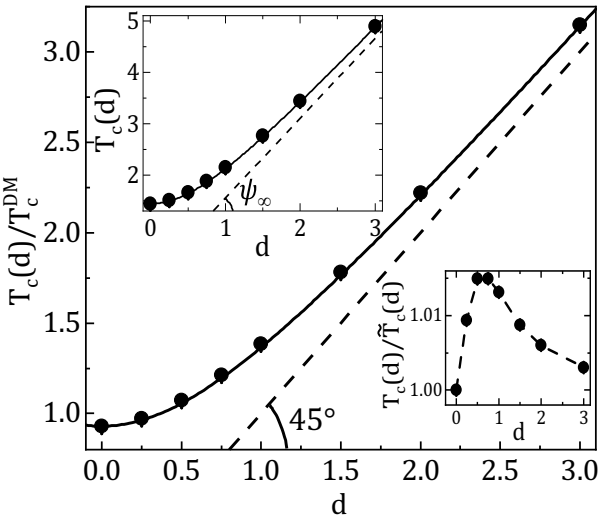

Figure 28 – Phase diagram in the temperature versus DM interaction plane. The circles are the present results and the full lines are fits to a hyperbolic function as described in the text. The dashed lines are the slopes of the transition lines for the limiting case $d = \infty$. The main graph shows the normalized transition temperature $T_c(d)/T_c^{DM}$, where the asymptote slope is 45°. The top inset gives $T_c(d)$, where the asymptote slope is ψ_∞. The bottom inset shows the ratio $T_c(d)/\widetilde{T}_c(d)$. The error bars are smaller than the symbol sizes.

temperature as a function of DM interaction, which depends only on the critical temperature for $d = 0$. To test whether the Heisenberg model with DM interaction could reproduce such behavior in its critical temperature dependence on d, a fit of the ratio $T_c(d)/T_c^{DM}$ was performed to a branch of a hyperbola defined as

$$\begin{aligned} \widetilde{T}_c(d) &= T_c^{DM}\sqrt{r^2 + d^2}, \\ r &= \frac{T_c(0)}{T_c^{DM}}, \end{aligned} \tag{3.23}$$

where $T_c(0)$ is the critical temperature of the Heisenberg model, and r is the only adjustable parameter. The full line in the upper inset in Figure 28 is given by setting $T_c(0) = 1.44293(5)$ and $T_c^{DM} = 1.55183(1)$ (these are the final estimates in Table 5 for $d = 0$ SBC and $d = \infty$ SBC, respectively), resulting in $r = 0.92982(3)$. The fit in the main graph, shown as a full line, gives almost the same result, namely $r = 0.92982(7)$. Naturally, the data do not follow a hyperbolic function, as can be seen in the bottom inset. Not like the deviations observed in the bottom inset of Figure 10, the present inset shows that the ratio $T_c(d)/\widetilde{T}_c(d)$ has a systematic deviation, with the largest deviation around $d \approx 0.625$ and asymptotically decreasing to unity as d tends to infinity. However, the fitted line can give good estimates of the critical temperature for any different values of the DM interaction.

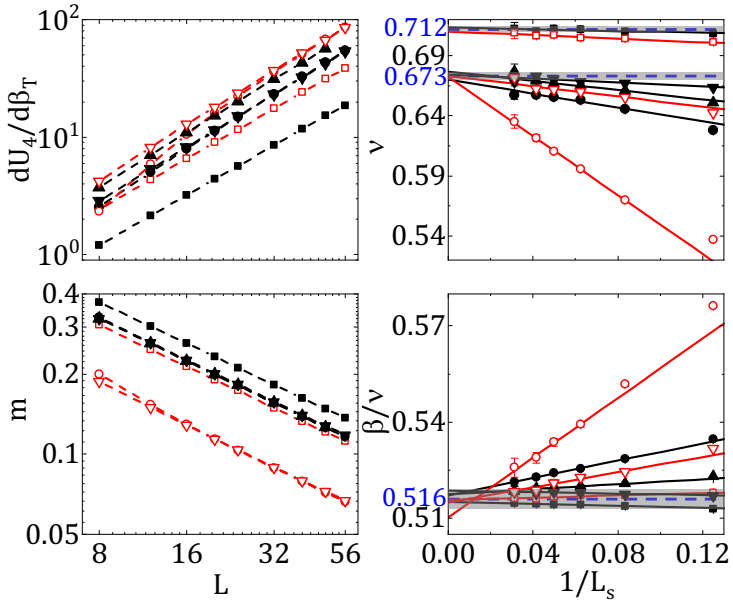

Figure 29 – Derivative of the order parameter fourth-order cumulant $dU_4(\beta_T; L)/d\beta_T$ (top left panel) and order parameter m (bottom left panel), both as function of the lattice size L and evaluated at $T = T_c$. In the left panels the axes scales are logarithmic and the dashed lines are just a guide to the eye. The linear fits, as described in the text, are shown for the critical exponent ν in the top right panel, and the ratio β/ν in the bottom right panel, as function of $1/L_s$ (L_s here means the smallest lattice size discarded in the fit), where full lines are additional linear fits. Horizontal dashed-lines in the two right panels indicate the mean values with the shaded area giving an idea of the error bars. The legends of Figure 27 also apply in this case.

3.3.3 Critical exponents

3.3.3.1 Critical exponent ν and β/ν ratio

The critical exponent ν and the ratio β/ν can be obtained taking advantage of the data from the MC simulations used to estimate T_c and U_4^*. Then, the derivative $dU_4(\beta_T; L)/d\beta_T$ and the order parameter m can be extrapolated at T_c by using Equations (3.10) and (3.17). The top left and bottom left panels in Figure 29 show, respectively, the derivative $dU_4(\beta_T; L)/d\beta_T$ and the order parameter m at T_c, both as a function of the lattice size L (the axes are in logarithmic scale). From the FSS relations given by Equations (3.13) and (3.14), the slopes of the linear fits are expected to furnish ν in the former case and β/ν in the latter case. However, although not completely apparent in Figure 29, in some cases, residual finite-size effects are still present.

To better estimate the critical exponents, several linear fits have been made by progressively discarding the smaller lattices. With L_s now being the smallest lattice size considered in the linear fit, a good estimate of the critical exponents could be obtained by

varying L_s from 8 to 32. The corresponding results, as a function of $1/L_s$, are depicted in the right panels of Figure 29, where in general, the finite-size effects are remarkably stronger for $d \neq 0$ and for FBC. These effects are even more pronounced for $d = 0.5$ with FBC. The full lines in the right panels of Figure 29 are additional linear fits to determine the final estimates of ν and β/ν, shown in Table 7.

Table 7 – Final estimates of ν and β/ν resulting from the straight line fits in the graphs on the right side of Figure 29. The last two rows show the averages of the estimates of ν and β/ν separated into $d = 0$ results and $d \neq 0$ results.

d	ν	β/ν
0 (SBC)	0.713(2)	0.5151(1)
0 (FBC)	0.710(1)	0.5158(4)
0.5 (SBC)	0.670(2)	0.5172(3)
0.5 (FBC)	0.6726(7)	0.510(4)
1 (SBC)	0.677(2)	0.5175(1)
∞ (SBC)	0.674(2)	0.5186(4)
∞ (FBC)	0.673(3)	0.515(1)
$d = 0$	0.712(2)	0.5155(4)
$d \neq 0$	0.673(3)	0.516(3)

As an example, focusing on the $d = 0$ case shown in the top right panel of Figure 29, the extrapolated value of the correlation length critical exponent is $\nu = 0.713(2)$ with SBC and $\nu = 0.710(1)$ with FBC. As expected, ν should be independent of the boundary conditions. These results can be averaged, leading to $\nu = 0.712(2)$ as a final estimate for $d = 0$ and highlighted in the graph by the upper horizontal dashed line. The shaded stripe gives some notion of the standard deviation of ν. Interestingly, all the extrapolations tend to the same result for $d \neq 0$, independent of the type of boundary conditions. The corresponding average of the estimates in Table 7 and represented by the horizontal dashed line in the top right panel in Figure 29, gives $\nu = 0.673(3)$. This means, indeed, that the DM interaction does change the universality class of the model, as was suggested by the computation of the fourth-order cumulant in the previous subsection.

Similarly to the procedure of obtaining ν, in the bottom right panel of Figure 29 are depicted the extrapolations obtained for the ratio β/ν. Although $d = 0.5$ with FBC still seems to demand even larger lattices with more MCS (which would take much more computational effort), the extrapolations converge to the same region for all of the cases. The estimates shown in Table 7 provides an estimate $\beta/\nu = 0.5155(4)$ for $d = 0$ and $\beta/\nu = 0.516(3)$ for $d \neq 0$, which suggest that besides having different exponents, the system satisfies the so called *weak universality class*, where the exponents are different but their ratios are the same [66, 67].

In order to further seek whether the weak universality class really holds for this

model, the ratio γ/ν and α/ν have also been computed by MC simulations with less CPU time.

3.3.3.2 γ/ν and α/ν ratios

The order parameter susceptibility χ and the specific heat C were obtained with less computational effort, as outlined by the second approach in subsection 3.2.3, at the cost of having less precise data. Only one MCSL, generating 10^5 data points, was performed at each temperature value in intervals having resolution $\Delta T = 0.001$ or $\Delta T = 0.0005$ close to the region of maximum values of the susceptibility and specific heat. For each lattice size L, the maximum values C_{peak} and χ_{peak} were estimated by firstly considering the largest value in C or in χ along the temperature interval, and then checking if other values would agree with the largest one within the error bars. When such values appeared, the final estimate of C_{peak} or χ_{peak} was the average of them including the largest value, otherwise, the final estimate was only the largest value with its error bar. During this procedure was also estimated the correspondent temperatures $T_{C_{peak}}$ and $T_{\chi_{peak}}$. In this way, for each lattice size L, not only χ_{peak} and C_{peak} were obtained, but also the corresponding temperatures where these peaks occur. MC simulations of lattice sizes $L = 64$ were also performed for $d = 0, 0.5$, and $d = \infty$ with SBC and FBC.

The FSS behavior of χ and C are expressed by Equations (3.15) and (3.16). The peak temperature T_{peak}, which can be either $T_{\chi_{\text{peak}}}$ or $T_{C_{\text{peak}}}$ has, for large enough systems, a FSS relation given by [6, 63]

$$T_{\text{peak}}(L) \approx T_c + b_{\text{peak}} L^{-1/\nu}, \tag{3.24}$$

where b_{peak} is a non-universal constant.

Figure 30 shows the peak temperature, T_{peak}, as a function of $L^{-1/\nu}$, obtained from the susceptibility and specific heat, for different values of d and boundary conditions. In this case, the ν exponents have been the mean values in Table 7, i.e. $\nu = 0.712$ for $d = 0$ and $\nu = 0.673$ for all values $d \neq 0$. In each data set, two linear fits were made, namely, one with all lattices and another neglecting the smallest lattice $L = 8$. When the linear fits are quite different, which are apparent only for some cases in Figure 30, the estimates come from fits neglecting the smallest lattice size. The corresponding results are displayed in Table 8. As one can see, the estimates of the critical temperature from the susceptibility and specific heat for all values of d are in agreement with each other, and also in agreement with the estimates of T_c obtained from the cumulant crossings.

Figure 31 shows the logarithm of the order parameter susceptibility peak χ_{peak} as a function of the logarithm of the lattice size L for different values of d. The slope of each data set furnishes, according to Equation (3.15), the ratio γ/ν. In this case, due to the shorter MC runs, the same analysis as the one for β/ν is not useful. Nevertheless, for all values of d, the slopes from the fits neglecting the smaller lattice size $L = 8$ are close

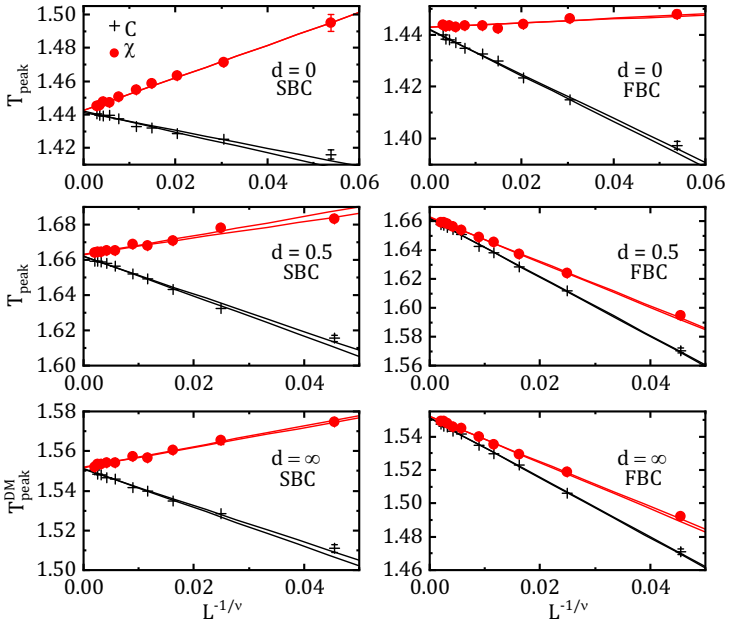

Figure 30 – Peak temperatures T_{peak} and $T_{\text{peak}}^{\text{DM}}$ of the susceptibility (circles) and specific heat (crosses) as a function of $L^{-1/\nu}$ for different values of d and respective boundary conditions, SBC and FBC. The exponents $\nu = 0.712(2)$ for $d = 0$ and $\nu = 0.673(3)$ for $d \neq 0$ are those obtained in this work and displayed in Table 7. For each data set there are two lines coming from linear fits, one considering all lattices and another neglecting the smallest lattice size. The error bars are smaller than the symbol sizes.

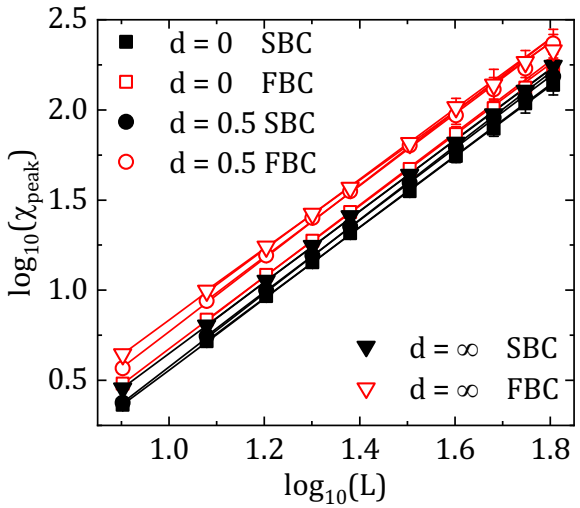

Figure 31 – Logarithm of the order parameter susceptibility peak χ_{peak} as a function of the logarithm of the lattice size L for different values of d with the boundary conditions specified in the legend. There are two lines corresponding to linear fits, one with all data and another neglecting the smallest lattice size. The error bars are smaller than the symbol sizes when they are not visible.

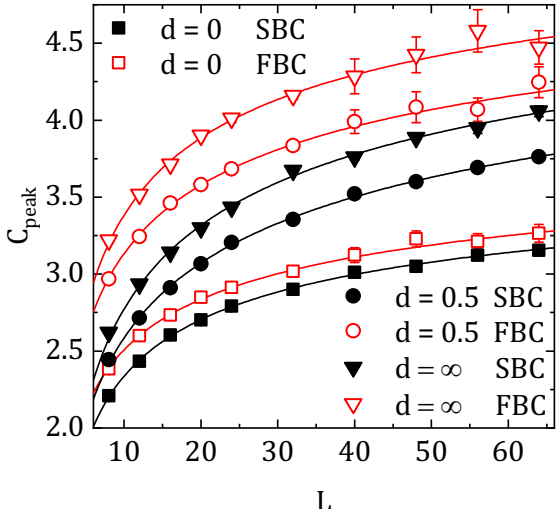

Figure 32 – Specific heat peak C_{peak}, as a function of the lattice size L, for different values of d with the boundary conditions specified in the legend. Full lines are non-linear fits according to Equation (3.16) and considering all data for each value of d. The error bars are smaller than the symbol sizes when they are not visible.

together, and the final estimates for γ/ν are listed in Table 8. The corresponding averages for the $d = 0$ and $d \neq 0$ results are also shown in the bottom of the table.

The specific heat peaks as a function of L and for the same values of d are shown in Figure 32. α is clearly negative, since C goes to a constant as $L \to \infty$. The full lines in Figure 32 are fits using Equation (3.16) and considering all data points. The corresponding values for d different from zero have been averaged and are displayed in Table 8. For comparison, the ratios α/ν for $d = 0$ with SBC and FBC have also been averaged and given in this same table. The strong presence of the infinite system background in the specific heat can be seen by the constant C_∞, which has ranged from 4.2(2) to 7(1), according to the fit results.

3.3.4 Structure factor

The structure factor, $\mathcal{S}(\boldsymbol{q})$, was measured for the same values of d as before and using the second approach of performing the MC simulations described in the previous subsections. The simulated lattice sizes were $L = 8, 12, 16, 20$ and 24, for both SBC and FBC. For this purpose, the final data consist of files containing all pair-correlation functions $\Gamma(\boldsymbol{r}_{jk})$ in Equation (3.20), in which they are estimated with their corresponding uncertainties. Thus, $S(\boldsymbol{q})$ can be calculated as a function of any arbitrary wave vector $\boldsymbol{q}$ through the Equation (3.20) and the pair-correlation functions data. Here, $\boldsymbol{q}$ is measured in radians per lattice spacing, with the lattice spacing being defined as unity. The uncertainty in the structure factor was estimated from the error propagation coming from $\Gamma(\boldsymbol{r}_{jk})$.

Table 8 – Estimates for the critical temperatures of the infinite system with different d values and boundary condition by taking the temperatures where the peaks in the specific heat and order parameter susceptibility occur, respectively providing $T_c^{C_{\text{peak}}}$ and $T_c^{\chi_{\text{peak}}}$. In turn, the peaks in the specific heat and order parameter susceptibility lead to the estimates of the ratios γ/ν and α/ν.

d	$T_c^{C_{\text{peak}}}$	$T_c^{\chi_{\text{peak}}}$	γ/ν	α/ν
0 (SBC)	1.4419(6)	1.4424(4)	1.963(6)	-0.33(7)
0 (FBC)	1.4420(4)	1.4428(4)	1.969(5)	-0.25(9)
0.5 (SBC)	1.6621(4)	1.6629(3)	1.997(8)	-0.18(5)
0.5 (FBC)	1.6629(2)	1.6630(2)	1.984(22)	-0.23(9)
∞ (SBC)	1.5512(5)	1.5517(4)	1.968(15)	-0.24(9)
∞ (FBC)	1.5513(3)	1.5521(3)	1.951(12)	-0.29(11)
$d = 0$			1.966(4)	-0.29(6)
$d \neq 0$			1.975(20)	-0.24(5)

As an example, the static structure factor $\mathcal{S}(\boldsymbol{q})$ is shown in Figure 33 for wave vectors in the q_x-q_y plane, for a lattice with size $L = 20$ at $T = T_c$ for various values of d. The same pattern is obtained when the wave vector lies either in the q_x-q_z or q_y-q_z planes. The intensity of the peaks, as well as their width, is indicated by the gradient scale on the right of each graph. It should be noted that the peaks in $\mathcal{S}(\boldsymbol{q})$ occur at $q_x = q_y = \pm\phi$, where ϕ is the pitch angle. As one can see from the gradient intensities in the figure, the height of the peaks gradually decrease, with their widths becoming wider as d increases from $d = 0$, and ending up with the most spreading values close to unity for $d = \infty$.

The dependence of the maximum value of $\mathcal{S}(\phi, \phi, 0)$ on the system size L and then the possibility of any FSS were checked. The graph on the left side in Figure 34 shows, for the same d values considered in Figure 33, a plot of the peak of $\mathcal{S}(\phi, \phi, 0)$, as a function of $L = 8, 12, 16, 20$ and 24, where both axes are logarithmic. Some results from simulations with FBC performed at $T = T_c$ were also included in this analysis. The model without DM interaction ($d = 0$ and $\phi = 0$) exhibits the usual long-range magnetic ordering along the planes in the lattice, as expected and clearly seen in the behavior of $\mathcal{S}(0, 0, 0)$, which increases as L increases and tends to infinity in the thermodynamic limit. However, for $d \neq 0$, the peaks $\mathcal{S}(\phi, \phi, 0)$ do not show any regular increase as L increases. Instead, the points tend to saturate or fluctuate around a horizontal line. This means that looking at x-y, x-z and y-z planes in the lattice, none long-range magnetic ordering seems to be observed.

On the other hand, the behavior of $\mathcal{S}(\boldsymbol{q})$ when $\boldsymbol{q} = \pm(\phi, \phi, \phi)$ and $d \neq 0$ is quite different. This particular wave vector is parallel to the diagonal direction of the lattice or, in terms of crystallographic definitions, the [111] direction in a simple cubic lattice. The corresponding peaks of $\mathcal{S}(\boldsymbol{q})$ at $T = T_c$, as a function of L, in logarithmic scales, are shown

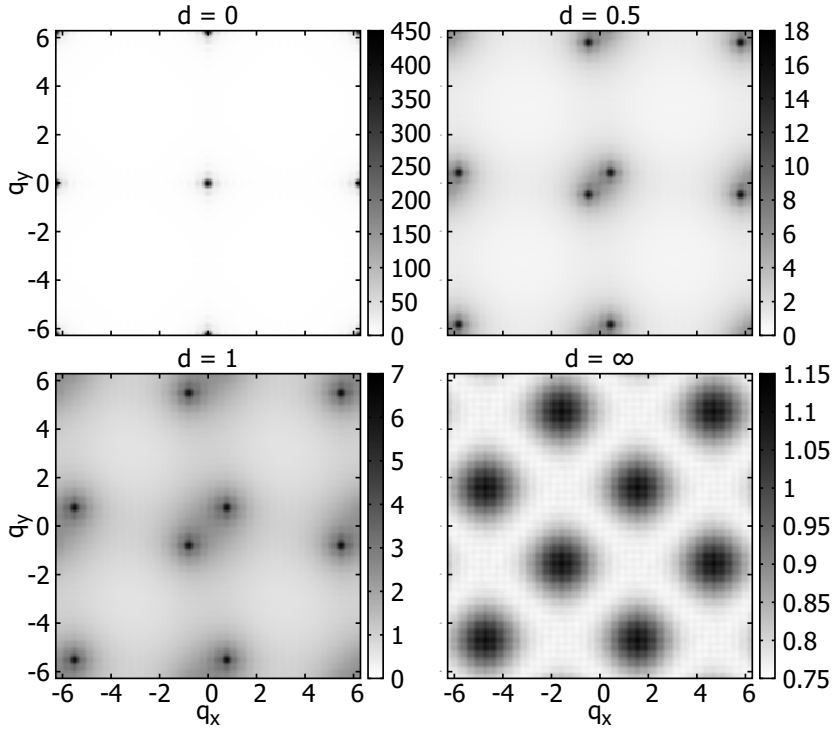

Figure 33 – Structure factor $\mathcal{S}(\boldsymbol{q})$ for the wave vector in the q_x-q_y plane with $q_z = 0$ and $T = T_c$ for different values of d. The lattice size is $L = 20$ and SBC was used in the MC simulations. The intensity of $\mathcal{S}(\boldsymbol{q})$ is given by the gradient scale on the right side of each figure.

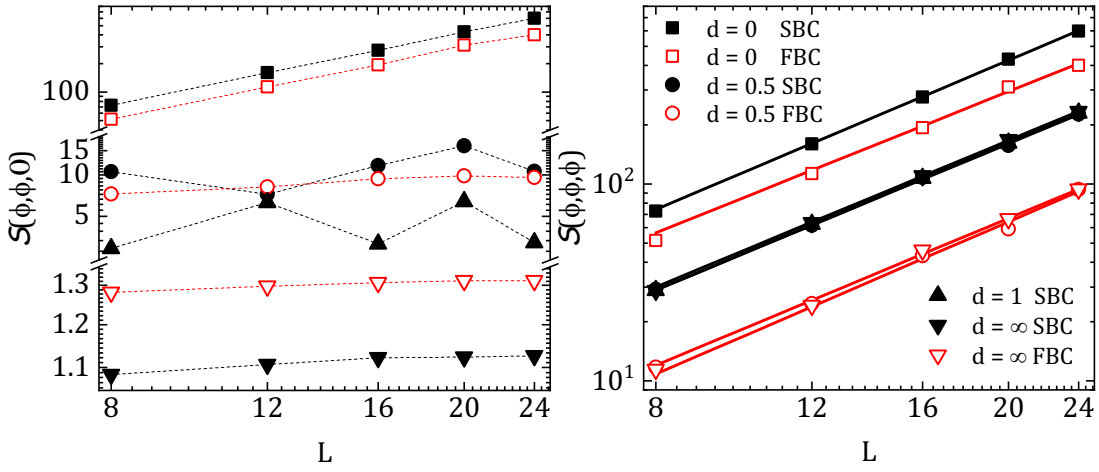

Figure 34 – Peak values of the static structure factor $\mathcal{S}(\boldsymbol{q})$, for wave vectors $\boldsymbol{q} = \pm(\phi, \phi, 0)$ (left panel) and $\boldsymbol{q} = \pm(\phi, \phi, \phi)$ (right panel), as a function of the lattice size L. The results are at $T = T_c$ for each d indicated in the legends (valid also for the top panel). Both axes are logarithmic. Dashed lines are only guides to the eye while solid lines are linear fits to the data. The error bars are smaller than the symbol sizes.

in the right panel of Figure 34. The two curves for $d = 0$ have not changed their behavior in relation to those in the graph on the left. However, for all of the remaining curves with $d \neq 0$, $\mathcal{S}(\phi, \phi, \phi)$ follows now the same trend as for $d = 0$, increasing with L and diverging to infinity in the thermodynamic limit. In other words, the magnetic long-range ordering for $d \neq 0$ is observed when the wave vector $\boldsymbol{q}$ is oriented along the diagonal directions with specific values that depend on d through the pitch angle ϕ. This result agrees with a theoretical finding for this model [29], which shows that the magnetization changes in a spiral way with rotations around the z-axis with a wave vector $\boldsymbol{q} = \pm(\phi, \phi, \phi)$.

Remarkably, all the curves in the right graph of Figure 34 follow a power law and are almost parallel to each other. In fact, by the static structure factor definition in Equation (3.20), one can verify that $\mathcal{S}(\phi, \phi, \phi) \approx \mathcal{S}_0 L^{\gamma/\nu}$ when $T = T_c$. Although the lattice sizes in this case are not as large as those used in the susceptibility and specific peaks analysis, linear fits to all data in the right graph of Figure 34 were also performed. The fit results were averaged, giving $\gamma/\nu = 1.9(1)$, in good agreement with the previous values from the order parameter susceptibility in Table 8 (despite the larger error due to the less statistics in this case).

The oscillations present in $\mathcal{S}(\phi, \phi, 0)$ as a function of L, depicted in the top panel of Figure 34, deserve more attention. Thus, in order to obtain extra insight about the $\mathcal{S}(\boldsymbol{q})$ behavior as a function of $\boldsymbol{q}$, ϕ and L, a complex-value magnetization $\widetilde{\mathcal{M}}(\boldsymbol{q})$ was defined, given by

$$\widetilde{\mathcal{M}}(\boldsymbol{q}) = \frac{1}{N} \left\| \sum_{j=1}^{N} \boldsymbol{S}_j e^{-i\boldsymbol{q}\cdot\boldsymbol{r}_j} \right\|, \tag{3.25}$$

which may assume complex values (the two double-vertical bars on the right hand side in the above equation represent the vector modulus). N is the total number of spins in the lattice. Then, the structure factor is, apart from some proportionality constant, written as

$$\mathcal{S}(\boldsymbol{q}) = N \left| \widetilde{\mathcal{M}}(\boldsymbol{q}) \right|^2, \tag{3.26}$$

where the vertical bars refer to the modulus of the complex $\widetilde{\mathcal{M}}(\boldsymbol{q})$. Considering then the ground-state spin configuration, the structure factor for a simple cubic lattice with $N = L^3$ sites can be written in analytical form

$$\mathcal{S}(\boldsymbol{q}) = \frac{1}{2L^3} \prod_{j=1}^{3} \left(\left\{ \frac{\sin\left[(\phi + q_j)L/2\right]}{\sin\left[(\phi + q_j)/2\right]} \right\}^2 + \left\{ \frac{\sin\left[(\phi - q_j)L/2\right]}{\sin\left[(\phi - q_j)/2\right]} \right\}^2 \right), \tag{3.27}$$

where the index $j = 1, 2, 3$ labels the x, y and z wave-vector components, respectively.

Figure 35 shows similar plots to those ones in Figure 33, but with the data generated from Equation (3.27), with $q_z = 0$ and $L = 20$. For the case $d \to \infty$ shown in the bottom right panel, instead of using the "$d = \infty$" notation, the "$d \to \infty$" notation has been preferred due to $\mathcal{S}(q_x, q_y, 0)$ becomes identically equal to zero when $\phi = \pi/2$ and $L = 20$ in Equation (3.27). In this way, to depict $\mathcal{S}(q_x, q_y, 0)$ in the $d \to \infty$ limit, the corresponding plot was set with $d = 100$.

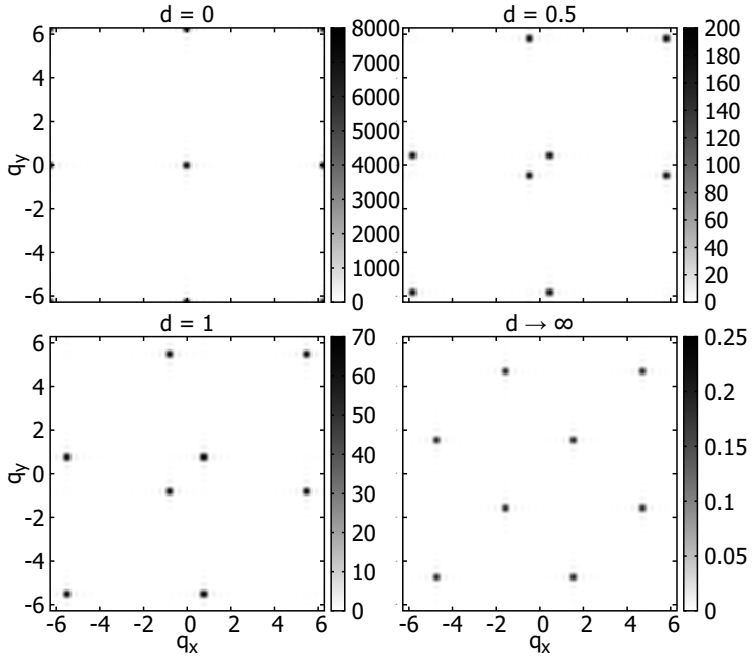

Figure 35 – Structure factor $\mathcal{S}(\boldsymbol{q})$ analytically calculated in the plane q_x-q_y with $q_z = 0$ by using Equation (3.27), considering the ground state spin configuration. The lattice size is $L = 20$. The intensity of $\mathcal{S}(\boldsymbol{q})$ is given by the gradient scale on the right side of each figure.

In the case that $q_x = q_y = \pm\phi$ and $q_z = 0$, Equation (3.27) simplifies into

$$\mathcal{S}(\phi, \phi, 0) = \frac{1}{2L^3}\left\{\left[\frac{\sin(L\phi)}{\sin\phi}\right]^4 + L^4\right\}\left[\frac{\sin(L\phi/2)}{\sin(\phi/2)}\right]^2. \tag{3.28}$$

The left panel of Figure 36 is a plot of the above structure factor for $d = 0.5, 1$ and ∞ as a function of L, both quantities on logarithmic scale. $\mathcal{S}(\phi, \phi, 0)$ was rescaled using the maximum values from the MC results in the left graph of Figure 34. The similarity of the data at $T = 0$ with those obtained at $T = T_c$ depicted in the left panel of Figure 36 is patent. Nevertheless, here it becomes easier to understand the oscillations as L changes, because the structure factor is zero whenever $\sin(L\phi/2) = 0$. In fact, using exactly $L = 8, 16$ and 24 for $d = 1$ and $L = 8, 12, 16, 20$ and 24 for $d = \infty$ in the log-log plot of $\mathcal{S}(\phi, \phi, 0)$ is not possible, just due to these zeros of Equation (3.28). They can be clearly seen in the right panel of Figure 36, where the values of L are discrete and vary in unity steps. One could still infer that there is a FSS behavior for lattices that are commensurate with the pitch angle and a different FSS for incommensurate lattices. This is clearly seen for $d = 1$ and $d = \infty$, the latter being valid for all data because all lattice sizes are commensurate with the pitch angle. However, for $d = 0.5$, none of the L values turn out to be commensurate and the data do not follow any special scaling.

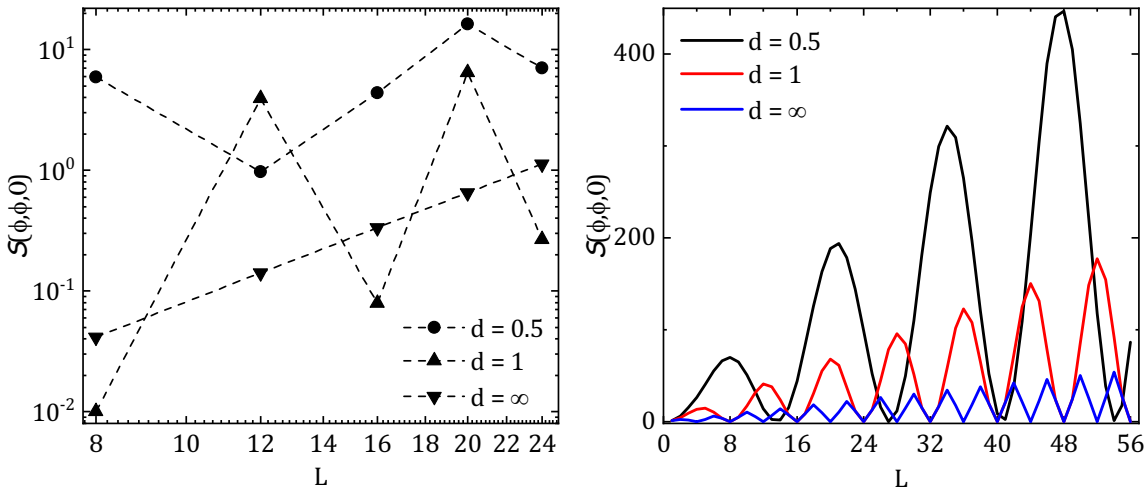

Figure 36 – Left panel shows a log-log plot of the peak values of the static structure factor $\mathcal{S}(\boldsymbol{q})$, obtained by Equation (3.28), with wave vector $\boldsymbol{q} = \pm(\phi, \phi, 0)$, as a function of the lattice size L. The results are at $T = 0$ for each d shown in the legend. Dashed lines are only guides to the eyes. Right panel shows $\mathcal{S}(\phi, \phi, 0)$ as a function of discrete values of L, where they vary in unity steps. Solid lines are only a guide to the eyes.

Finally, for the wave vector $\boldsymbol{q} = \pm(\phi, \phi, \phi)$, Equation (3.27) results in

$$\mathcal{S}(\phi, \phi, \phi) = \frac{1}{2L^3}\left\{\left[\frac{\sin(L\phi)}{\sin\phi}\right]^6 + L^6\right\}, \tag{3.29}$$

which does not have any zeros for $L > 0$ and increases as L^3.

3.3.5 Boundary condition analysis

In Subsection 3.2.2 was presented the definitions of the SBC and FBC, where the difference between them is that, during the MC simulation, the former has a same fixed phase shift angle for each of the x-, y- and z-directions of the lattice, whereas the latter has three independent variable phase shift angles defined for the x-, y- and z-directions. These phase shift angles have been written as Δ_x, Δ_y and Δ_z. For SBC, they are calculated by Equation (3.5) and for FBC are generated every MCS following the prescription in Equation (3.8).

Figure 37 shows the phase shift angle distribution $P(\Delta_i)$ as a function of Δ_i for $d = 0.5$ in the MC simulations with FBC for each specified direction, labeled by $i = x, y, z$. In this example, the lattice size is $L = 8$ and the temperature is $T = 1.6$, which is close to the critical temperature for $d = 0.5$. The distributions are practically identical, as expected, since the lattice has cubic geometry. Besides that, the general behavior of these distributions was previously analyzed in Subsection 2.3.5, where the Gaussian shaping of these curves could be seen. The mean values below the curve, i.e. $\langle\Delta_x\rangle$, $\langle\Delta_y\rangle$ and $\langle\Delta_z\rangle$,

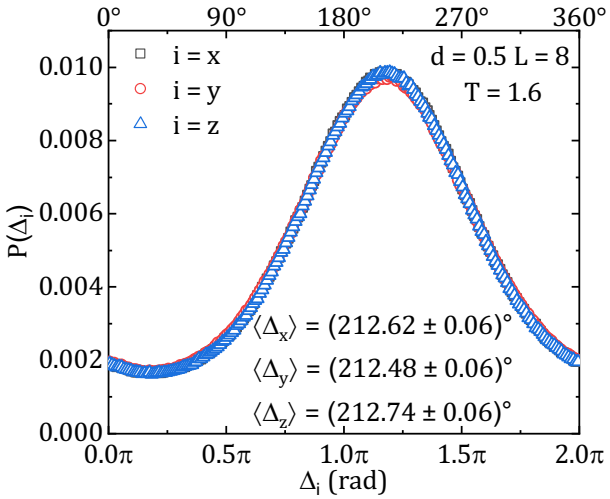

Figure 37 – Phase shift angle distribution $P(\Delta_i)$ as a function of Δ_i for $d = 0.5$ at $T = 1.6$, where $i = x, y, z$ specifies the x-, y- and z-directions in the lattice. The three curves (there is an overlap of them) were independently calculated for each of these directions according to the FBC prescription given by Equation (3.8). The lattice size is $L = 8$. The mean value $\langle\Delta_i\rangle$ for each direction is indicated below the curves. They come from Gaussian fits in the data, modeled with Equation (2.41).

come from Gaussian fits based on Equation (2.41)[8]. For a comparison, the phase shift angles used in the SBC resulting from Equation (3.5) are $\Delta_x = \Delta_y = \Delta_z = 212.52...°$, showing again that the predicted incommensurability between the lattice and the ground-state spin structure persists in the temperature range from $T = 0$ up to $T \lesssim T_c$.

The differences that have been observed during the FSS analysis with respect to the SBC and FBC, may be mainly due to the probability distributions of the energy and order parameter, which are produced from MC simulations using each of these boundary conditions. As an example, Figure 38 shows the energy per site and order parameter probability distribution function for the lattice size $L = 48$ in the three regimes of the DM interaction using both SBC and FBC. The energy unit for the $d = 0$ and $d = 0.5$ regimes is J, and for $d = \infty$ regime (a pure "DM model") it may be either D or $J\sqrt{1 + d^2}$ with $d \to \infty$. For each value of d, the probability distributions were obtained using histograms at a temperature that comes from the average of the critical temperature estimates with SBC and FBC. More precisely, this temperature has been defined as the mean critical temperature $\bar{T}_c(d) = [T_c(d)_{SBC} + T_c(d)_{FBC}]/2$. The amount of data obtained from the MC simulations was large enough to ensure that energy and order parameter distributions maintain their shapes and are free from any noise at their tails, as discussed in Appendix B. Thus, the smooth behavior of the curves shows that the temperature range is still within the region of validity.

[8] Here, the probability $P(\Delta)$ has not been divided by the maximum probability $P(\langle\Delta\rangle)$ at the mean value $\langle\Delta\rangle$.

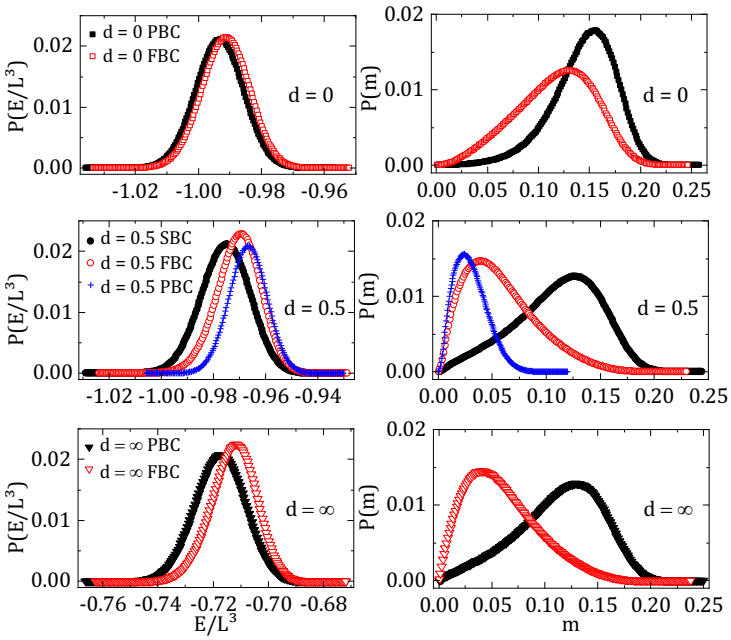

Figure 38 – Probability distributions of the energy per site $P\,(E/L^3)$ (left panels) and order parameter $P\,(m)$ (right panels) for values of d in the three chosen regimes and both SBC and FBC. The lattice size is $L = 48$ and the temperature is close to the critical temperature for each DM interaction. The middle panels for $d = 0.5$ also show the probability distribution with periodic boundary conditions (PBC). The legends on the left panels also apply to the right panels.

The shapes of the distributions are clearly dependent upon the type of the chosen boundary conditions. Both $d = 0$ and $d = \infty$ are commensurate with the lattice size $L = 48$, and the use of either SBC or usual periodic boundary condition (PBC) give the same result. The situation is different for $d = 0.5$, because there is an unavoidable incommensurability with the lattice, as described in Subsection 2.3.5. The middle panels of Figure 38 also show the corresponding probability distributions using PBC. However, results with PBC for incommensurate lattices do not produce coherent values with the expected FSS behavior, as previously shown in Figure 18. This can be clearly seen for $d = 0.5$ in Figure 38, where $P(E/L^3)$ for PBC is remarkably narrower with its σ^2 smaller than the other boundary conditions, and $P(m)$ has much smaller width and wings, resulting in much different susceptibilities and fourth-order cumulants. There are also remarkable differences between the SBC and FBC energy and order parameter distributions, which are even more evident for $d = 0.5$ and $d = \infty$ than for $d = 0$. As a result, these differences are, for example, reflected in the order parameter fourth-order cumulants (Figure 26), order parameter susceptibilities (Figure 31) and specific heat (Figure 32), among other related quantities. Although in the thermodynamic limit the critical temperature and critical exponents estimates are expected to be the same, the universal value of the order parameter fourth-order cumulants have not been the same, as shown along this work.

There might be some fundamental difference, at least in the order parameter distributions, associated with the defined boundary condition.

3.4 Conclusion

Table 9 – Final estimates of the critical temperature T_c, the value of the cumulant U_4^* at T_c, the critical exponent ν and the ratios β/ν, γ/ν and α/ν, for several values of d and both SBC and FBC. $T_c^{C_{\text{peak}}}$ and $T_c^{\chi_{\text{peak}}}$ are also critical temperature estimates obtained from finite-size scaling (FSS) analyses. The universal values are averages obtained from the top 7 row data and also include the ratio U_4^*/ν_{SBC} for SBC. Some results from the literature for the Heisenberg and XY models are also displayed for comparison.

d	T_c	U_4^*	ν	β/ν	γ/ν	α/ν	$T_c^{C_{\text{peak}}}$	$T_c^{\chi_{\text{peak}}}$
0 (SBC)	1.44293(5)	0.6208(1)	0.713(2)	0.5152(1)	1.963(6)	-0.33(7)	1.4419(6)	1.4424(4)
0 (FBC)	1.44296(2)	0.5679(2)	0.710(1)	0.5158(4)	1.969(5)	-0.25(9)	1.4420(4)	1.4428(4)
0.5 (SBC)	1.66281(1)	0.58434(9)	0.670(2)	0.5172(3)	1.997(8)	-0.18(5)	1.6621(4)	1.6629(3)
0.5 (FBC)	1.66272(3)	0.3488(2)	0.6726(7)	0.510(4)	1.984(22)	-0.23(9)	1.6629(2)	1.6630(2)
1 (SBC)	2.14692(5)	0.5854(1)	0.677(2)	0.5175(1)				
∞ (SBC)	1.55183(1)	0.5856(4)	0.674(2)	0.5186(4)	1.968(15)	-0.24(9)	1.5512(5)	1.5517(4)
∞ (FBC)	1.55181(2)	0.35836(4)	0.673(3)	0.515(1)	1.951(12)	-0.29(11)	1.5513(3)	1.5521(3)

Heisenberg model with DM interaction (this work's results)

d	U_4^* (SBC)	U_4^* (FBC)	ν	β/ν	γ/ν	α/ν	U_4^*/ν_{SBC}	Reference
0	0.6208(1)	0.5679(2)	0.712(2)	0.5155(4)	1.966(4)	-0.29(6)	0.869(4)	
$\neq 0$	0.5851(7)	0.3536(69)	0.673(3)	0.516(3)	1.975(20)	-0.24(5)	0.872(2)	
Heisenberg model								
0	0.6202(1)		0.7112(5)	0.5187(6)	1.963(2)	-0.188(2)	0.8727(6)	[68]
	0.6217(8)[a]		0.712(4)	0.515(5)	1.972(7)	-0.192(16)	0.873(5)	[69]
XY model								
	0.5859(8)		0.669(6)	0.5179(24)	1.965(5)		0.876(8)	[70]
	0.5856(1)		0.6717(1)	0.5190(2)	1.9619(4)	-0.0225(5)	0.8718(2)	[71]

[a] from Reference [63]

The main results obtained along of the present Monte Carlo study of the Heisenberg model with DM interaction are summarized in Table 9. The first comparison is for the model with $d = 0$, where there are ample results in the literature for the isotropic Heisenberg model from different techniques, including experimental measurements of the critical exponents. The critical temperature, in this case $T_c = 1.44295(3)$, is in excellent agreement with previous MC simulations, e.g. $T_c = 1.442987(1)$ [69] and $T_c = 1.44293(6)$ [72].

The limiting case in which $d = \infty$, where the FM interactions are completely removed from the model and only DM interactions are actually left (a "DM model"), has been studied as well. The DM model undergoes a second-order phase transition, like the pure isotropic Heisenberg model, with critical temperature $T_c = 1.55183(1)$ (considering

the SBC result for instance). Below T_c, the spin configurations are in the spiral phase, and they change into the paramagnetic phase above T_c. Alternatively, the limiting case $d = \infty$ provides the variation rate T_c/d in the d tending to infinity limit, which is numerically equal to the previous critical temperature. Using this result together with the critical temperature estimates for other values of d, the global phase diagram in the T-d plane has been obtained. The T_c dependence on d follows a quasi-hyperbolic dependence. This means that $T_c(d)$ can be modeled by using a simple hyperbola equation. Although it is not an exact equation to describe $T_c(d)$ for this model, a quite good estimate can be inferred of the critical temperature for different values of the DM interaction d without the need of any further simulation.

Unlike the critical temperature and critical exponents, the fourth-order cumulant of the order parameter U_4^* depends upon the boundary conditions. From an analysis of the universal quantities given in Table 9, the critical exponents along the transition line for $d > 0$ are apparently different from the isotropic Heisenberg model. However, as the ratio of the critical exponents and the cumulants are the same, to within the error bars, it is evident that *weak universality* holds for the Heisenberg model with DM interaction. Moreover, from a comparison of the exponents for $d \neq 0$ and those in the literature for the XY model, the Heisenberg model with DM interaction has shown to be in the same weak universality class as the XY model [26, 27, 29]. Since the spin vectors tend to be partially aligned with planes perpendicular to the DM vector and the z-component of the magnetization fluctuating around zero as the temperature increases up to T_c, the XY model characteristic in the studied model is a coherent result.

The structure factor calculations have indicated that there is no presence of magnetic long-range order in the x-y, x-z and y-z planes for $d \neq 0$, like it occurs for the three-dimensional ferromagnetic Heisenberg model. Instead, for $d \neq 0$, magnetic long range order has been noticed when one observes the spin vectors along directions parallel to the diagonal of the lattice (the [111] direction in a simple cubic lattice). Some oscillations seen in the structure factor peaks as function of the lattice size for $d \neq 0$, when it is calculated in the previous mentioned planes, have appeared due to the effect of spin modulation caused by DM interaction in the finite lattices, as demonstrated from analytic results.

All results presented in Table 9 have also shown the possibility of keeping fixed phase shift angles in the angular differences through the boundary of the lattices as an alternative to the fluctuating boundary condition (FBC). In this case, this new boundary condition has been named shifted boundary condition (SBC). As long as the modulation of the spins in the ground state configuration is known, the phase shift angles can be accordingly calculated before the MC simulation starts. However, the probability distributions of the energy and order parameter from MC simulations with SBC and FBC will be remarkably different when they are compared to each other. Ultimately, the universal value of the fourth-order cumulant will be different between results from SBC and FBC, as pointed

out before.

Finally, it must be stressed that the careful considerations about the boundary condition used in the MC simulations allowed achieving the estimates for the critical quantities shown in Table 9. Additional numerical comparison to other MC simulations, as well as different approximation methods, can be found in References [73] and [74].

4 General conclusion

Through extensive Monte Carlo (MC) simulations and finite-size scaling (FSS) analyses, two classical ferromagnetic (FM) models with Dzyaloshinskii-Moriya (DM) interaction have been studied in this work: the two-dimensional planar rotator model on a square lattice and the three-dimensional Heisenberg model in a simple cubic lattice (summing up a total CPU time equivalent to around 113 years of single-core runnings). The incommensurability due to the presence of DM interactions in these models between spin structure and discrete finite lattices has been circumvented by using fluctuating boundary condition (FBC), and also a new type of boundary condition named shifted boundary condition (SBC). Then, coherent energy and order parameter data could be appropriately obtained from the MC simulations. The use of single histogram techniques have provided several thermodynamic functions being calculated at convenient temperature intervals, allowing to realize a finer analysis on these functions. As a result, FSS approach at the criticality of the models has led to good estimates of the involved thermodynamic quantities and to quite conclusive results about the universality of the transition.

For the two-dimensional planar rotator model, it could be seen that the presence of the DM interaction makes it equivalent to the pure planar rotator model with a rescaled exchange term, which depends upon DM interaction intensity. The modulation of the spin orientations caused by the DM interaction can accordingly be undone to recover the typical spin arrangement of the pure planar rotator model. Thus, the critical behavior of the model is dictated by the Berezinskii-Kosterlitz-Thouless (BKT) transition. As a result, the topological structure of vortices seen in the pure planar rotator model are also present in both the configuration with the undone modulation of the spins and in the actual spiral configuration, i.e. the configuration affected by the competition between the FM and DM interactions.

On the other hand, the three-dimensional Heisenberg model with DM interaction undergoes a second-order phase transition like the pure isotropic Heisenberg model. The spin configurations change from spiral phase into paramagnetic phase when the critical temperature is overcome. Structure factor calculations in a simple cubic lattice at the transition have shown that the magnetic long-range order of the spin vectors occurs along directions parallel to the diagonal ([111]) of the lattice. However, the universality class of the isotropic Heisenberg model has no longer held for the model with DM interaction. In fact, the Heisenberg model has presented what is called *weak universality* when DM interaction takes place. Moreover, it could be concluded that the Heisenberg model with DM interaction is in the same weak universality class as the XY model.

The present study has not addressed the effects of an external magnetic field applied in any of the systems. Such study is left for a future work. It would be very

interesting because of the possibility of a rich phase diagram displaying spiral, conical, solitons, skyrmions, induced ferromagnetic and paramagnetic phases, according to the values of temperature and magnetic field. Extra interaction terms could also be added to the Hamiltonian to make the model more realistic. For instance, interaction terms coming from crystal anisotropies which indeed occur in real magnetic materials. Even the inclusion of more than one DM interaction in the model is a plausible possibility.

Bibliography

[1] Heisenberg, W.: *Zur Theorie des Ferromagnetismus*, pages 580–597. Springer Berlin Heidelberg, Berlin, Heidelberg, 1985. https://doi.org/10.1007/978-3-642-61659-4_35. Cited on page 10.

[2] Nolting, Wolfgang and A. Ramakanth: *Quantum Theory of Magnetism*. 2009. https://api.semanticscholar.org/CorpusID:117078782. Cited on page 10.

[3] Mohn, Peter: *Magnetism in the solid state: an introduction*, volume 134. Springer Science & Business Media, 2002. https://doi.org/10.1007/3-540-30981-0. Cited on page 10.

[4] Coey, J. M. D.: *Magnetism and Magnetic Materials*. Cambridge University Press, 2010. https://doi.org/10.1017/CBO9780511845000. Cited 2 times on page 10 e 13.

[5] Sachdev, Subir: *Quantum Phase Transitions*. Cambridge University Press, 2nd edition, 2011. https://doi.org/10.1017/CBO9780511973765. Cited on page 10.

[6] Landau, David P. and Kurt Binder: *A Guide to Monte Carlo Simulations in Statistical Physics*. Cambridge University Press, 4th edition, 2014. https://doi.org/10.1017/CBO9781139696463. Cited 11 times on page 10, 13, 22, 23, 47, 52, 53, 55, 56, 67 e 92.

[7] Brush, Stephen G.: *History of the Lenz-Ising Model*. Reviews of Modern Physics, 39:883–893, 1967. https://link.aps.org/doi/10.1103/RevModPhys.39.883. Cited on page 11.

[8] Berezinsky, V. L.: *Destruction of long range order in one-dimensional and two-dimensional systems having a continuous symmetry group. I. Classical systems*. Soviet Physics—JETP, 32:493–500, 1971. Cited 2 times on page 11 e 16.

[9] Kosterlitz, J. M. and D. J. Thouless: *Ordering, metastability and phase transitions in two-dimensional systems*. Journal of Physics C: Solid State Physics, 6(7):1181, 1973. https://dx.doi.org/10.1088/0022-3719/6/7/010. Cited 4 times on page 11, 16, 38 e 39.

[10] Kosterlitz, J. M.: *The critical properties of the two-dimensional xy model*. Journal of Physics C: Solid State Physics, 7(6):1046, 1974. https://dx.doi.org/10.1088/0022-3719/7/6/005. Cited 4 times on page 11, 16, 23 e 39.

[11] Holz, Arno: *High-Temperature Study of Planar Rotator- and XY-Models for Dimensions $D \leq 2$*, pages 277–294. Springer Netherlands, Dordrecht, 1981. https://doi.org/10.1007/978-94-009-8368-7_16. Cited on page 11.

[12] Erickson, R. A.: *Neutron Diffraction Studies of Antiferromagnetism in Manganous Fluoride and Some Isomorphous Compounds*. Physical Review Journals Archive, 90:779–785, 1953. https://link.aps.org/doi/10.1103/PhysRev.90.779. Cited on page 11.

[13] Borovik-Romanov, A. S. and M. P. Orlova: *Magnetic properties of cobalt and manganese carbonates*. Soviet Physics—JETP, 4:531–534, 1957. Cited 2 times on page 11 e 12.

[14] Dzyaloshinsky, I.: *A thermodynamic theory of "weak" ferromagnetism of antiferromagnetics*. Journal of Physics and Chemistry of Solids, 4(4):241–255, 1958. https://www.sciencedirect.com/science/article/pii/0022369758900763. Cited on page 11.

[15] Moriya, Tôru: *New Mechanism of Anisotropic Superexchange Interaction*. Physical Review Letters, 4:228–230, 1960. https://link.aps.org/doi/10.1103/PhysRevLett.4.228. Cited on page 11.

[16] Crépieux, A. and C. Lacroix: *Dzyaloshinsky–Moriya interactions induced by symmetry breaking at a surface*. Journal of Magnetism and Magnetic Materials, 182(3):341–349, 1998. https://www.sciencedirect.com/science/article/pii/S0304885397010445. Cited on page 12.

[17] Uchida, Masaya, Yoshinori Onose, Yoshio Matsui, and Yoshinori Tokura: *Real-Space Observation of Helical Spin Order*. Science, 311(5759):359–361, 2006. https://www.science.org/doi/abs/10.1126/science.1120639. Cited on page 12.

[18] Kousaka, Yusuke, Shin ichiro Yano, Jun ichiro Kishine, Yusuke Yoshida, Katsuya Inoue, Koichi Kikuchi, and Jun Akimitsu: *Chiral Magnetic Ordering and Commensurate-to-Incommensurate Transition in CuB2O4*. Journal of the Physical Society of Japan, 76(12):123709, 2007. https://doi.org/10.1143/JPSJ.76.123709. Cited on page 12.

[19] Stishov, Sergei M. and A. E. Petrova: *Itinerant helimagnet MnSi*. Physics-Uspekhi, 54(11):1117, 2011. https://dx.doi.org/10.3367/UFNe.0181.201111b.1157. Cited on page 12.

[20] Kishine, Jun ichiro and A.S. Ovchinnikov: *Chapter One - Theory of Monoaxial Chiral Helimagnet*, volume 66 of *Solid State Physics*, pages 1–130. Aca-

demic Press, 2015. https://www.sciencedirect.com/science/article/pii/S0081194715000041. Cited 2 times on page 12 e 13.

[21] Bode, M., M. Heide, K. von Bergmann, P. Ferriani, S. Heinze, G. Bihlmayer, A. Kubetzka, O. Pietzsch, S. Blügel, and R. Wiesendanger: *Chiral magnetic order at surfaces driven by inversion asymmetry.* Nature, 447(7141):190–193, 2007. https://doi.org/10.1038/nature05802. Cited on page 12.

[22] Ferriani, P., K. von Bergmann, E. Y. Vedmedenko, S. Heinze, M. Bode, M. Heide, G. Bihlmayer, S. Blügel, and R. Wiesendanger: *Atomic-Scale Spin Spiral with a Unique Rotational Sense: Mn Monolayer on W(001).* Physical Review Letters, 101:027201, 2008. https://link.aps.org/doi/10.1103/PhysRevLett.101.027201. Cited on page 12.

[23] Grigoriev, S. V., Yu. O. Chetverikov, D. Lott, and A. Schreyer: *Field Induced Chirality in the Helix Structure of* Dy/Y *Multilayer Films and Experimental Evidence for Dzyaloshinskii-Moriya Interaction on the Interfaces.* Physical Review Letters, 100:197203, 2008. https://link.aps.org/doi/10.1103/PhysRevLett.100.197203. Cited on page 12.

[24] Jiang, Wanjun, Gong Chen, Kai Liu, Jiadong Zang, Suzanne G.E. te Velthuis, and Axel Hoffmann: *Skyrmions in magnetic multilayers.* Physics Reports, 704:1–49, 2017. https://www.sciencedirect.com/science/article/pii/S0370157317302934. Cited 2 times on page 12 e 13.

[25] Göbel, Börge, Ingrid Mertig, and Oleg A. Tretiakov: *Beyond skyrmions: Review and perspectives of alternative magnetic quasiparticles.* Physics Reports, 895:1–28, 2021. https://www.sciencedirect.com/science/article/pii/S0370157320303525. Cited 2 times on page 12 e 13.

[26] Perk, J. H. H. and H. W. Capel: *Antisymmetric exchange, canting and spiral structure.* Physics Letters A, 58(2):115–117, 1976. https://www.sciencedirect.com/science/article/pii/0375960176905156. Cited 2 times on page 13 e 78.

[27] Calvo, M.: *Exact equivalence of the Dzialoshinski-Moriya exchange interaction and quadratic spin anisotropies.* Journal of Physics C: Solid State Physics, 14(24):L733, 1981. https://dx.doi.org/10.1088/0022-3719/14/24/003. Cited 2 times on page 13 e 78.

[28] Rubinstein, Michael, Boris Shraiman, and David R. Nelson: *Two-dimensional* XY *magnets with random Dzyaloshinskii-Moriya interactions.* Physical Review B, 27:1800–1811, 1983. https://link.aps.org/doi/10.1103/PhysRevB.27.1800. Cited 2 times on page 13 e 40.

[29] Klein, Lior and Amnon Aharony: *Crossover and multicriticality due to the Dzyaloshinsky-Moriya interaction.* Physical Review B, 44:856–858, 1991. https://link.aps.org/doi/10.1103/PhysRevB.44.856. Cited 3 times on page 13, 72 e 78.

[30] Ho, Kwan yuet, T. R. Kirkpatrick, Yan Sang, and D. Belitz: *Ordered phases of itinerant Dzyaloshinsky-Moriya magnets and their electronic properties.* Physical Review B, 82:134427, 2010. https://link.aps.org/doi/10.1103/PhysRevB.82.134427. Cited on page 13.

[31] Proskurin, Igor, Alexander S. Ovchinnikov, and Jun ichiro Kishine: *On Berezinskii-Kosterlitz-Thouless transition in monoaxial chiral helimagnets.* Journal of Physics: Conference Series, 903(1):012062, 2017. https://dx.doi.org/10.1088/1742-6596/903/1/012062. Cited on page 13.

[32] Azizi, F. and H. Rezania: *Dynamical and static spin structure factors of Heisenberg antiferromagnet on honeycomb lattice in the presence of Dzyaloshinskii-Moriya interaction.* Physica E: Low-dimensional Systems and Nanostructures, 114:113603, 2019. https://www.sciencedirect.com/science/article/pii/S138694771930476X. Cited on page 13.

[33] Hui-Ping, Liu, Sun Yun-Zhou, and Yi Lin: *New Monte Carlo Simulations to a Generalized XY Model.* Chinese Physics Letters, 23(2):316, 2006. https://dx.doi.org/10.1088/0256-307X/23/2/012. Cited 2 times on page 13 e 18.

[34] Yun-Zhou, Sun, Liu Hui-Ping, and Yi Lin: *Monte Carlo Study of Planar Rotator Model with Weak Dzyaloshinsky–Moriya Interaction.* Communications in Theoretical Physics, 46(4):663, 2006. https://dx.doi.org/10.1088/0253-6102/46/4/021. Cited 3 times on page 13, 27 e 28.

[35] Vedmedenko, E. Y., L. Udvardi, P. Weinberger, and R. Wiesendanger: *Chiral magnetic ordering in two-dimensional ferromagnets with competing Dzyaloshinsky-Moriya interactions.* Physical Review B, 75:104431, 2007. https://link.aps.org/doi/10.1103/PhysRevB.75.104431. Cited on page 13.

[36] Yi, Su Do, Shigeki Onoda, Naoto Nagaosa, and Jung Hoon Han: *Skyrmions and anomalous Hall effect in a Dzyaloshinskii-Moriya spiral magnet.* Physical Review B, 80:054416, 2009. https://link.aps.org/doi/10.1103/PhysRevB.80.054416. Cited on page 13.

[37] Hamann, A., D. Lamago, Th. Wolf, H. v. Löhneysen, and D. Reznik: *Magnetic Blue Phase in the Chiral Itinerant Magnet MnSi.* Physical Review Letters, 107:037207, 2011. https://link.aps.org/doi/10.1103/PhysRevLett.107.037207. Cited on page 13.

[38] Sun, Yun Zhou, Lin Yi, and Jian Sheng Wang: *Effects of Dzyaloshinsky-Moriya Interaction on Planar Rotator Model on Triangular Lattice*. Communications in Computational Physics, 11(4):1169–1181, 2012. https://doi.org/10.4208/cicp.100410.020211s. Cited 2 times on page 13 e 28.

[39] Buhrandt, Stefan and Lars Fritz: *Skyrmion lattice phase in three-dimensional chiral magnets from Monte Carlo simulations*. Physical Review B, 88:195137, 2013. https://link.aps.org/doi/10.1103/PhysRevB.88.195137. Cited on page 13.

[40] Nishikawa, Yoshihiko and Koji Hukushima: *Phase transitions and ordering structures of a model of a chiral helimagnet in three dimensions*. Physical Review B, 94:064428, 2016. https://link.aps.org/doi/10.1103/PhysRevB.94.064428. Cited on page 13.

[41] Belemuk, A. M. and S. M. Stishov: *Phase transitions in chiral magnets from Monte Carlo simulations*. Physical Review B, 95:224433, 2017. https://link.aps.org/doi/10.1103/PhysRevB.95.224433. Cited on page 13.

[42] Liu, Huiping, J. A. Plascak, and D. P. Landau: *Incommensurability and phase transitions in two-dimensional XY models with Dzyaloshinskii-Moriya interactions*. Physical Review E, 97:052118, 2018. https://link.aps.org/doi/10.1103/PhysRevE.97.052118. Cited 5 times on page 13, 14, 23, 27 e 28.

[43] Olsson, Peter: *Self-Consistent Boundary Conditions in the* 2DXY *Model*. Physical Review Letters, 73:3339–3342, 1994. https://link.aps.org/doi/10.1103/PhysRevLett.73.3339. Cited 2 times on page 14 e 21.

[44] Ohta, Takao and David Jasnow: XY *model and the superfluid density in two dimensions*. Physical Review B, 20:139–146, 1979. https://link.aps.org/doi/10.1103/PhysRevB.20.139. Cited on page 16.

[45] Cha, Min Chul, Matthew P. A. Fisher, S. M. Girvin, Mats Wallin, and A. Peter Young: *Universal conductivity of two-dimensional films at the superconductor-insulator transition*. Physical Review B, 44:6883–6902, 1991. https://link.aps.org/doi/10.1103/PhysRevB.44.6883. Cited on page 16.

[46] Nagaosa, N.: *Quantum Field Theory in Condensed Matter Physics*. Texts and Monographs in Physics. Springer, 1999. https://books.google.com.br/books?id=C9uAXYIlFhMC. Cited on page 16.

[47] Alcaraz, F. C. and W. F. Wreszinski: *The Heisenberg XXZ Hamiltonian with Dzyaloshinsky-Moriya interactions*. Journal of Statistical Physics, 58:45–56, 1990. https://doi.org/10.1007/BF01020284. Cited 3 times on page 17, 30 e 48.

[48] Metropolis, Nicholas, Arianna W. Rosenbluth, Marshall N. Rosenbluth, Augusta H. Teller, and Edward Teller: *Equation of State Calculations by Fast Computing Machines*. The Journal of Chemical Physics, 21(6):1087–1092, 1953. https://doi.org/10.1063/1.1699114. Cited 2 times on page 18 e 49.

[49] Swendsen, Robert H. and Jian Sheng Wang: *Nonuniversal critical dynamics in Monte Carlo simulations*. Physical Review Letters, 58:86–88, 1987. https://link.aps.org/doi/10.1103/PhysRevLett.58.86. Cited on page 18.

[50] Vetterling, William T. and William H. Press: *Numerical recipes: example book C*. Cambridge University Press, 1992. Cited 2 times on page 22 e 53.

[51] Challa, Murty S. S. and D. P. Landau: *Critical behavior of the six-state clock model in two dimensions*. Physical Review B, 33:437–443, 1986. https://link.aps.org/doi/10.1103/PhysRevB.33.437. Cited 2 times on page 22 e 23.

[52] Rastelli, E., S. Regina, and A. Tassi: *Monte Carlo simulation for square planar model with a small fourfold symmetry-breaking field*. Physical Review B, 70:174447, 2004. https://link.aps.org/doi/10.1103/PhysRevB.70.174447. Cited on page 22.

[53] Binder, Kurt: *Finite size scaling analysis of Ising model block distribution functions*. Zeitschrift für Physik B Condensed Matter, 43:119–140, 1981. https://doi.org/10.1007/BF01293604. Cited 2 times on page 23 e 55.

[54] Fisher, M. E.: *Proceedings of the International Summer School Enrico Fermi 1970, Course 51, Varenna, Italy*. 1971. Cited on page 23.

[55] Hsieh, Yun Da, Ying Jer Kao, and Anders W. Sandvik: *Finite-size scaling method for the Berezinskii–Kosterlitz–Thouless transition*. Journal of Statistical Mechanics: Theory and Experiment, 2013(09):P09001, 2013. http://dx.doi.org/10.1088/1742-5468/2013/09/P09001. Cited 3 times on page 26, 27 e 28.

[56] Nguyen, Phong H. and Massimo Boninsegni: *Superfluid Transition and Specific Heat of the 2D x-y Model: Monte Carlo Simulation*. Applied Sciences, 11(11), 2021. https://www.mdpi.com/2076-3417/11/11/4931. Cited 3 times on page 26, 27 e 28.

[57] Kosterlitz, J. M. and D. J. Thouless: *Chapter 5 Two-Dimensional Physics*. 7:371–433, 1978. https://www.sciencedirect.com/science/article/pii/S0079641708601754. Cited 2 times on page 32 e 33.

[58] Gupta, Rajan and Clive F. Baillie: *Critical behavior of the two-dimensional XY model*. Physical Review B, 45:2883–2898, 1992. https://link.aps.org/doi/10.1103/PhysRevB.45.2883. Cited 3 times on page 32, 33 e 39.

[59] Selke, W.: *Critical Binder cumulant of two-dimensional Ising models.* The European Physical Journal B - Condensed Matter and Complex Systems, 51:223–228, 2006. https://doi.org/10.1140/epjb/e2006-00209-7. Cited 2 times on page 44 e 62.

[60] Fisher, M. E.: *The renormalization group in the theory of critical behavior.* Reviews of Modern Physics, 46:597–616, 1974. https://link.aps.org/doi/10.1103/RevModPhys.46.597. Cited on page 47.

[61] Campostrini, Massimo, Martin Hasenbusch, Andrea Pelissetto, Paolo Rossi, and Ettore Vicari: *Critical exponents and equation of state of the three-dimensional Heisenberg universality class.* Physical Review B, 65:144520, 2002. https://link.aps.org/doi/10.1103/PhysRevB.65.144520. Cited on page 47.

[62] Li, Wei, H. P. Kunkel, X. Z. Zhou, Gwyn Williams, Y. Mukovskii, and D. Shulyatev: *Estimates of the critical exponents of single-crystal* $La_{0.73}Ba_{0.27}MnO_3$. Physical Review B, 70:214413, 2004. https://link.aps.org/doi/10.1103/PhysRevB.70.214413. Cited on page 47.

[63] Holm, Christian and Wolfhard Janke: *Critical exponents of the classical three-dimensional Heisenberg model: A single-cluster Monte Carlo study.* Physical Review B, 48:936–950, 1993. https://link.aps.org/doi/10.1103/PhysRevB.48.936. Cited 4 times on page 55, 56, 67 e 77.

[64] Zhu, W., Shou shu Gong, and D. N. Sheng: *Identifying spinon excitations from dynamic structure factor of spin-1/2 Heisenberg antiferromagnet on the Kagome lattice.* Proceedings of the National Academy of Sciences, 116(12):5437–5441, 2019. https://www.pnas.org/doi/abs/10.1073/pnas.1807840116. Cited on page 56.

[65] Yadav, Ravi, Satoshi Nishimoto, Manuel Richter, Jeroen van den Brink, and Rajyavardhan Ray: *Large off-diagonal exchange couplings and spin liquid states in* C_3*-symmetric iridates.* Physical Review B, 100:144422, 2019. https://link.aps.org/doi/10.1103/PhysRevB.100.144422. Cited on page 56.

[66] Suzuki, Masuo: *New Universality of Critical Exponents.* Progress of Theoretical Physics, 51(6):1992–1993, 1974. https://doi.org/10.1143/PTP.51.1992. Cited on page 66.

[67] Khan, N., P. Sarkar, A. Midya, P. Mandal, and P. K. Mohanty: *Continuously Varying Critical Exponents Beyond Weak Universality.* Scientific Reports, 7(1):45004, 2017. https://doi.org/10.1038/srep45004. Cited on page 66.

[68] Campostrini, Massimo, Martin Hasenbusch, Andrea Pelissetto, Paolo Rossi, and Ettore Vicari: *Critical behavior of the three-dimensional* XY *universality class.* Physical

Review B, 63:214503, 2001. https://link.aps.org/doi/10.1103/PhysRevB.63.214503. Cited on page 77.

[69] Nonomura, Yoshihiko and Yusuke Tomita: *Nonequilibrium behaviors of the three-dimensional Heisenberg model in the Swendsen-Wang algorithm*. Physical Review E, 93:012101, 2016. https://link.aps.org/doi/10.1103/PhysRevE.93.012101. Cited on page 77.

[70] Krech, M. and D. P. Landau: *Spin-dynamics simulations of the three-dimensional* XY *model: Structure factor and transport properties*. Physical Review B, 60:3375–3387, 1999. https://link.aps.org/doi/10.1103/PhysRevB.60.3375. Cited on page 77.

[71] Campostrini, Massimo, Martin Hasenbusch, Andrea Pelissetto, and Ettore Vicari: *Theoretical estimates of the critical exponents of the superfluid transition in* ^{4}He *by lattice methods*. Physical Review B, 74:144506, 2006. https://link.aps.org/doi/10.1103/PhysRevB.74.144506. Cited on page 77.

[72] Chen, Kun, Alan M. Ferrenberg, and D. P. Landau: *Static critical behavior of three-dimensional classical Heisenberg models: A high-resolution Monte Carlo study*. Physical Review B, 48:3249–3256, 1993. https://link.aps.org/doi/10.1103/PhysRevB.48.3249. Cited on page 77.

[73] Pelissetto, Andrea and Ettore Vicari: *Critical phenomena and renormalization-group theory*. Physics Reports, 368(6):549–727, 2002. https://www.sciencedirect.com/science/article/pii/S0370157302002193. Cited on page 79.

[74] Xu, Wanwan, Yanan Sun, Jian Ping Lv, and Youjin Deng: *High-precision Monte Carlo study of several models in the three-dimensional U(1) universality class*. Physical Review B, 100:064525, 2019. https://link.aps.org/doi/10.1103/PhysRevB.100.064525. Cited on page 79.

[75] Bureau International des Poids et Mesures (BIMP): *Evaluation of measurement data – Guide to the expression of uncertainty in measurement.*, 2008. https://www.bipm.org/documents/20126/2071204/JCGM%20100%202008%20E.pdf/cb0ef43fbaa5-11cf-3f85-4dcd86f77bd6. Cited 2 times on page 91 e 96.

Appendix

APPENDIX A – Averages and uncertainties of the thermodynamic quantities

To estimate the expected averages and corresponding uncertainties of quantities such as energy $\langle E \rangle$, order parameter $\langle m \rangle$, specific heat c_v, order parameter susceptibility χ, order parameter fourth-order cumulant U_4, etc., the obtained total data from the MC simulations are firstly divided into bins. Basically, the total data comprise several files containing two rows, one filled out with energy and the other one with the order parameter, as described in Subsections 2.2.3 and 3.2.3. By performing separate statistics on each bin, and then joining the resulting averages from all of them, the expected values and corresponding uncertainties are computed for each desired quantity.

As an example, the total data formed by t_m pairs of energy-order parameter is considered. Then, they are divided into n bins. Each one has $l = t_m/n$ pairs of energy-order parameter. Thus, separate statistics on each bin produce

$$\langle A \rangle_i = \frac{1}{l} \sum_{t=i\times l+1}^{(i+1)\times l} A_t, \quad \text{with} \quad i = 0, 1, 2, ..., n-1, \tag{A.1}$$

where the n bins are labeled by an index i, and A is used to represent either E or m. It should be stressed that in the process of computing $\langle E \rangle_i$ and $\langle m \rangle_i$, their corresponding quantities $c_{v,i}$, χ_i and $U_{4,i}$ for each bin data i can also be obtained. As long as these intermediate data have been partially stored, the final averages come from

$$\bar{F} = \frac{1}{n} \sum_{i=0}^{n-1} F_i, \tag{A.2}$$

where F_i may be $\langle E \rangle_i$, $\langle m \rangle_i$, $c_{v,i}$, χ_i and $U_{4,i}$. The uncertainty associated to $\bar{F}$ is estimated by [75]

$$s\left(\bar{F}\right) = \frac{s(F)}{\sqrt{n}}, \tag{A.3}$$

where $s(F)$ is the sample standard deviation

$$s^2\left(F\right) = \frac{1}{n-1} \sum_{i=0}^{n-1} \left(F_i - \bar{F}\right)^2. \tag{A.4}$$

The number of bins n must be sufficiently large to ensure that $\bar{F}$ provides a reliable estimate of the expected value of the random variable F. Likewise, $s\left(\bar{F}\right)$ is supposed to provide a reliable estimate of the variance $s^2\left(\bar{F}\right) \cong \sigma^2/n$ [75]. In this work, n has been chosen according to the data size from the MC simulations, ranging as $n = 20, 100, 500, 1000$.

APPENDIX B – Single histogram method

The probability distribution of states of a system in thermal equilibrium at a temperature T, having energy E and magnetization M, is given, according to the Boltzmann distribution, by [6]

$$P_\beta(E,M) = \frac{W(E,M)}{Z(\beta)} e^{-\beta E}, \tag{B.1}$$

where $\beta = 1/k_B T$, $Z(\beta)$ is the canonical partition function of the system, $W(E,M)$ is the density of states with energy E and magnetization M, and k_B is the Boltzmann constant. By performing a MC simulation for this system at a temperature β_0, the joint probability $P_{\beta_0}(E,M)$ at β_0 can be estimated from the measured values of energy and magnetization during the simulation in the thermal equilibrium. The frequency of these data after t_m measurements produces a histogram $H(E,M)$, which can be used to estimate $P_{\beta_0}(E,M)$ as

$$P_{\beta_0}(E,M) \approx \frac{H(E,M)}{t_m}. \tag{B.2}$$

This equation provides a way to also estimate the density of states term $W(E,M)$ in Equation (B.1), which is temperature independent. Thus, one has

$$W(E,M) \approx \frac{Z(\beta_0)}{t_m} H(E,M)\, e^{-\beta_0 E}. \tag{B.3}$$

The density of states in Equation (B.1) is replaced by its estimate in Equation (B.3), so that the joint probability $P_\beta(E,M)$ can be written as

$$P_\beta(E,M) \approx \frac{Z(\beta_0)}{t_m Z(\beta)} H(E,M) e^{-(\beta-\beta_0)E}. \tag{B.4}$$

The unknown quantity $Z(\beta_0)/t_m Z(\beta)$ can be solved by normalizing $P_\beta(E,M)$, leading to the single histogram reweighting, which is given by the probability distribution

$$P_\beta(E,M) = \frac{H(E,M)\, e^{-\Delta\beta E}}{\sum_{E,M} H(E,M)\, e^{-\Delta\beta E}}, \tag{B.5}$$

where $\Delta\beta = \beta - \beta_0$. Then, the above equation can be easily used to compute further values for other related quantities which may be even a function of E and M. If this function is represented by $f(E,M)$, its expected value, $\langle f(E,M)\rangle_\beta$, for the system at a temperature T, is calculated as

$$\langle f(E,M)\rangle_\beta = \sum_{E,M} f(E,M)\, P_\beta(E,M). \tag{B.6}$$

The reliability of the above method in estimating $\langle f(E,M)\rangle_\beta$ will depend, of course, on the data size t_m. When $t_m \to \infty$ in Equation (B.2), the approximation for the probability distribution tends to the exact one as $H(E,M)/t_m \to P_{\beta_0}(E,M)$. Since t_m

is just the number of measurements of E and M stored in $H(E, M)$, the larger t_m, the better will be the estimate for $P_{\beta_0}(E, M)$ and, consequently, the expected values. Besides, the data quality is also important, since they will be contained in $H(E, M)$.

In practice, the E and M values coming from the MC simulations may be tabulated in a file or in the computer RAM storage. This means that the data are organized in t_m rows by two columns with energy and magnetization. However, if some other quantity f having dependence on E and/or M was also measured and stored during the simulation, Equation (B.6) can be written as

$$\langle f(E, M)\rangle_\beta = \frac{\sum_{t=1}^{t_m} f(E_t, M_t)\, e^{-\Delta\beta E_t}}{\sum_{t=1}^{t_m} e^{-\Delta\beta E_t}}. \tag{B.7}$$

The above equation has been used in the algorithms of the programs in this work to obtain the relevant quantities through their extrapolation at other temperatures T around those ones where the MC simulations were performed, refered to as T_0. Figure 39 shows an example for the planar rotator model with DM interaction with $d = 1$, where the method was applied to calculate the order parameter fourth-order cumulant U_4 (defined by Equation (2.18)) as a function of T for several lattice sizes. Each curve was obtained using the histograms from just one temperature by using Equation (B.7).

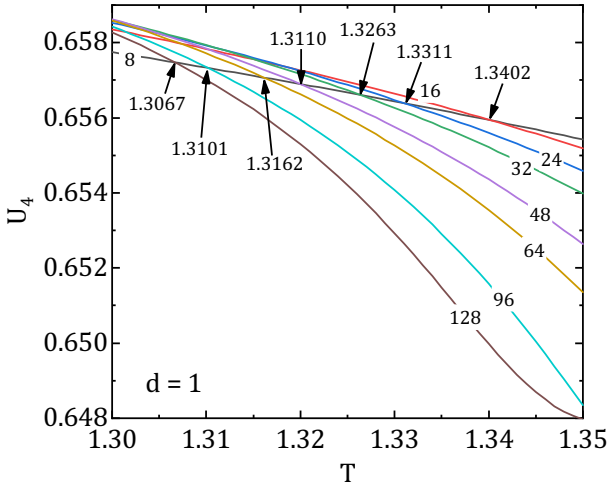

Figure 39 – An example of the single histogram method application to obtain thermodynamic functions by extrapolation. U_4 is the order parameter fourth-order cumulant as a function of the temperature T, in J/k_B units. The number on each curve is the corresponding lattice size L. The arrows indicate the location where the curves with $L > 8$ cross the curve with $L = 8$. Each curve was constructed by extrapolations from data of MC simulations at just one temperature value.

To check the reliability of the extrapolation, the histogram of the energy distribution at the extrapolated temperature T may be compared to that one at the MC simulation temperature T_0, as shown in Figure 40. They correspond to the energy distribution from

the data of the lattice size $L = 128$, the largest system considered in the study of the model in Chapter 2. Because of its size, it demands more MC simulations due to its large number of possible configurations in the thermal equilibrium. As one can see, the extrapolated distribution has kept its shape very similar to the distribution at the MC simulation temperature. For the purpose of analyzing crossing points of the cumulant curves, the histogram method has proved to work well up to the extrapolated temperatures T indicated in Figure 39. For temperatures relatively far from T_0, the histogram method may not be reliable in obtaining the cumulants due to deformations in one of the tails of the extrapolated energy distribution.

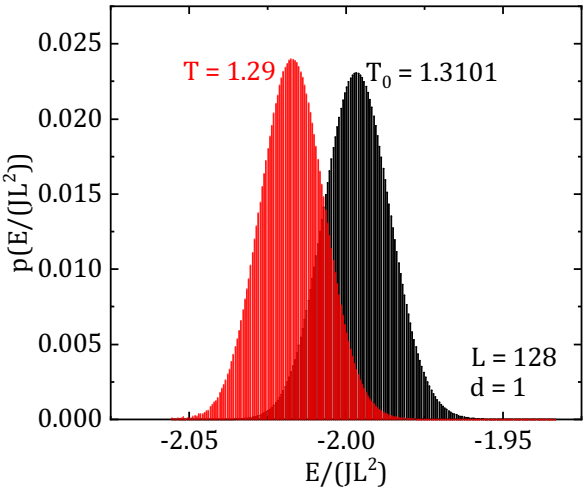

Figure 40 – Energy distributions of a system based on the model in Chapter 2, given by a square lattice with size $L = 128$. The distributions correspond to two different temperatures. $T_0 = 1.3101$ is the temperature where the MC simulation was performed. The other distribution comes from the extrapolation by using the single histogram method at $T = 1.29$. This is an example showing that the extrapolated distribution has not deformed up to the interest temperature $T = 1.29$.

APPENDIX C – Fourth-order Binder cumulant crossing temperature estimate

Since the single histogram method does not provide a simple analytical expression to invert the U_4 dependence on T into T explicitly dependent of U_4, the alternative is to approximate U_4 by some appropriate function of T. This appendix describes a method to estimate the crossing temperature where two cumulants intercept each other. As this is not a type of direct measurement of a quantity, as described in Appendix A, it is called an indirect measurement.

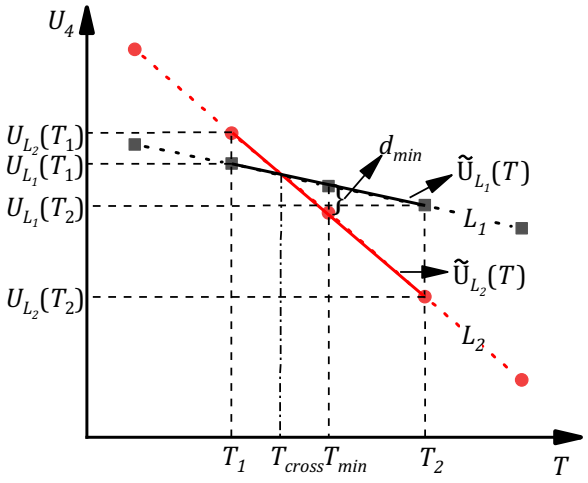

Figure 41 – Illustration about the T_{cross} calculation, which is the crossing temperature of a cumulant for a lattice size L_1 (squares) and other cumulant for a lattice size L_2 (circles). The points are the cumulant values obtained through single histogram method on MC simulation data, identified as U_{L_1} and U_{L_2}. The full lines $\tilde{U}_{L_1}(T)$ and $\tilde{U}_{L_2}(T)$ are straight lines connecting the points at T_1 and T_2 for both lattice sizes, respectively. The dashed lines across the cumulant data are just guide to eyes.

Figure 41 shows an example of the region in the U_4-T plane where two cumulants cross each other. The cumulant U_{L_1} belongs to a system with a lattice size L_1, represented by the square symbols. Likewise, U_{L_2} is the cumulant from a system with lattice size L_2, represented by the circles. Both U_{L_1} and U_{L_2} are calculated at each T value by using the single histogram method.

The location where U_{L_1} and U_{L_2} intercept each other is found by first searching the smallest difference of the cumulants in the whole temperature interval. This difference is shown as d_{min} in Figure 41, which occur at $T = T_{\text{min}}$. From this point, a temperature sub-interval $[T_1, T_2]$ is defined, where U_{L_1} and U_{L_2} are approximated by straight line

functions $\widetilde{U}_{L_1}(T) = b_{L_1} - a_{L_1}T$ and $\widetilde{U}_{L_2}(T) = b_{L_2} - a_{L_2}T$, respectively. These curves are shown as full lines in Figure 41. The temperatures $T_1, T_{\min}$, and T_2 are equally spaced by ΔT-steps. The constants a_{L_1} and b_{L_1} depend on U_{L_1} calculated at T_1 e T_2, besides being also T_1 and T_2 dependent. In the same way for a_{L_2} and b_{L_2}, but both of them being U_{L_2} dependent. The crossing temperature T_{cross} satisfies $\widetilde{U}_{L_1}(T_{\text{cross}}) = \widetilde{U}_{L_2}(T_{\text{cross}})$. This equation is solved for T_{cross}, resulting in

$$T_{\text{cross}} = \frac{b_{L_2} - b_{L_1}}{a_{L_2} - a_{L_1}}. \tag{C.1}$$

Then, by using the points in the U_4-T plane for $T = T_1$ and $T = T_2$ shown in Figure 41 to determine a_{L_1}, b_{L_1}, a_{L_2} and b_{L_2}, one obtains

$$T_{\text{cross}} = T_2 - \frac{\Delta U_{T_2}}{\Delta U_{T_2} - \Delta U_{T_1}} \Delta T_{12}, \tag{C.2}$$

where ΔU_{T_1}, ΔU_{T_2} e ΔT_{12} are defined as

$$\Delta U_{T_1} = U_{L_2}(T_1) - U_{L_1}(T_1), \tag{C.3a}$$

$$\Delta U_{T_2} = U_{L_2}(T_1) - U_{L_1}(T_2). \tag{C.3b}$$

$$\Delta T_{12} = T_2 - T_1, \tag{C.3c}$$

Equation (C.2) together with the definitions (C.3) show that T_{cross} is a function of $U_{L_1}(T_1)$, $U_{L_2}(T_1)$, $U_{L_1}(T_2)$ and $U_{L_2}(T_2)$, which in turn are extrapolated at T_1 e T_2 via the single histogram method on MC simulation data simulated at some other temperature. The mean values and uncertainties of these cumulants can be calculated as the standard deviation of their mean values by applying the method in Appendix A on the generated data at T_1 e T_2 from the single histogram method. These uncertainties propagate to the final estimate of T_{cross} through its uncertainty δT_{cross}, given by [75]

$$\delta T_{\text{cross}} = \pm \sqrt{\sum_{i=1}^{2}\sum_{j=1}^{2} \left[\frac{\partial T_{\text{cross}}}{\partial U_{L_i}(T_j)}\right]^2 \left[\delta U_{L_i}(T_j)\right]^2}, \tag{C.4}$$

where $U_{L_i}(T_j)$ is the cumulant of the lattice L_i at $T = T_j$, and $\delta U_{L_i}(T_j)$ is the uncertainty of this cumulant value. The partial derivatives are solved based on Equation (C.2) for T_{cross}. The final result for δT_{cross} is compactly written as

$$\delta T_{\text{cross}} = \pm 2C\Delta T, \tag{C.5}$$

where C contains the contributions from the cumulants and their uncertainties, which reads

$$C = \frac{\sqrt{\left\{\left[\delta U_{L_1}(T_1)\right]^2 + \left[\delta U_{L_2}(T_1)\right]^2\right\}\left(\Delta U_{T_2}\right)^2 + \left\{\left[\delta U_{L_1}(T_2)\right]^2 + \left[\delta U_{L_2}(T_2)\right]^2\right\}\left(\Delta U_{T_1}\right)^2}}{\left(\Delta U_{T_2} - \Delta U_{T_1}\right)^2}. \tag{C.6}$$

The ΔT value choice may depend on the studied model. For the cumulant crossings analysis, $\Delta T = 0.001$ was fixed for the planar rotator model in subsection 2.3.1, and $\Delta T = 0.0001$ for the 3-dimensional Heisenberg model in subsection3.3.1.

Annex

ANNEX A – Published articles

PHYSICAL REVIEW E **106**, 044116 (2022)

Incommensurate phases in the two-dimensional XY model with Dzyaloshinskii-Moriya interactions

G. Albuquerque Silva,[1] J. A. Plascak,[1,2,3] and D. P. Landau[3]

[1]*Departamento de Física, Instituto de Ciências Exatas, Universidade Federal de Minas Gerais, C.P. 702, 30123-970 Belo Horizonte, MG, Brazil*

[2]*Universidade Federal da Paraíba, Centro de Ciências Exatas e da Natureza–Campus I, Departamento de Física, CCEN Cidade Universitária, 58051-970 João Pessoa, PB, Brazil*

[3]*Center for Simulational Physics, University of Georgia, Athens, Georgia 30602, USA*

(Received 2 July 2022; accepted 27 September 2022; published 13 October 2022)

The two-dimensional XY model with Dzyaloshinskii-Moriya interaction has been studied through extensive Monte Carlo simulations. A hybrid algorithm consisting of single-spin Metropolis and Swendsen-Wang cluster-spin updates has been employed. Single histogram techniques have been used to obtain the thermodynamic variables of interest and finite-size-scaling analysis has led to the phase transition behavior in the thermodynamic limit. Fluctuating boundary conditions have been utilized in order to match the incommensurability between the spin structures and the finite lattice sizes due to the Dzyaloshinskii-Moriya interaction. The effects of the fluctuating boundary conditions have been analyzed in detail in both commensurate and incommensurate cases. The Berezinskii-Kosterlitz-Thouless transition temperature has been obtained as a function of the Dzyaloshinskii-Moriya interaction and the results are in excellent agreement with the exact equation for the transition line. The spin-spin correlation function critical exponent has been computed as a function of the Dzyaloshinskii-Moriya interaction and temperature. In the incommensurate cases, optimal sizes for the finite lattices and the distribution of the boundary shift angle have been extracted. Analysis of the low temperature configurations and the corresponding vortex-antivortex pairs have also been addressed in some regions of the phase diagram.

DOI: 10.1103/PhysRevE.106.044116

I. INTRODUCTION

The two-dimensional XY model with Dzyaloshinskii-Moriya (DM) interactions has received a great deal of attention in recent years. The XY portion of the model [1] can be applied, e.g., to superfluid films [2] and Josephson junction arrays [3], and in two dimensions the model undergoes a Berezinskii-Kosterlitz-Thouless (BKT) transition characterized by an exponentially divergent correlation length and in-plane susceptibility [4–6]. On the other hand, the DM interaction part of the model [7,8], besides the original motivation for explaining weak ferromagnetism in some antiferromagnetic materials, is also responsible for some new special phenomena including, e.g., spin canting out of the CuO_2 plane in $LaCu_2O_4$ superconductors [9] and helical spin order in $Fe_xCo_{1-x}Si$ alloys [10].

The importance of the DM interaction has also been noticed in Mn monolayers, where the adjacent spins are not perfectly antiferromagneticly aligned, but slightly canted, resulting in a spin spiral structure with chiral order [11,12]. A nonzero average chirality has also been observed in Dy/Y multilayer films [13], indicating that DM interactions also exist in this material, with the chirality being ascribed to the lack of the inversion symmetry at the interfaces of the multilayer films.

The model with both XY exchange and additional DM interactions has been recently treated by Monte Carlo (MC) simulations [14]. However, it was previously shown that this more general model is, in fact, equivalent to an XY exchange renormalized Hamiltonian with the ground state having shifted angle orientation amongst the nearest-neighbor spins, with angles that are a function of the DM interaction [15]. As a result, depending on the strength of the DM interaction, incommensurability arises at low temperatures for the model. When defined on finite lattices, this leads to some spin configuration inconsistencies when using the usual periodic boundary conditions (PBC) to eliminate undesirable surface effects (in this case, besides the frustration of the spin alignments at the borders of the finite lattice, the energy of the system turns out to be significantly enhanced).

In order to circumvent the incommensurability problem on finite lattices, fluctuating boundary conditions (FBC) have been proposed [14,16]. In this way, it has been shown that FBC can in fact provide good results for the transition behavior in the cases where the incommensurability prevails. However, the role of this FBC on the system has not been studied in detail nor has the phase diagram been obtained over a wide range of the DM interaction strength.

In this work we have then revisited the two-dimensional XY model including DM interactions by employing more extensive MC simulations, making use of a hybrid algorithm consisting of single-spin updates following Metropolis algorithm and Swendsen-Wang cluster-spin updates. FBC have also been used for all lattice sizes to permit incommen-

 ©2022 American Physical Society

surate structures to form, i.e., to avoid artificially imposing commensurability. We have additionally employed single histogram techniques to obtain the thermodynamic variables just above, at, and below the BKT transition temperature.

The organization of the paper is as follows. In the next section, the model and the transformation we have performed are presented. Section III is devoted to the MC simulation background and the thermodynamic variables that have been computed. In Sec. IV the results are presented and discussed and in the final section some concluding remarks are addressed. In the final section, we have also stressed that, although we have an exact transition temperature for the model as function of the DM interaction, important results concerning periodic and fluctuating boundary conditions, temperature scaling relation of the correlation length critical exponent, vortex-antivortex pair configurations, and shift angle distribution for different lattice sizes should be very useful in studying other similar systems.

II. MODEL

The Hamiltonian for the ferromagnetic XY model with DM interaction can be written as

$$\mathcal{H} = -J \sum_{\langle ij \rangle} \vec{S}_i \cdot \vec{S}_j - \vec{D} \cdot \sum_{\langle ij \rangle} (\vec{S}_i \times \vec{S}_j), \tag{1}$$

where the sums are taken over nearest-neighbor pairs of sites $\langle ij \rangle$ on a square lattice, $\vec{S}_i$ is a two-component classical vector of unit length, $J > 0$ is the exchange interaction, and the DM interaction is given by the vector $\vec{D}$. By taking the DM interaction along the z axis and using the transformation proposed in Ref. [15] we get

$$\mathcal{H} = -J\sqrt{1+d^2} \sum_{\langle ij \rangle} \cos(\theta_i - \theta_j - \phi), \tag{2}$$

where $\phi = \arcsin(d/\sqrt{1+d^2})$ and we have defined $d = D/J$. Here θ_i and θ_j are the spin rotation angles of the ith and jth sites relative to the x-axis direction, respectively. The transformed Hamiltonian is thus another XY system with renormalized exchange interaction $J(d)$ and an angle phase shift $\phi(d)$, both depending on the DM interaction.

Preparing for the MC simulations, we perform an additional transformation to the above Hamiltonian, namely

$$\theta_i = \theta_i^0 - \frac{\pi}{2}(1+\sigma_i), \tag{3}$$

where σ_i takes the values ± 1 and θ_i^0 denotes a trial angle at the site i. If $\sigma_i = -1$, θ_i just keeps the same value; if $\sigma_i = 1$, it means that θ_i is rotated by an angle of π. Combining Eqs. (2) and (3) we arrive at an Ising-type Hamiltonian

$$\mathcal{H} = -\sum_{ij} J_{ij}\sigma_i\sigma_j, \tag{4}$$

where

$$J_{ij} = J\sqrt{1+d^2}\cos\left(\theta_i^0 - \theta_j^0 - \phi\right) \tag{5}$$

is an effective nonuniform Ising coupling between spins. This transformation turns out to be very useful for implementing the Swendsen-Wang cluster-spin portion of the algorithm to the model.

III. MONTE CARLO SIMULATIONS AND THERMODYNAMIC VARIABLES

A. Monte Carlo simulations

We use a hybrid Monte Carlo algorithm, which combines the standard single-spin Metropolis update [17] and the Swendsen-Wang cluster-spin update [18]. In the single-spin update, a new random orientation for the spin $\vec{S}_i$ is chosen at each site i and, if it lowers the energy, the new state is accepted; otherwise, it is accepted only with a probability according to the standard Metropolis criterion.

In order to reduce the critical slowing down of this simulation, the Swendsen-Wang (SW) cluster algorithm is also used. In an initial spin configuration of Hamiltonian (4) we choose $\sigma_i = 1$ for all the sites. If $J_{ij} > 0$ in (5), we put a bond between ith and jth sites with a probability $P(J_{ij}) = 1 - \exp(-2J_{ij}/k_BT)$, where k_B is the Boltzmann constant and T the temperature. If $J_{ij} < 0$, no bond is inserted. After clusters are constructed by putting bonds between spins, every cluster has the same possibility either to rotate by an angle of π or just to keep the same value. In general, one SW sweep related to Eqs. (3) and (4) followed after one Metropolis sweep related to Eq. (2).

As reported in Ref. [14], depending on the value of d, incommensurability emerges between the spin orientations and the finiteness of the lattice, preventing the normal use of periodic boundary conditions (PBC). This can be seen by computing the phase shift Δ across the boundaries (same row or column) of a lattice size L, which can be given by

$$\Delta = L\phi \text{ (a)}, \quad \Delta = 2n\pi \text{ (b)}, \quad L = 2n\pi/\phi \text{ (c)}, \tag{6}$$

where n is a positive nonzero integer. Whenever Eq. (6b) holds, the structure is commensurate with the lattice and the use of periodic boundary conditions will be suitable for the finite system. Otherwise, the structure is incommensurate with the lattice. Nevertheless, one can look for *optimal* lattice sizes by considering values of L close to the result obtained by using Eq. (6c) for different integers n.

However, as will be discussed in the next section, the incommensurability problem can be more efficiently circumvented by adopting fluctuating boundary conditions [16]. It can be done as follows. Suppose there is a phase shift Δ across the boundary at the same row and column, i.e., $\Delta = \theta_{1,y} - \theta_{L,y}$ and $\Delta = \theta_{x,1} - \theta_{x,L}$ for $1 \leqslant x \leqslant L$ and $1 \leqslant y \leqslant L$, in such a way that Eq. (6b) is not satisfied. After a hybrid MC sweep to update the spins while fixing Δ, one employs an extra, standard Metropolis sweep to update Δ while fixing all the spins. It has been shown that employing this FBC is better than the usual PBC when the system is incommensurate [14]. In this case, one hybrid MC step is composed by combining one Metropolis sweep, one SW sweep, and one Metropolis sweep updating just the boundary phase shift. Although one can use PBC whenever the phase shift and lattice size turn out to be commensurate, a detailed comparison between both boundary conditions are still necessary in this case.

The MC simulations have been performed on $L \times L$ square lattices, with total sites $N = L^2$ and L ranging from $L = 8$ to $L = 128$. Typically, $10^5 - 10^6$ MC data points have been discarded for equilibration and $10^8 - 3\times10^8$ MC data points have been retained for constructing the single histograms.

The sampling interval for collecting data has been 10 hybrid MC sweeps for all lattice sizes, making the total length of the simulations ten times longer than the numbers specified above. For instance, for the largest simulated lattice $L = 128$ a total of more than 3×10^9 configurations have been generated for the construction of the histograms.

B. Thermodynamic variables

The data that have been collected from the simulations consisted basically of the energy, magnetization, and the phase shifts across the boundaries. Derived quantities such as cumulants and fluctuations could also be easily obtained. However, due to the spin rotation along both the x and y directions at low temperatures (when the strength of DM interaction is not very small), the usual magnetization, which is the regular order parameter in the two-dimensional XY model [19,20], does not play the role of an order parameter in the present system. This is because of the periodic and oscillating spin arrangement that results when the DM interaction is included. Nevertheless, according to the spin arrangement in the ground state, we can define a different, and more convenient, order parameter as follows:

$$m = \frac{1}{L^2}\sqrt{M_x^2 + M_y^2},$$
$$M_x = \sum_{i=1}^{L^2} \cos[\theta_i + (x_i + y_i)\phi],$$
$$M_y = \sum_{i=1}^{L^2} \sin[\theta_i + (x_i + y_i)\phi], \tag{7}$$

where (x_i, y_i) is the coordinate of the ith spin and $x_i, y_i \in [1, L]$. Thus $m = 1$ in the ground state and, for finite lattices, should decrease as the temperature increases.

According to the finite-size-scaling theory [19,21,22] of the BKT critical behavior, the above quantity, for all temperatures T below T_c, where T_c is the BKT transition temperature, should have a power-law scaling behavior of the type

$$m \propto L^{-x}, \tag{8}$$

$T \leqslant T_c$, with a temperature dependent exponent x, and no such power-law behavior for temperatures $T > T_c$. Exactly at the transition temperature $T = T_c$ the exponent x is equal to $\eta/2$ [19], where $\eta = 1/4$ is the corresponding spin-spin correlation function critical exponent. These exponents decrease as the temperature decreases and go towards zero in the $T \to 0$ limit. Thus we can extract information about the transition, in the thermodynamic limit, by analyzing the behavior of m for different lattice sizes.

Another useful quantity is the fourth-order cumulant of the order parameter, originally suggested by Binder to analyze the Ising model critical properties [23]. In the present case we have considered the reduced form of the cumulant that can be written as

$$U_4 = 1 - \langle m^4\rangle/3\langle m^2\rangle^2, \tag{9}$$

where the angle bracket denotes a thermal average. Binder has shown that, for large enough lattices, there is a *fixed point* in the U_4 curves that is independent on the system size L and the location of this fixed point gives the transition point. So, the Binder cumulants are scale independent at the critical point and can also be used to determine the phase transition temperature T_c. For an XY model we expect that the fourth-order cumulants will become equal below the BKT transition temperature; however, corrections to finite-size scaling are sometimes still present in the cumulant crossings for the lattice sizes at hand. When these finite-size effects happen, and when the crossings have a systematic shift with L, we can extrapolate the transition temperature to the thermodynamic limit by fitting the corresponding data to [6,14,22]

$$T_{\text{cross}} = T_c + B/(\ln L)^2, \tag{10}$$

where T_{cross} is the temperature of the cumulant crossings and B a nonuniversal constant. A derivation of the above equation using a renormalization group approach can be found in Ref. [6] and more explicitly in Refs. [24,25].

IV. RESULTS

A. BKT transition temperature

The crossings of the reduced form of the cumulants (9) have been used to compute the BKT transition temperature T_c for several values of the DM interaction d. This is a very convenient quantity because we do not need *a priori* knowledge of any exponent, even when one has to use Eq. (10). We have thus studied the pure XY model with $d = 0$ for two main reasons: first, in order to compare our transition temperature with previous estimates from the literature and, second, because this transition temperature, as we will see in the next subsection, is needed to get the exact transition line as a function of the DM interaction.

The top panel in Fig. 1 shows the magnetization fourth-order cumulant U_4 as a function of the temperature T, for different values of the lattice size L. Note that here, and also in what follows, all temperatures are given in units of J/k_B. The lines in Fig. 1 have been obtained from single histogram reweighting of data taken at different temperatures T_0 for each lattice, with T_0 within the interval $0.91 < T_0 < 0.94$. We note that the larger the lattice size the more MCS had to be discarded (consequently, even more MCS had to be taken for the averages) in order to get reliable estimates of U_4. In doing so, for the larger lattices we have always tested the energy probability distribution at the crossing points (which were different from the temperature where the histograms were taken) to ensure that its wings do not suffer from large statistical uncertainties. It is apparent from the top panel of Fig. 1 that the cumulant crossings are still quite dependent on the lattice sizes. However, taking as reference the minimum size $L_{\text{min}} = 8$, there is a clear systematic decrease in the temperature crossing T_{cross} as the other sizes increase from $L > 8$, making the use of Eq. (10) quite suitable in this case. Although it cannot be clearly seen in Fig. 1, the same qualitative crossings happen when the minimum lattice sizes $L_{\text{min}} = 16$ and $L_{\text{min}} = 24$.

In fact, we would expect the cumulants to all be the same for temperatures lower than the crossing points, since the transition should always be present for any $T < T_{\text{BKT}}$. For instance, in the bottom panel of Fig. 1 we have the magnetization cumulants for the larger lattices and lower temperatures.

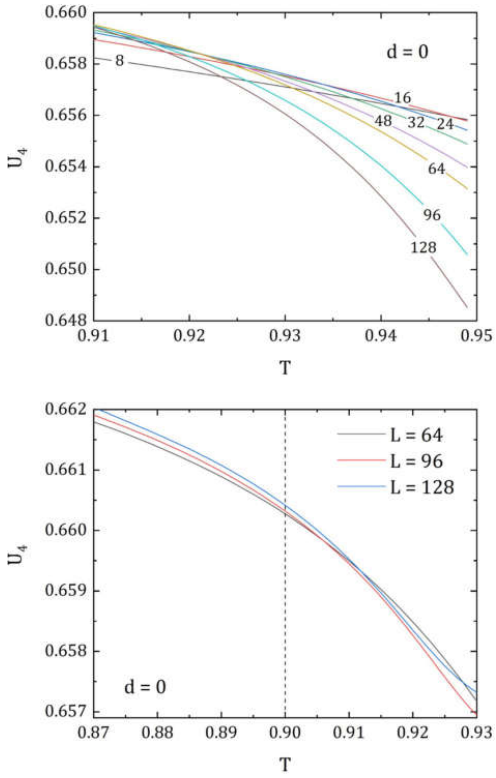

FIG. 1. Binder cumulant U_4 of the order parameter vs temperature T for different lattice sizes for the XY model, $d = 0$, using PBC. The data points, with corresponding error bars, have been omitted for clarity. In the bottom panel only the larger lattices have been considered with new data taken at $T = 0.9$ (dashed line) and analyzed with single histograms.

While the cumulants still cross for $L = 64$ and $L = 96$ (as we will see below, this crossing value is actually compatible with the extrapolated evaluation of the BKT transition temperature), the cumulants for $L = 96$ and $L = 128$ seem to be almost parallel in this region of temperature, a fact that can signal a possible BKT transition. For this reason, we can consider the crossing temperatures as an indication of the BKT transition T_c.

The temperatures of the cumulant crossings $T_{\rm cross}(L, L_{\rm min})$ are obtained from the data of the top panel of Fig. 1, taken as reference the cumulants for $L_{\rm min} = 8$, $L_{\rm min} = 16$, and $L_{\rm min} = 24$. The results are shown in Fig. 2 as a function of $(\ln L)^{-2}$. The error bars of the crossings have been estimated as described in the Appendix. It is interesting to note, in all cases, the strong size dependence of the data, with the scaling regime, as predicted by Eq. (10), being only achieved for the lattice sizes greater than $L \geqslant L_s$, with the smallest size $L_s = 64$.

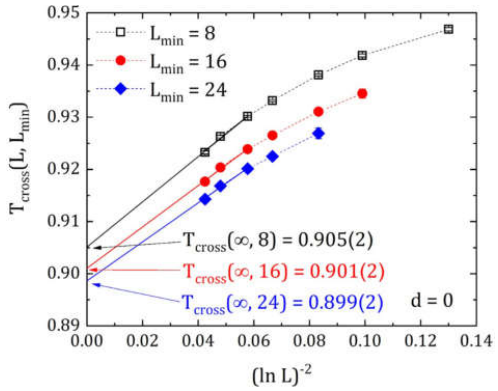

FIG. 2. Temperature of the crossings of the Binder cumulant of the order parameter $T_{\rm cross}(L, L_{\rm min})$ as a function of different reference lattice sizes $L_{\rm min}$ when $d = 0$ (XY model) using PBC. The upper, middle, and lower sets of data points correspond to crossings with $L_{\rm min} = 8$, $L_{\rm min} = 16$, and $L_{\rm min} = 24$, respectively. The dashed lines are just guides to the eye, while the solid lines are linear fits using Eq. (10) for lattice sizes $L \geqslant 64$. The extrapolated transition temperatures in the $L \to \infty$ limit, $T_c(\infty, L_{\rm min})$, are indicated by the arrows.

In addition, we can see that the $L \to \infty$ limit from each linear fit, $T_c(\infty, L_{\rm min})$, still depends on the reference lattice size $L_{\rm min}$. For this reason, we can further assume that $T_{\rm cross}(\infty, L_{\rm min})$ should follow the same scaling behavior given by Eq. (10). The result is shown in Fig. 3, from which, with an additional fit, leads to $T_c(\infty, \infty) = T_c = 0.894(1)$, a value that compares very well to $T_c = 0.8935(1)$ and

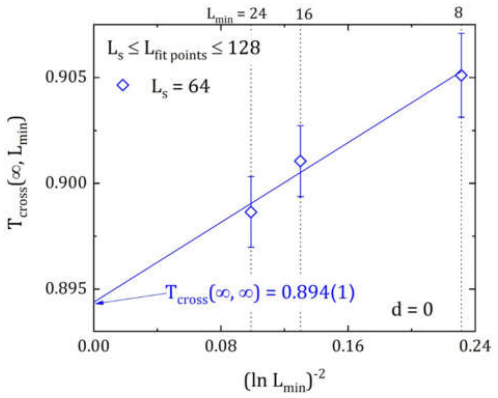

FIG. 3. Temperature of the extrapolated crossings of the Binder cumulant of the order parameter $T_{\rm cross}(\infty, L_{\rm min})$ as a function of different reference lattice sizes $L_{\rm min}$ (shown on top of the figure) when $d = 0$ (XY model) using PBC. The vertical dashed lines locate the reference lattice sizes $L_{\rm min}$ and the solid line is a linear fit using Eq. (10). L_s is the smallest lattice size considered in the fits of Fig. 2. The extrapolated transition temperature is indicated by the arrow.

TABLE I. BKT transition temperature $T_c(d)$ and the ratio $T_c(d)/\sqrt{1+d^2}$ for some values of the DM interaction d. In the last column we have some results from the literature. The last line gives the average of $T_c(d)/\sqrt{1+d^2} \equiv \overline{T}(0)$ for all values of d (including $d \to \infty$).

d	$T_c(d)$	$T_c(d)/\sqrt{1+d^2}$	$T_c(d)$ (literature)
0	0.894(1)	0.894(1)	0.8935(1) [26]
			0.8935(5) [27]
0.05	0.902(1)	0.901(1)	
0.25	0.930(2)	0.902(2)	
0.5	0.997(3)	0.892(3)	1.013(4) [14]
0.75	1.120(1)	0.896(1)	
1	1.268(2)	0.897(1)	1.292(6) [14]
1.25	1.4491(2)	0.9053(1)	
1.5	1.6203(4)	0.8988(2)	
$d \to \infty$		0.897(1)	
	$\overline{T}(0)$	0.898(4)	

$T_c = 0.8935(5)$ obtained in Refs. [26] and [27], respectively. These values are also listed in Table I where $T_c \equiv T_c(0)$.

Following the same procedure as above we can compute the transition temperature for other values of the DM interaction. As an example, Figs. 4 show the results for $d = 0.5$ using FBC and $d = 1$ using PBC. Since for $d = 1$ we have $\phi = \pi/4$, according to Eq. (6 c), the finite lattices must be multiples of 8 in order to keep the commensurability with the spin configurations, hence allowing use of PBC. As for the case of the pure XY model, $d = 0$, we can see that the scaling regime in these two examples has been only reached for the largest lattices. In fact, this is the general trend for all values $d > 0$.

The results of $T_c(\infty, L_{\min})$ from Fig. 4, as a function of $(\ln L_{\min})^{-2}$, are shown in Fig. 5. The additional extrapolation can still improve the estimate of the BKT temperature T_c slightly.

Table I gives the BKT transition temperature $T_c(d)$ so obtained for some additional values of the DM interaction

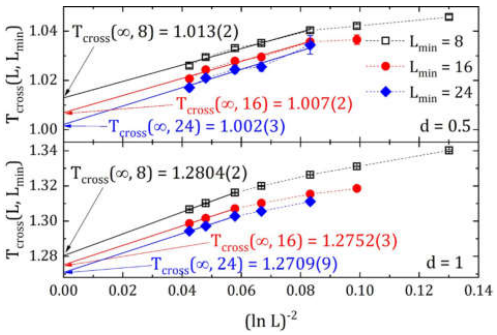

FIG. 4. Same as Fig. 2 for $d = 0.5$ using FBC (upper panel) and $d = 1$ using PBC (lower panel). The extrapolated transition temperatures are also indicated in the figures for the three reference lattice sizes.

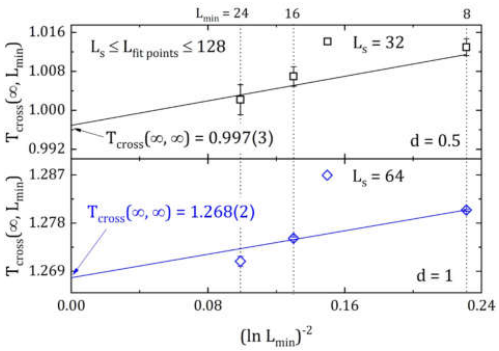

FIG. 5. Same as Fig. 3 for $d = 0.5$ using FBC (upper panel) and $d = 1$ using PBC (lower panel). L_s is the smallest lattice size considered in the fits. The extrapolated transition temperatures are also indicated for the three reference lattice sizes.

d together with some available values previously obtained from the literature [14,26,27]. Note that the transition temperatures for $d = 0.5$ and $d = 1$ are comparable to the previous estimates from Ref. [14]. However, the present ones are expected to be more accurate due to the greater statistics obtained from the simulations. We also note that the BKT transition temperatures from Ref. [14] are higher than the present ones. This is a consequence of the results in [14] being obtained using all lattice sizes and, accordingly, resulting in a smaller slope for the data extrapolation.

In Table I we also find the transition temperature for a smaller value of d namely $d = 0.05$, in order to seek whether the transition temperature starts first decreasing as d increases from zero before having a positive slope for higher values of d, as has been reported in Refs. [28,29] for the square and triangular lattices, respectively. We can see that the present result for $d = 0.05$ indeed increases and $T_c(d)$ has a monotonic behavior for larger values of the DM interaction. The decreased value of T_c for small d obtained in Refs. [28,29] could be related to the use of PBC instead of FBC, as in our approach. The expected behavior of the transition temperature as d increases will be better elucidated in the following subsection.

B. Transition temperature as a function of the DM interaction

The corresponding phase diagram of the model in the DM interaction d versus the BKT transition temperature $T_c(d)$ plane, using the values from Table I, is shown in the upper inset of Fig. 6. Note that as $d \to \infty$ the shift angle goes to $\phi \to \pi/2$ and the transition frontier becomes a straight line. Thus, taking Eq. (2) and considering $\phi = \pi/2$, we can perform an extra simulation to obtain an effective transition temperature $T_{\text{eff}} = T_c(d)/d$. This result gives, in fact, the asymptotic slope of the transition line as $d \to \infty$. Interestingly enough, the result is, within the error bars, the same as the transition temperature of the pure XY model (see Table I).

To better understand this behavior, and motivated by the definition of the order parameter in Eq. (7), we consider the

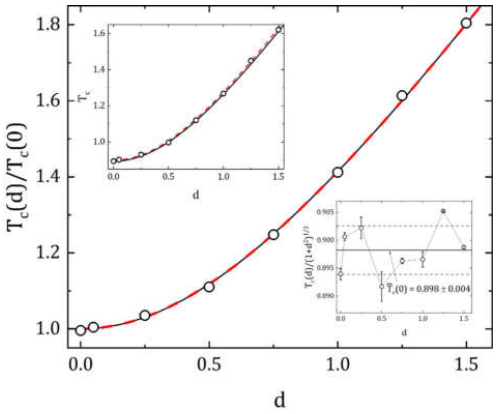

FIG. 6. *Main curve.* Phase diagram in the DM interaction d versus the reduced transition temperature $T_c(d)/T_c(0)$ plane. The circles are the results from Table I with $T_c(0) = 0.898(4)$. The solid line is the function $\sqrt{1+d^2}$ and the dashed line a fit with $\sqrt{r+d^2}$ with r given in the text (both lines are almost coincident to each other in the scale of the figure). *Upper inset.* $T_c(d)$ versus d where the solid line comes from Eq. (13) with $T_c(0) = 0.894(1)$ and the dashed line is the hyperbola using Eq. (14) with the parameters in the text. *Bottom inset.* Values of $T_c(d)/\sqrt{1+d^2}$ from the third column in Table I as a function of d. The solid line locates the mean value and the dashed lines the error bars.

following Hamiltonian:

$$\mathcal{H} = -J(d) \sum_{\langle ij \rangle} \cos[\tilde{\theta}_i(d) - \tilde{\theta}_j(d)], \tag{11}$$

where

$$\begin{aligned} \tilde{\theta}_i(d) &= \theta_i - (x_i + y_i)\phi(d), \\ \tilde{\theta}_j(d) &= \theta_j - (x_j + y_j)\phi(d). \end{aligned} \tag{12}$$

Since j is a nearest neighbor of i, one has always $(x_i + y_i) - (x_j + y_j) = 1$ and $\tilde{\theta}_i(d) - \tilde{\theta}_j(d) = \theta_i - \theta_j - \phi(d)$. This means that Hamiltonian (11) above is equivalent to Hamiltonian (2). From (11) the transition temperature is thus given by

$$T_c(d) = T_c(0)\sqrt{1+d^2}. \tag{13}$$

The above equation gives the exact transition line of the XY model with DM interaction. It is the equation of a hyperbola, which is symmetric regarding d, as it should be. This is the same result previously obtained for the one-dimensional version of the model [15].

From the above equation, it is also clear that the ratio $T_c(d)/\sqrt{1+d^2}$ is a constant, equivalent to the BKT transition of the pure model. The third column on Table I and the corresponding data in the bottom inset in Fig. 6 show this trend. The mean value $\overline{T}(0) = 0.898(4)$ is also quite comparable to the $T_c(0)$ obtained in the previous subsection and from values in the literature.

On the other hand, the ratio $T_c(d)/T_c(0) = \sqrt{1+d^2}$ is the equation of a rectangular hyperbola with equal semiaxis. Figure 6 also shows $T_c(d)/T_c(0)$, with $T_c(0) = \overline{T}(0) = 0.898(4)$, plotted together with the function $\sqrt{1+d^2}$ (solid line) and a fit with $\sqrt{r+d^2}$, where r is a fitting parameter (dashed line). In both cases one gets a quite nice agreement with the simulations and the value $r = 1.000(2)$ very close to the expected value $r = 1$.

The solid line in the upper inset of Fig. 6 is obtained from Eq. (13) with $T_c(0) = 0.894(1)$ and the dashed line is a fit of the simulation results with the hyperbole function

$$T_c(d) = T^*\sqrt{r+d^2}, \tag{14}$$

where T^* and r are the fitting parameters. Again, in both cases, a good agreement has been achieved with the simulation results, and the fitting parameters $T^* = 0.906(4)$ and $r = 0.99(1)$ are also comparable to the expected ones.

C. BKT transition and critical exponent η for $T < T_c$

We expect the transition, for any value of d, to remain of BKT type for temperatures $T < T_c$, since the transformed Hamiltonian (2) is, in essence, just another XY model with renormalized exchange interaction (although, as we shall see below in Sec. IV D, the low temperature spin configurations seem to have lower symmetry than that of the two-dimensional XY model and, as a consequence, misleadingly suggest a conventional phase transition). For the particular example of the pure model shown in the top panel of Fig. 1, one can see that the lattice sizes are still a little too small to fully reflect this behavior, because the cumulants are not all the same for temperatures lower than the crossing points. This is shown more clearly in the bottom panel of Fig. 1. This same tendency is also seen for other values of the DM interaction. For this reason, in order to confirm the BKT transition at lower temperatures we have studied the order parameter m, defined in Eq. (7), in conjunction with its scaling behavior (8). As an example, we have chosen the value $d = 0.5$ with FBC, and the results of the log-log plot of m, as a function of the lattice size L, are shown in Fig. 7 for different temperatures, slightly above and below T_c. For lower temperatures, in this case for $T \lessapprox 1.0$, all the data are along straight lines whose slopes decrease as T decreases. For higher temperatures, the behavior of m starts to deviate from straight lines signifying that the scaling regime of Eq. (8) is no longer valid and the system has been driven above the BKT transition. The wider dashed line in Fig. 7 represents the threshold of the transition exponent $\eta = 1/4$.

From the slopes of the data in Fig. 7 (and some additional ones not shown in that figure for still lower temperatures), we can compute the corresponding spin-spin correlation function critical exponent η. The results, so obtained, are shown in Fig. 8 as a function of the temperature T. It is clear from this figure that the transition is indeed of BKT type and the exponent $\eta \to 0$ as the temperature $T \to 0$, as expected. Some selected values of the exponents of Fig. 8 are displayed in Table II. Although there are some oscillations in the η values as the temperature is changed close to $T \approx 1$, we can roughly estimate the BKT transition temperature as $T_c = 1.009(9)$, a

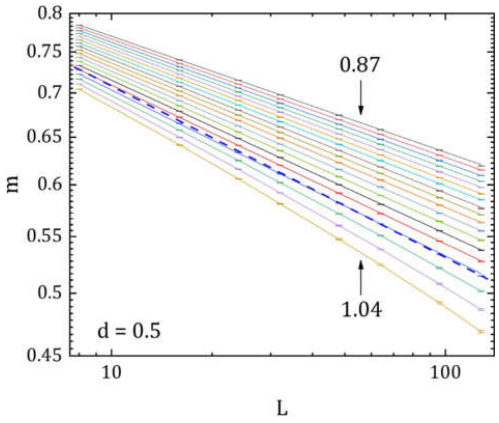

FIG. 7. Log-log plot of the order parameter m as a function of the lattice size L for different values of the temperature T for $d = 0.5$. From the lower temperature 0.87 to the higher temperature 1.04, all the steps are 0.01. The results come from histogram reweighting of data taken at temperatures $T = 0.9$, 0.97, and 1. The wider dashed straight line corresponds to the slope that gives $\eta = 1/4$. The lines for $T \leqslant 1$ are linear fits to the data, while for $T > 1$ they are just guides to the eyes.

value which is quite consistent with the transition temperature $T_c = 0.997(3)$ given in Table I. The results are similar for other values of the DM interaction d.

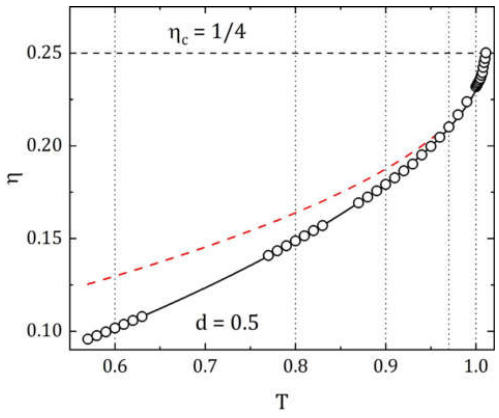

FIG. 8. Spin-spin correlation function critical exponent η as a function of the temperature T for $d = 0.5$. The vertical dotted lines locate the temperature at which the data were taken for constructing the histograms and the horizontal dotted line is the threshold of the critical exponent $\eta_c = 1/4$. The full line is a fit according to Eq. (15) with the parameters given in the text. The dashed line is a fit with only the two first terms of Eq. (15) and considering only data for $T > 0.97$.

TABLE II. Spin-spin correlation function critical exponent η for some values of temperature T for $d = 0.5$.

T	η	T	η
1.012	0.2516(9)	0.88	0.1724(2)
1.011	0.2502(9)	0.87	0.1692(2)
1.01	0.2486(9)	0.83	0.1570(2)
1.009	0.2498(9)	0.82	0.1542(2)
1	0.2318(4)	0.81	0.1514(2)
0.99	0.2238(4)	0.8	0.1488(2)
0.98	0.2168(4)	0.79	0.1460(2)
0.97	0.2102(2)	0.78	0.1434(2)
0.96	0.2046(2)	0.77	0.1408(2)
0.95	0.1996(2)	0.63	0.1068(2)
0.94	0.1952(4)	0.62	0.1058(2)
0.93	0.1902(2)	0.61	0.1038(2)
0.92	0.1866(2)	0.6	0.1016(2)
0.91	0.1828(2)	0.59	0.0996(2)
0.9	0.1792(2)	0.58	0.0976(2)
0.89	0.1756(4)	0.57	0.0956(2)

The data in Fig. 8 can be further analyzed by considering a temperature dependence of η as

$$\eta(T) = \frac{1}{4} - C\left(1 - \frac{T}{T_c}\right)^{1/2} + C'\left(1 - \frac{T}{T_c}\right) + C''\left(1 - \frac{T}{T_c}\right)^{3/2}, \quad (15)$$

where C, C', and C'' are fitting parameters and we use $T_c = 1.011$. The first two terms in (15) come from Refs. [30,31], where close to the transition temperature T_c the leading behavior is expected to have a square-root singularity. A fit with only those two terms, close to the transition point [fitting the data for $T > 0.97$ with $C = 0.189(3)$ and extrapolating to $T < 0.97$], is shown by the dashed line in Fig. 8. Although a good agreement has been obtained close to T_c, the fitted curve is far from the simulation results in an extended region of lower temperatures. On the other hand, by considering higher order contributions, as explicitly given in Eq. (15), one can see a quite good agreement, in the entire temperature range, with fit parameters $C = 0.179(3)$, $C' = -0.12(1)$, and $C'' = 0.06(1)$ (shown by the solid line in Fig. 8). In addition, with these parameters we have $\eta(0) = 0.01(1)$ and the slope at $T = 0$ $d\eta(T)/dT|_{T\to 0} = 0.12(2)$, which should be compared to the exact $\eta(0) = 0$ and $d\eta(T)/dT|_{T\to 0} = 1/2\pi = 0.169\ldots$ from the spin-wave phase [30,31].

D. Low temperature phase configurations

It is interesting to see the topology of the spin arrangements as the present BKT transition is passed through. As discussed above, at zero temperature the system orders with neighboring spins having shift angles ϕ. However, as the temperature increases, there are fluctuations in these neighboring orientations. Figure 9 depicts the corresponding spin configuration for $d = 0.5$ with FBC and lattice size $L = 48$ at three different values of temperature. In the top panels we show the spin configurations and in the bottom panels respective color

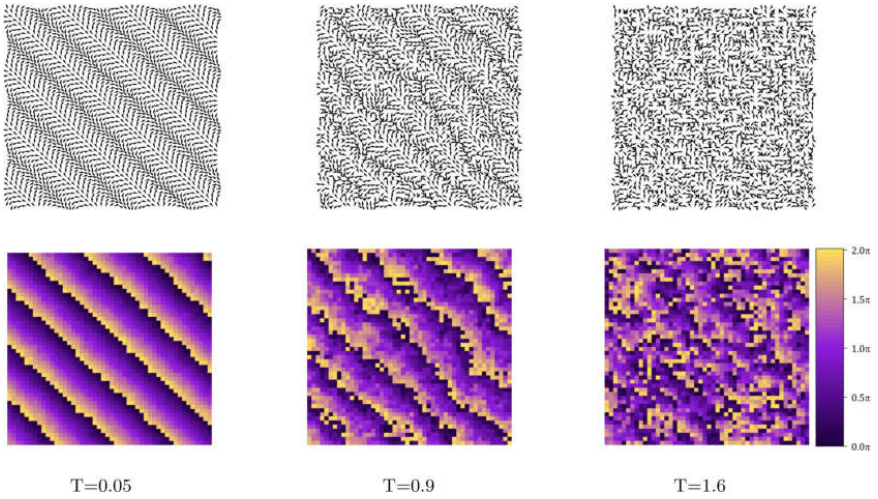

FIG. 9. Typical spin configurations given by the arrows (top panels) and color gradient of the spin orientation angle in radians (bottom panels) for $d = 0.5$ and lattice size $L = 48$ with FBC. Low temperature in the two left panels, just below the BKT transition temperature in the two middle panels, and high temperature in the two right panels.

gradients for the spin angle in radians. The striped ordering of the spins is, perhaps, better seen in the color gradient structure of the bottom panels: at low temperatures (left panels) the order is well defined; just below the BKT transition temperature (middle panels) the order still persists with larger fluctuations; and, eventually, the disordered state is achieved for higher temperatures (as depicted in the right panels).

The strip arrangement, due to the DM interaction, in some sense seems to cover up the topological structure of vortices in these systems and one might falsely expect that the incommensurate chiral order leads to a phase transition to a lower symmetry phase than that of the two-dimensional XY model and hence to a conventional phase transition. However, this is indeed not the case, because we can invert the spins by the angle ϕ and obtain similar configurations of the pure XY model. As an example, Fig. 10 shows the spin configurations, together with the location of the vortex-antivortex pairs, for $d = 0.5$. The top panels correspond to a temperature just below the transition temperature and the bottom panels to a temperature above the transition. The left panels show the actual configurations and the right panels the configurations with reverted spins. The dots and stars locate the vortex-antivortex cores. We can see that the vortex-antivortex pairs are still present even in the actual configuration of the spins due to the DM interaction.

E. FBC versus PBC and incommensurate shift angle distribution

For DM interactions where the lattice sizes become incommensurate with the spin orientations, the FBC have provided more reliable results than the usual PBC. Although in the previous results for $d = 0.5$ the FBC have been implemented in the same finite lattices used with PBC for commensurate values of d, one can as well investigate the behavior for the *optimal* sizes using Eq. (6c). For instance, for $d = 0.5$ we have $\phi = 0.4636\ldots$ rad and $L = 13.5516\ldots$, meaning that one can choose $L = 14, 28, 42, \ldots$ instead of multiples of

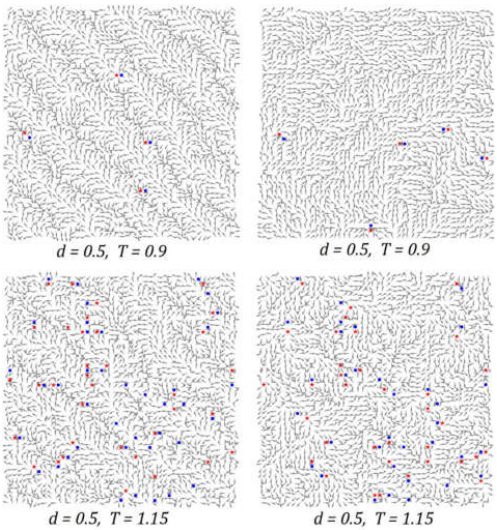

FIG. 10. Spin configurations for $d = 0.5$, just below the transition temperature in the top panels and just above the transition temperature in the bottom panels. The left panels show the actual configurations and the right panels the configurations with reverted spins. The dots and stars locate the vortex-antivortex pairs.

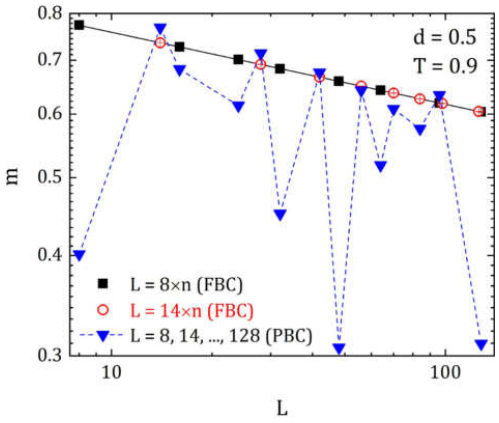

FIG. 11. Log-log plot of the order parameter m as a function of the lattice size L for $d = 0.5$ and $T = 0.9$. The squares correspond to lattice sizes that are multiples of 8 with $n \leqslant 16$, while the circles are optimal sizes which are multiples of 14 with $n \leqslant 9$. The triangles are data obtained by considering all lattices with PBC. The solid line is a fit to the scaling function given by Eq. (8) using only the results obtained from FBC. The dashed line is just a guide to the eyes.

$L = 8$ as before. Figure 11 depicts the log-log plot of the order parameter m as a function of lattice sizes L considering both choices. With the data obtained from FBC, the critical exponent is given by $\eta = 0.08954(4)$ and is comparable to the value $\eta = 0.0896(1)$ obtained by using only lattice sizes that are multiples of 8. It is then clear that, as soon as one uses FBC, the sizes of lattices are not so important for getting the transition properties of the model.

Figure 11 also shows the results for all considered lattices using PBC. We can clearly see that most of the values fall either far below or above the fit obtained using FBC. It is also interesting that even for the "optimal" lattice sizes, with PBC, the results are still rather far from the fit obtained by using FBC.

It should be stressed here that, as in the Ising model [32], different types of boundary conditions influence the universal value of the fourth-order cumulant U_4^* in the thermodynamic limit (although the transition temperature is not affected by them). In this case, for $d = 0$, we estimate $U_4^* = 0.6599(3)$ with PBC and $U_4^* = 0.6468(1)$ with FBC.

The use of optimal lattice sizes with FBC in the incommensurate case has an important effect on the probability distribution of the shift angle Δ that results from the simulation.

The behavior of such probability distributions (which, to our knowledge, has not been previously reported in the literature) should be quite useful when treating other incommensurate systems. Figure 12 show the shift angle probability distribution $P^*(\Delta) = P(\Delta)/P(\langle\Delta\rangle)$ for several values of temperature T for $d = 0.5$ and two different lattice sizes, namely $L = 48$ and $L = 41$. In order to have a better visualization, in each case the actual probability $P(\Delta)$ has been divided by the computed probability $P(\langle\Delta\rangle)$ at the mean value $\langle\Delta\rangle$,

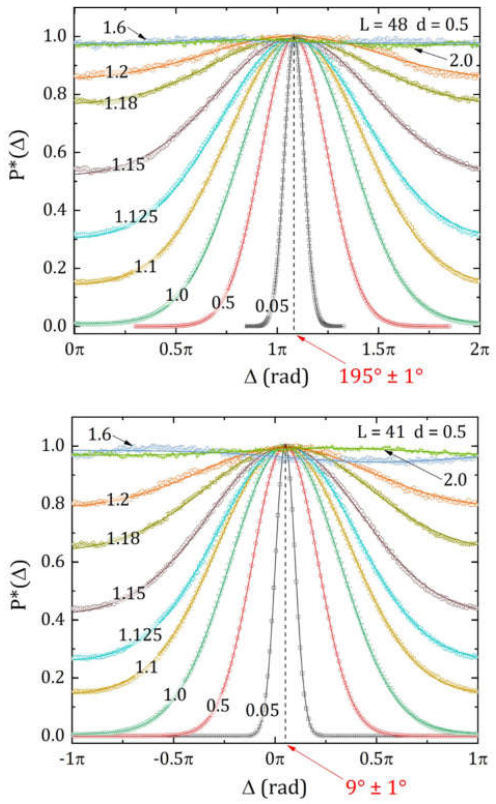

FIG. 12. Shift angle distribution $P^*(\Delta)$ as a function of Δ for $d = 0.5$ and several values of temperature. The lattice size is $L = 48$ in the upper panel and $L = 41$ in the bottom panel. The lines are Gaussian fits according to Eq. (16). The arrows indicate the mean value of the shift angle in degrees.

so one always has $P^*(\langle\Delta\rangle) = 1$. In general, all the $P^*(\Delta)$ distributions are Gaussian and have been fitted using

$$P^*(\Delta) = P_0 + A\, e^{-\frac{(\Delta-\langle\Delta\rangle)^2}{2w^2}}, \tag{16}$$

where P_0 and A are constants and w is the width of the distribution. We can see that the width w decreases as T decreases. On the other hand, as the temperature increases above the BKT temperature, the distribution flattens and reaches a constant value, meaning that in this region the phase shift is not so important due to the strong thermal fluctuations. We can clearly see that the only difference between the optimal size [here $L = 41$ obtained from Eq. (6c) with $n = 3$] and any other size will be just the mean value of the shift angle Δ, which for optimal lattice sizes will be closer to zero. It should also be stressed that if we consider FBC for commensurate lattices we obtain the same qualitative behavior above described with $\langle\Delta\rangle \approx 0$.

V. CONCLUDING REMARKS

The two-dimensional XY model with Dzyaloshinskii-Moriya (DM) interaction has been studied through extensive Monte Carlo simulations by employing a hybrid algorithm consisting of single-spin Metropolis updates and Swendsen-Wang cluster-spin updates. Single histogram reweighting techniques have been introduced to obtain the thermodynamic variables close to the Berezinskii-Kosterlitz-Thouless (BKT) transition and finite-size scaling has been used to analyze the phase transition behavior in the thermodynamic limit. Fluctuating boundary conditions (FBC) have been utilized in order to match the incommensurability between the spin structure and the finite lattice sizes due to the DM interaction. The effects of the FBC have been analyzed in detail and the BKT transition temperature, as well as the corresponding spin-spin correlation function critical exponent, has been obtained as a function of the DM interaction and temperature.

It is clear that the transition is indeed of BKT type for any value of the DM interaction, and the critical exponent η decreases from $1/4$ towards zero as the temperature decreases. The ground state is composed of strips of aligned spins that lose their conformation as the temperature approaches the BKT transition temperature.

In incommensurate cases, optimal sizes for the finite lattices, or any other lattice sizes, furnish coherent results as soon as FBC are considered. The distribution of the boundary shift angle, however, has mean values closer to zero for optimal lattices and quite different values for other sizes.

Another important result in the present work is the analytic equation for the transition temperature of the model as a function of the DM interaction, which has been verified by simulation. Besides the fact that this relation could be used in the study of quantum versions of the XY system with DM interaction, there are some important features of the present simulations that helped lead to a better understanding of the physical behavior of the model. In addition, some of these features should certainly be quite useful in studying models with other types of anisotropies, for instance, as follows.

(i) The importance of considering fluctuating boundary conditions, even to compute the exponent η, as depicted in Fig. 11.

(ii) The scaling behavior of the exponent η as a function of temperature, given by Eq. (15), which extends to the entire temperature range.

(iii) Looking at the spin configurations of Fig. 9, it is not at all obvious that the model still exhibits vortex and antivortex pairs and a BKT transition. It looks, indeed, at first sight like a conventional transition. However, we have shown that the vortices and antivortices are still present and the transition is really of BKT type.

(iv) The Gaussian distribution of the shift angle in Figs. 12 is expected to be the same for other models.

ACKNOWLEDGMENTS

This research was supported by CNPq, CAPES, and FAPEMIG (Brazilian agencies). We thank A. R. Bergeron for fruitful discussions concerning the initial simulations on this model. This study was also supported in part by resources and technical expertise from the Georgia Advanced Computing Resource Center (GACRC), a partnership between the University of Georgia's Office of the Vice President for Research and Office of the Vice President for Information Technology. We would also like to acknowledge Professor G. Weber for the invaluable assistance in the use of the Statistical Mechanics Computer Lab facilities at UFMG.

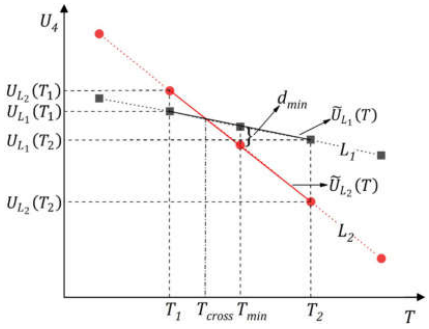

FIG. 13. Sketch of the estimate of the cumulant crossing between two diffferent lattice sizes L_1 (squares) and L_2 (circles). $d_{\min}$ is the minimum value of the magnitude of the difference of the cumulants $|U_{L2} - U_{L_1}|$ at $T_{\min}$, from which one locates neighboring temperatures T_1 and T_2. $\tilde{U}_{L_1}(T)$ is the straight line equation (full line) through points $[T_1, U_{L_1}(T_1)]$ and $[T_2, U_{L_1}(T_2)]$, while $\tilde{U}_{L_2}(T)$ is the corresponding straight line equation through points $[T_1, U_{L_2}(T_1)]$ and $[T_2, U_{L_2}(T_2)]$. T_{cross} is the temperature where the lines $\tilde{U}_{L_1}(T)$ and $\tilde{U}_{L_2}(T)$ meet.

APPENDIX

This Appendix briefly describes the method used to compute the crossing temperatures from the cumulants as well as the estimate of the corresponding errors.

Figure 13 sketches typical results for the cumulants U_{L_1} and U_{L_2} of two different lattice sizes L_1 and L_2 as a function of temperature. If $d_{\min}$ is the minimum value of the magnitude of the difference of the cumulants $|U_{L_2} - U_{L_1}|$ occurring at $T_{\min}$, we can determine its two neighboring temperatures T_1 and T_2, as shown in Fig. 13. From these points we construct the equations of straight lines $\tilde{U}_{L_1}(T)$ and $\tilde{U}_{L_2}(T)$, which meet at T_{cross} where $\tilde{U}_{L_1}(T_{\text{cross}}) = \tilde{U}_{L_2}(T_{\text{cross}})$, leading to

$$T_{\text{cross}} = T_2 - \frac{\Delta U_{T_2}}{\Delta U_{T_2} - \Delta U_{T_1}} \Delta T_{12}, \tag{A1}$$

where

$$\begin{aligned} \Delta T_{12} &= T_2 - T_1, \\ \Delta U_{T_1} &= U_{L_2}(T_1) - U_{L_1}(T_1), \\ \Delta U_{T_2} &= U_{L_2}(T_2) - U_{L_1}(T_2). \end{aligned} \tag{A2}$$

Since T_1, T_2, and ΔT_{12} are fixed in a particular data set, the error in crossing temperature δT_{cross} comes basically from the simulations and the histogram reweighting on the other quantities appearing in Eqs. (A1) and (A2), in this case the

corresponding cumulants at different temperatures. Accordingly, one has [33]

$$\delta T_{\text{cross}} = \sqrt{\sum_{i=1}^{2}\sum_{j=1}^{2}\left[\frac{\partial T_{\text{cross}}}{\partial U_{L_i}(T_j)}\right]^2 [\delta U_{L_i}(T_j)]^2}, \tag{A3}$$

where the partial derivatives are taken from Eqs. (A1) and (A2) and $\delta U_{L_i}(T_j)$ is the uncertainty coming from the simulation data.

A more compact form of the above expression can be given by

$$\delta T_{\text{cross}} = 2C\Delta T, \tag{A4}$$

where ΔT is the chosen resolution of the temperature interval where the histograms are taken (in our case $\Delta T = 0.001$) and C specifies the contributions from the cumulants and their uncertainties for the lattice sizes L_1 and L_2 at temperatures T_1 and T_2. More explicitly, one has

$$C = \frac{\sqrt{C_1 + C_2}}{\left(\Delta U_{T_2} - \Delta U_{T_1}\right)^2}, \tag{A5}$$

with

$$C_1 = \left\{\left[\delta U_{L_1}(T_1)\right]^2 + \left[\delta U_{L_2}(T_1)\right]^2\right\}(\Delta U_{T_2})^2,$$
$$C_1 = \left\{\left[\delta U_{L_1}(T_2)\right]^2 + \left[\delta U_{L_2}(T_2)\right]^2\right\}(\Delta U_{T_1})^2. \tag{A6}$$

Estimates of the error of the cumulants at different temperatures are obtained by dividing the data into bins and computing the cumulants for each bin using the respective histograms. It is then possible to estimate the mean value and the error of the cumulants at any temperature.

[1] T. Matsubara and H. Matsuda, Prog. Theor. Phys. **16**, 569 (1956).
[2] T. Ohta and D. Jasnow, Phys. Rev. B **20**, 139 (1979).
[3] D. J. Resnick, J. C. Garland, J. T. Boyd, S. Shoemaker, and R. S. Newrock, Phys. Rev. Lett. **47**, 1542 (1981).
[4] V. L. Berezinskii, Sov. Phys. JETP **32**, 493 (1971).
[5] J. M. Kosterlitz and D. J. Thouless, J. Phys. C: Solid State Phys. **6**, 1181 (1973).
[6] J. M. Kosterlitz, J. Phys. C: Solid State Phys. **7**, 1046 (1974).
[7] I. Dzyaloshinsky, J. Phys. Chem. Solids **4**, 241 (1958).
[8] T. Moriya, Phys. Rev. Lett. **4**, 228 (1960); Phys. Rev. **120**, 91 (1960).
[9] D. Coffey, K. S. Bedell, and S. A. Trugman, Phys. Rev. B **42**, 6509 (1990).
[10] M. Uchida, Y. Onose, Y. Matsui *et al.*, Science **311**, 359 (2006).
[11] M. Bode, M. Heide, K. V. Bergmann *et al.*, Nature **447**, 190 (2007).
[12] P. Ferriani, K. von Bergmann, E. Y. Vedmedenko, S. Heinze, M. Bode, M. Heide, G. Bihlmayer, S. Blugel, and R. Wiesendanger, Phys. Rev. Lett. **101**, 027201 (2008).
[13] S. V. Grigoriev, Yu. O. Chetverikov, D. Lott, and A. Schreyer, Phys. Rev. Lett. **100**, 197203 (2008).
[14] H. Liu, J. A. Plascak, and D. P. Landau, Phys. Rev. E **97**, 052118 (2018).
[15] F. C. Alcaraz and W. F. Wreszinski, J. Stat. Phys. **58**, 45 (1990).
[16] P. Olsson, Phys. Rev. Lett. **73**, 3339 (1994).
[17] N. Metropolis, A. W. Rosenbluth, M. N. Rosenbluth *et al.*, J. Chem. Phys. **21**, 1087 (1953).
[18] R. H. Swendsen and J. S. Wang, Phys. Rev. Lett. **58**, 86 (1987).
[19] M. S. S. Challa and D. P. Landau, Phys. Rev. B **33**, 437 (1986).
[20] E. Rastelli, S. Regina, and A. Tassi, Phys. Rev. B **69**, 174407 (2004); **70**, 174447 (2004).
[21] M. E. Fisher, in *Proceeding of the International Summer School "Enrico Fermi" 1970, Course 51, Varenna, Italy*, edited by M. S. Green (Academic Press, New York, 1971).
[22] D. P. Landau and K. Binder, *A Guide to Monte Carlo Simulation in Statistical Physics*, 5th ed. (Cambridge University Press, Cambridge, UK, 2021).
[23] K. Binder, Z. Phys. B: Condens. Matt. **43**, 119 (1981).
[24] S. T. Bramwell and P. C. W. Holdsworth, J. Phys.: Condens. Matter **5**, L53 (1993).
[25] D. Venus, Phys. Rev. B **105**, 235440 (2022).
[26] Y.-D. Hsieh, Y.-J. Kao, and A. W. Sandvik, J. Stat. Mech. (2013) P09001.
[27] P. H. Nguyen and M. Boninsegni, Appl. Sci. **11**, 4931 (2021).
[28] S. Yun-Zhou, L. Hui-Ping, and Y. Lin, Commun. Theor. Phys. (Beijing, China) **46**, 663 (2006).
[29] Y.-Z. Sun, L. Yi, and J.-S. Wang, Commun. Comput. Phys. **11**, 1169 (2012).
[30] J. M. Kosterlitz and D. J. Thouless, in *Progress in Low Temperature Physics*, edited by D. F. Brewer (Elsevier, Amsterdam, 1978), Chap. 5.
[31] R. Gupta and C. F. Baillie, Phys. Rev. B **45**, 2883 (1992).
[32] W. Selke, Eur. Phys. J. B **51**, 223 (2006).
[33] Evaluation of measurement data—Guide to the expression of uncertainty in measurement, https://www.bipm.org/documents/20126/2071204/JCGM_100_2008_E.pdf/cb0ef43f-baa5-11cf-3f85-4dcd86f77bd6.

PHYSICAL REVIEW E **109**, 064113 (2024)

Three-dimensional Heisenberg model with Dzyaloshinskii-Moriya interaction: A Monte Carlo study

G. Albuquerque Silva,[1] A. R. Bergeron,[2] J. A. Plascak,[1,2,3] and D. P. Landau[2]
[1]*Departamento de Física, Instituto de Ciências Exatas, Universidade Federal de Minas Gerais, C.P. 702, 30123-970 Belo Horizonte MG, Brazil*
[2]*Center for Simulational Physics, The University of Georgia, Athens, Georgia 30602 USA*
[3]*Universidade Federal da Paraíba, Centro de Ciências Exatas e da Natureza–Campus I, Departamento de Física–CCEN Cidade Universitária 58051-970, João Pessoa PB, Brazil*

(Received 28 December 2023; accepted 21 May 2024; published 6 June 2024)

The three-dimensional classical Heisenberg model on a simple cubic lattice with Dzyaloshinskii-Moriya (DM) interactions between nearest-neighbors in all directions has been studied using Monte Carlo simulations. The Metropolis algorithm, combined with single histogram reweighting techniques and finite-size scaling analyses, has been used to obtain the thermodynamic behavior of the system in the thermodynamic limit. Simulations were performed with the same set of interaction parameters for both *shifted* boundary conditions (SBC) and *fluctuating* boundary conditions (FBC). Because of an incommensurability caused by the DM interaction, the SBC incorporated a fixed shift angle at the boundary which varies as a function of the DM interaction and lattice size. This SBC method decreases the simulation time significantly, but the distribution of states is somewhat different than that obtained with FBC. The ground state for nonzero DM interaction is a spiral configuration where the spins are restricted to lie in planes perpendicular to the DM vector. We found that this spiral configuration undergoes a conventional second-order phase transition into a disordered, paramagnetic state with the transition temperature being a function of the magnitude of the DM interaction. The limiting case with only DM interaction in the model has also been considered. The critical exponent ν, the critical exponent ratios α/ν, β/ν, γ/ν, as well as the critical temperature T_c and fourth-order cumulant of the order parameter U_4^* at T_c have been estimated for different magnitudes of DM interaction. The critical exponents and cumulants at the transition are different from those for the three-dimensional Heisenberg model, but the ratios α/ν, β/ν, γ/ν, U_4^*/ν are the same, implying that weak universality is valid for all values of DM interaction. Structure factor calculations for particular cases have been performed considering SBC and FBC in the simulations with different lattice sizes at the critical temperatures.

DOI: 10.1103/PhysRevE.109.064113

I. INTRODUCTION

The phenomenon giving rise to a spontaneous magnetization in the absence of an external magnetic field in ferromagnetic (FM) materials below the critical temperature was first elucidated by Heisenberg [1], who introduced a symmetric "exchange interaction" or, as he named it, "exchange term." In this way, not only ferromagnetic but antiferromagnetic (AFM) materials could be successfully analyzed based on models which incorporate an exchange interaction. A good example is the Heisenberg model itself. It was later noticed that a type of "weak" ferromagnetism occurs in certain antiferromagnetic materials that could not be explained only on the basis of the Heisenberg exchange interaction [2,3]. The agent responsible for this effect was clarified by Dzyaloshinskii [4] and Moriya [5] and is now called the Dzyaloshinskii-Moriya (DM) interaction.

It is interesting to note that, besides the antiferromagnetic materials exhibiting weak ferromagnetism, the DM interaction can also appear due to symmetry breaking at a surface of some magnetic materials [6], crystals with a chiral magnetic structure [7–10], and in magnetic thin films in multilayers [11–14]. In these cases, different magnetic phases than the usual FM phase can emerge, such as helical, conical, solitons, spiral phases, and even phases with more exotic spin textures like skyrmions [14,15]. Because of the importance of DM interactions to the formation of such novel and compelling spin textures, many experimental studies of systems with DM coupling have focused on these magnetic structural properties [16]. In addition, multiferroics (see, e.g., Ref. [17]), for which DM interaction plays a significant role, also exhibit other interesting behavior, e.g., ferroelectricity, which has captured the interest of experimentalists. The specific heat has been measured [18] for the ferromagnet Mn_5Ge_3, which orders at room temperature, but the resolution was insufficient to extract critical exponents of the respective second-order phase transition.

The thermodynamic properties, the magnetic structures, and the magnetic excitations present in these systems containing DM interaction have been studied by theoretical approaches as well as by Monte Carlo (MC) simulations (see, e.g., Refs. [19–24] and [25–30], respectively). However, in some of these investigations the important question of the weak universality class of the models has not been completely addressed when one regards the effect of the DM interaction.

In previous works [31,32], the two-dimensional XY model with DM interactions has been studied using MC simulations and finite-size scaling. The phase diagram in the temperature

 ©2024 American Physical Society

versus DM interaction plane, as well as the respective critical exponents were obtained, and it was noticed that the modulation of the spin vectors with position depended upon the value of the DM interaction. As a result, incommensurability may appear when arbitrary values of the DM interaction are considered in the simulations. In this case, fluctuating boundary conditions (FBC) have been implemented in order to properly accommodate incommensurabilities.

Here we have adopted the same procedure used for the two-dimensional XY model to analyze the Heisenberg model with DM interaction in three dimensions. As stated by Moriya [5], DM interactions occur in crystals of low symmetry, like noncentrosymmetric crystals [6]. Despite some special details that occur in real materials, e.g., intrinsic interaction anisotropies and crystal asymmetries, we have considered a simpler model consisting of the traditional isotropic exchange Heisenberg Hamiltonian with DM interaction defined in a simple cubic lattice. This model has some similarity with the pyrochlore lattice with DM interactions [33] (in spite of the difference of lattice symmetry, which is hexagonal in the later one [34]). Besides that, several chiral helimagnets, among which MnSi and $CrNb_3S_6$, have been studied on the basis of simpler models like the one considered here [25–30], having subtle differences with respect to the way that DM vector interactions are defined between the spins in the lattice and/or by the addition of extra interaction terms in the model.

The plan of the paper is as follows: In the next section, the model and effective Hamiltonian are presented. Section III is devoted to the methodology, including the Monte Carlo simulation details, boundary conditions, thermodynamic quantities of interest, and finite-size scaling analyses. The results are presented in Sec. IV and concluding remarks are made in the final section.

II. MODEL

The Hamiltonian we have considered can be written as

$$\mathcal{H} = -J \sum_{\langle i,j \rangle} \mathbf{S}_i \cdot \mathbf{S}_j - \sum_{\langle i,j \rangle} \mathbf{D} \cdot (\mathbf{S}_i \times \mathbf{S}_j), \tag{1}$$

where the first sum represents the isotropic Heisenberg term with exchange interaction J, and the second sum represents the Dzyaloshinskii-Moriya term, with $\mathbf{D}$ being the DM vector interaction. $\mathbf{S}_i$ are three-dimensional classical spin vectors sitting at each site i of a simple cubic lattice with $\|\mathbf{S}_i\| = 1$. The bracket $\langle i, j \rangle$ specifies that each spin interacts with its nearest neighbors along the three directions of the lattice for both for the FM and DM interactions.

Choosing the DM vector along the positive z direction and applying the transformation proposed by Alcaraz and Wreszinski [35], we get the effective Hamiltonian

$$\mathcal{H}(d) = -J \sum_{\langle i,j \rangle} \{\sqrt{1+d^2}\cos[\varphi_i - \varphi_j - \phi(d)] \times \sin\theta_i \sin\theta_j + \cos\theta_i \cos\theta_j\}, \tag{2}$$

where $d = D/J$, D is the magnitude of the DM interaction vector, φ_i and θ_i are the angles of the spin vector $\mathbf{S}_i$ in spherical coordinates, and $\phi(d) = \tan^{-1} d$. It is worthwhile to stress, for future reference, that the Hamiltonian (2) is equivalent to an anisotropic Heisenberg model with renormalized exchange interaction in the x-y plane.

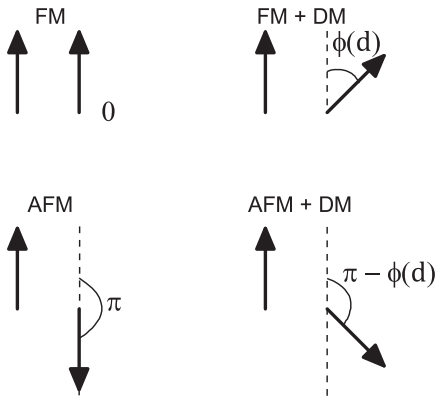

FIG. 1. A simple illustration showing the ground-state relative orientation of two nearest spin vectors according to the type of interaction between them. Top illustrations for the ferromagnetic case (FM) case, with and without Dzyaloshinskii-Moriya (DM) interactions. Bottom illustrations for the antiferromagnetic (AFM) case, with and without DM interaction. The azimuthal angular difference $\phi(d)$ of the pair of spins is indicated in each case.

It is easy to see that, in the FM ($J > 0$) ground state all the spin vectors arrange themselves in a spiral configuration where the spins are restricted to lie in planes perpendicular to the DM vector. Moreover, two adjacent spin vectors have an angular difference equal to $\phi(d)$. As depicted in the top sketches in Fig. 1, and one lattice spacing displacement implies that a $\phi(d)$ rotation of the next spin vector, causes a modulation of the x- and y- spin components along the principal lattice directions, which causes a modulation on the x- and y-spin components along the x-, y-, and z-lattice directions. In this sense, $\phi(d)$ is the pitch angle and, according to its value, the modulation length may be either commensurate or incommensurate with a finite lattice. It is this possible incommensurability that requires more subtle boundary conditions when simulating the model with DM interaction on finite lattices.

In the AFM case, i.e., $J < 0$, the ground-state configuration of the model would also be restricted to lie in planes perpendicular to the DM vector, but the spin vectors now would arrange themselves in an antiparallel way, with any spin and its nearest neighbor in the lattice having an azimuthal angular difference equal to $\pi - \phi(d)$, as it is depicted in the bottom sketches in Fig. 1. This means that one lattice spacing displacement implies in a $\pi - \phi(d)$ rotation of the next spin vector, giving rise to a modulation on the spin vectors as discussed in the above paragraph. Some attention should be paid to the signal of $\phi(d)$ in Eq. (2), which changes into $-\phi(d)$ in the cosine argument due to the ratio $d = D/J$.

This work will be focused only on the FM case, though the AFM case could be studied in a very similar approach and eventually lead to similar conclusions about the critical behavior of the antiferromagnetic model with DM interaction.

III. METHODOLOGY

A. Monte Carlo simulations

The simulations consist of running several MC steps per spin (MCS) and storing the corresponding values of energy, order parameter, etc. One MCS is defined by a sequential sweep of all the spins of the lattice using the standard Metropolis algorithm [36]. For each spin vector $\mathbf{S}_i$ having angles (θ_i, φ_i), new angles (θ_i', φ_i') are randomly chosen and accepted if the total energy becomes smaller than the total energy for the previous angles or if the Boltzmann probability of the energy difference is greater than a random number uniformly distributed between 0 and 1. If this last condition does not occur, then the spin angles remain unchanged.

Lattices with $L \times L \times L = L^3$ sites have been used in the MC simulations with the sizes raging from $L = 8$ to 56 ($L = 64$ in some cases). A typical simulation consisted of 10^5–10^6 discarded MCS (depending on L) for thermalization and measurements taken every 10 MCS within the total of 10^6 MCS after equilibration. For some finer analysis, single-histogram reweighting techniques were used with data from 300 to 800 simulations (again, depending on L), running on different processor cores and starting with different random number generator seeds. A maximum of 1.6×10^9 configurations have been generated for the lattice size $L = 56$, with histograms constructed with data coming from 8×10^7 configurations. The random number generator we have used was "ran2" in Ref. [37].

B. Boundary conditions

To check if the modulation length due to the DM interaction, measured by the parameter d, is commensurate or incommensurate with the lattice size L, we considered a shift angle $\Delta(d, L)$ in the interval $[0, 2\pi)$, given by

$$\Delta(d, L) = \text{mod}[L\phi(d), 2\pi], \tag{3}$$

where $\phi(d)$ is the pitch angle and "mod" is the modulo operation. In the case of the ground-state spin configuration at $T = 0$, if $\Delta(d, L) = 0$, then the configurations are commensurate with the lattice. Otherwise, when $\Delta(d, L)$ differs from zero, an incommensurability takes place. However, having this shift angle at hand, it is possible to compensate the azimuthal angular differences $\varphi_i - \varphi_j$, for the spins i and j along the boundary of the lattice, by choosing $\varphi_i + \Delta - \varphi_j$. If one wishes to study the AFM version of the model, then it would only be necessary to make the change $\phi(d) \to \pi - \phi(d)$ in Eq. (3).

Based on these considerations, we have defined two different boundary conditions for the simulations. One uses Δ calculated from Eq. (3), which remains fixed during the entire simulation. The other one uses a variable value of Δ which is calculated by an extra Metropolis step specially designed for the spins on the boundary of the lattice. For convenience, we will refer to the use of a constant Δ as *shifted boundary condition* (SBC) and FBC [38] when Δ is determined through an extra Metropolis sweep. For the simulations with FBC, we defined Δ_x, Δ_y, and Δ_z to be the shift angles for each direction in the lattice and they were calculated independently of each other. In this way, after one MCS with Metropolis algorithm, there is one additional step to sweep all the spins along the boundary to compute the three shift angles.

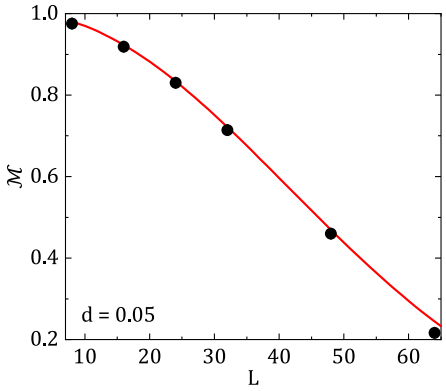

FIG. 2. Magnetization per spin $\mathcal{M}$ as a function of the lattice size L for a small value $d = 0.05$. The solid line corresponds to the theoretical result at $T = 0$, given by Eq. (4) in a simple cubic lattice. The circles are MC simulation results at a low temperature $T = 0.025$. The MC errors are smaller than the symbol sizes.

We stress here that, whenever $\Delta(d, L) = 0$, SBC becomes identical to the usual periodic boundary condition (PBC). For instance, the configurations are commensurate with the lattice sizes for (i) $d = 0$ for any value of L because $\phi = 0$, (ii) $d = 1$ for L being a multiple of 8 since $\phi = \pi/4$, and (iii) $d = \infty$ for L multiple of 4 since $\phi = \pi/2$. In all cases above SPC and PBC produce the same result. However, for $d = 0.5$, for example, a spin modulation length equal to $2\pi/\tan^{-1} 0.5 = 13.55\ldots$ lattice spacing results in an unavoidable incommensurability case for any finite lattice size.

C. Thermodynamic quantities and finite-size scaling relations

In this model, the usual magnetization per spin $\mathcal{M}$, defined as the magnitude of the vectorial sum of all spins $\mathbf{S}_i$ divided by the number of sites, $\mathcal{M} = \|\sum_{i=1}^{L^3} \mathbf{S}_i\|/L^3$, goes to zero in the thermodynamic limit as soon as $d \neq 0$. Nevertheless, for finite lattices this quantity differs from zero. At $T = 0$, where all spins are in the x-y plane, it is possible to compute $\mathcal{M}$ as a function of L and ϕ. The result is

$$\mathcal{M}(L, \phi) = \left| \frac{\sin(L\phi/2)}{L \sin(\phi/2)} \right|^3. \tag{4}$$

It is clear that $\mathcal{M}(L, \phi) \to 0$ as $L \to \infty$ for any finite ϕ. As $\phi \to 0$ one has $\mathcal{M}(L, \phi) \to 1$, as expected, because, in this case, we have $d = 0$ and the DM interaction is suppressed.

The full line in Fig. 2 gives the behavior of $\mathcal{M}$ from Eq. (4), as a function of the lattice size L, for a small pitch angle corresponding to $d = 0.05$. The circles correspond to MC results for the same value of d and for a very low temperature $T = 0.025$. Here, and in the remainder of this paper, we consider the exchange interaction $J = 1$ and the Boltzmann constant $k_B = 1$ (in other words, it simply means that we are measuring

the temperature T in convenient units of k_B/J). The agreement seen in this figure shows that $T = 0.025$ is low enough to capture the essence of the ground-state configuration.

Even when the temperature increases from such a low value, the spin vectors are still forced to closely stay in planes perpendicular to the DM vector. This can be seen from the behavior of the z-component magnetization $\mathcal{M}_z = (\sum_{i=1}^{L^3} S_i^z)/L^3$ as the temperature increases. Figure 3 shows the results from MC simulations at $d = 0.05$ and $d = 0.5$ and different lattice sizes. $\mathcal{M}_z$ fluctuates around zero with the magnitude of its fluctuation decreasing as d increases in the whole temperature range. Furthermore, $\mathcal{M}_z$ seems to tend to zero as the lattice size tends to infinity. It is also interesting to notice that the DM interaction forces the spins to stay in perpendicular planes even for smaller lattices, since the fluctuations decrease two orders of magnitude when $d = 0.5$ even for the smaller lattice $L = 8$.

Based on the foregoing considerations, it is evident that the magnetization per spin $\mathcal{M}$ cannot be used as an order parameter as soon as one has a DM interaction in the model (despite the fact that, as the temperature increases, the magnetization per spin decreases from its value at $T = 0$ for each value L and approaches zero).

We have defined a different order parameter m as

$$m = \frac{1}{L^3}\sqrt{\left\{\sum_{i=1}^{L^3}\cos[\varphi_i + (x_i + y_i + z_i)\phi]\sin\theta_i\right\}^2 + \left\{\sum_{i=1}^{L^3}\sin[\varphi_i + (x_i + y_i + z_i)\phi]\sin\theta_i\right\}^2 + \left(\sum_{i=1}^{L^3}\cos\theta_i\right)^2}. \quad (5)$$

Note that m depends not only on the spin spherical angles but also on their positions in the lattice and the pitch angle ϕ. Ultimately, the terms $(x_i + y_i + z_i)\phi$ in Eq. (5) have the effect of undoing the modulations on the spin vectors caused by the presence of the DM interaction, with $x_i, y_i, z_i \in [0, L-1]$. As a result, for any finite lattice $m = 1$ in the ground state and decreases to zero as the temperature increases, playing the perfect role of an order parameter.

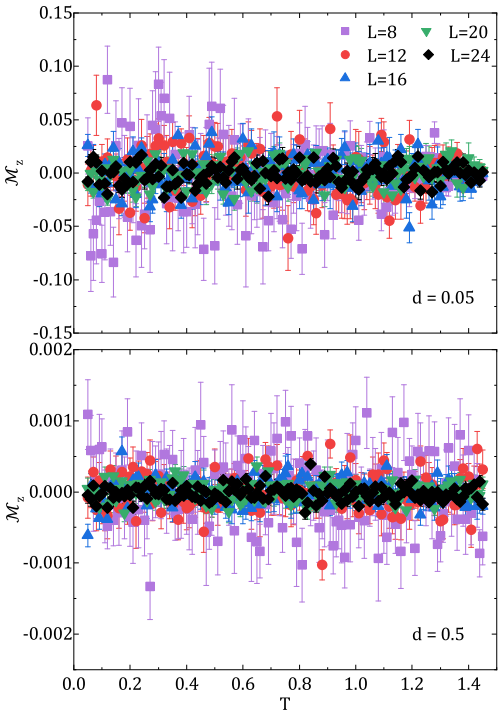

FIG. 3. MC results of the z-component magnetization per spin $\mathcal{M}_z$, as a function of the temperature T, for different lattice sizes, at $d = 0.05$ (top panel) and $d = 0.5$ (bottom panel).

A very useful quantity to compute the critical temperature is the fourth-order (Binder) cumulant of the above order parameter [39], defined in its reduced form as

$$U_4 = 1 - \frac{\langle m^4\rangle}{3\langle m^2\rangle^2}, \quad (6)$$

where the angle brackets denote the thermal average. For sufficiently large systems, this cumulant as a function of temperature should cross at the same point T_c for different values of L. T_c is thus the critical temperature and the cumulant U_4^* at T_c has a universal value. In addition, the slopes of U_4 at T_c are proportional to $L^{-1/\nu}$, where ν is the correlation length critical exponent. These properties of U_4 allow an almost unbiased estimate of T_c, U_4^* and ν [40,41].

When the finite lattices are not large enough, residual corrections to finite-size scaling (FSS) [39] make the crossing points of the cumulant U_4 suffer a systematic shift as L varies. As we shall see below, this also happens in the present model. However, if $T_{\rm cross}(L, L_s)$ is the crossing temperature of the cumulants for lattice sizes L and L_s, where L_s is fixed and taken as a reference lattice size, then the systematic deviations of this quantity can be modeled as [40,41]

$$T_{\rm cross}(L, L_s) = T_c(\infty, L_s) + \frac{B_T}{\log_{10}(L/L_s)}, \quad (7)$$

where $T_c(\infty, L_s)$ gives us an estimate of the critical temperature of the infinite system and B_T is a nonuniversal constant.

Similarly to Eq. (7), the cumulant values at $T_{\rm cross}(L, L_s)$, namely $U_4^*(L, L_s)$, can be modeled as

$$U_4^*(L, L_s) = U_4^*(\infty, L_s) + \frac{B_U}{\log_{10}(L/L_s)}, \quad (8)$$

where $U_4^*(\infty, L_s)$ provides an estimate of the cumulant for the infinite lattice and B_U is another nonuniversal constant.

Since both $T_c(\infty, L_s)$ and $U_4^*(\infty, L_s)$ could still depend on the reference lattice L_s, one eventually obtains the critical

temperature T_c and the fourth-order cumulant U_4^* in the limit $L_s \to \infty$, namely $T_c = T_c(\infty, \infty)$ and $U_4^* = U_4^*(\infty, \infty)$. In the present case, it was possible to get reasonable resolution for the cumulant crossings with $L_s = 8,\ 12,\ 16$, and 20. We have also taken $L > L_s$ for all values of L_s.

Having the critical temperature in hand, the critical exponents of the correlation length ν, order parameter β, susceptibility of the order parameter γ, and specific heat α can be computed from the finite-size scaling relations,

$$\left.\frac{dU_4(\beta_T; L)}{d\beta_T}\right|_{\beta_T=\beta_{T_c}} \approx\ U_0 L^{-1/\nu}, \tag{9}$$

$$m(T = T_c; L) \approx\ m_0 L^{-\beta/\nu}, \tag{10}$$

$$\chi_{\text{peak}}(L) \approx\ \chi_0 L^{\gamma/\nu}, \tag{11}$$

$$C_{\text{peak}}(L) \approx\ C_\infty + C_0 L^{\alpha/\nu}, \tag{12}$$

where U_0, m_0, χ_0, C_∞, and C_0 are constants. Equation (9) corresponds to the derivative of the fourth-order cumulant with respect to the variable $\beta_T = 1/k_B T$ and is taken at the critical temperature. Equation (10) is the order parameter at T_c. Equation (11) is the peak value of the order parameter susceptibility χ defined by

$$\chi = \frac{L^3[\langle m^2\rangle - \langle m\rangle^2]}{k_B T}, \tag{13}$$

and Eq. (12) is the peak value of the specific heat C given by

$$C = \frac{\langle \mathcal{H}^2\rangle - \langle \mathcal{H}\rangle^2}{L^3 k_B T^2}. \tag{14}$$

More detail about the nature of the phase transition is given by the structure factor [41], which provides information about the spin-spin correlations and the magnetic long-range ordering. This quantity is defined by the spatial Fourier transform of the time-independent pair-correlation function $\Gamma(\mathbf{r}_{jk}) = \langle \mathbf{S}_j \cdot \mathbf{S}_k\rangle - \langle \mathbf{S}_j\rangle \cdot \langle \mathbf{S}_k\rangle$ of the spin configurations in thermal equilibrium, with $\mathbf{r}_{jk} = \mathbf{r}_j - \mathbf{r}_k$ being the relative vector position of the spins at j and k sites, respectively (the lattice parameter has been normalized to unity). Accordingly, the static structure factor $\mathcal{S}(\mathbf{q})$ can be written as

$$\mathcal{S}(\mathbf{q}) = \frac{1}{L^3}\sum_{j,k} \Gamma(\mathbf{r}_{jk}) e^{i\mathbf{q}\cdot\mathbf{r}_{jk}}, \tag{15}$$

where $\mathbf{q}$ is the wave vector and the double summation runs over all the spins in the lattice. This structure factor is also very useful to investigate the magnetic structures emerging from complex arrangements of the spins, as well as distinguishing different magnetic phases [42,43].

D. More on simulations

The simulations have been done following two different approaches for different values of d and shifted and fluctuating boundary conditions.

In the first approach, data generated by sets of extensive MC simulations as described above (with an estimated CPU time of the order 7×10^5 core-hours), together with the single histogram reweighting, have been used to accurately estimate the critical temperature T_c and the value of the fourth-order cumulant U_4^*. For this purpose, we have used Eqs. (5)–(8) with $L \leqslant 56$. The critical exponent ν and the ratio β/ν have been estimated through the FSS relations given by Eqs. (9) and (10).

In the second approach, with less computational effort (an estimated 10^5 core-hours), the susceptibility of the order parameter and specific heat curves as a function of T have been directly obtained from single MC simulations, and the ratios γ/ν and α/ν have been estimated from the FSS relations given by Eqs. (11) and (12). In this case we have also included a larger lattice $L = 64$. Additional estimates of T_c, using the FSS of the temperatures where the susceptibility of the order parameter and specific heat take place, have been obtained as well. The computation of the structure factor $\mathcal{S}(\mathbf{q})$ has been done following this second approach for lattice sizes $L \leqslant 24$ (CPU time of only about 2000 core-hours in this case).

IV. RESULTS

In this section, we will focus on the results for three particular regimes of d. The first one is when $d = 0$ which is the well-known Heisenberg model that has no spin modulation but only FM order at low temperatures. In this case, comparison of the present results with previous simulations can also be made. As an intermediate regime, we consider $d = 0.5$, having a spin modulation length that results in an unavoidable incommensurability for any finite lattice size. In some cases, $d = 1$ will also be considered, where commensurate lattices are obtained when L is a multiple of 8.

The third regime is when d tends to infinity and the DM interaction dominates, i.e., a three-dimensional "DM model" containing only DM interactions. This regime will be referred to as $d = \infty$, where the second term involving cosines in Eq. (2) can be neglected. This case results in the shortest possible spin modulation length $\phi = \pi/2$ being equal to four lattice spacings. The incommensurability can thus be circumvented by choosing lattice sizes $L = 4n$, with $n = 1, 2, \ldots$.

In the $d = \infty$ limit, where the cosines term can be neglected, the simulations provide a transition where

$$[\beta_{T_c} J\sqrt{1 + d^2}]^{-1} = T_c^{\text{DM}} \tag{16}$$

plays the role of the critical temperature of the DM model. In addition, from Eq. (16) one has (recalling that we are considering $k_B = 1$ and $J = 1$)

$$T_c = T_c^{\text{DM}} d. \tag{17}$$

The above equation also gives the slope of the transition temperature line $T_c(d)$, as a function of d, in the $d = \infty$ limit. This feature will become clearer below, when discussing the global phase diagram.

In all the above three different regimes, we consider both SBC and FBC and compare their respective results.

A. Energy and order parameter distribution functions

In all the below data, the histograms have been analyzed within the desired temperature interval, e.g., around the cumulant crossings. We, thus, checked if the energy and order parameter distributions maintain their shapes and are free from any noise at their tails as compared to the original

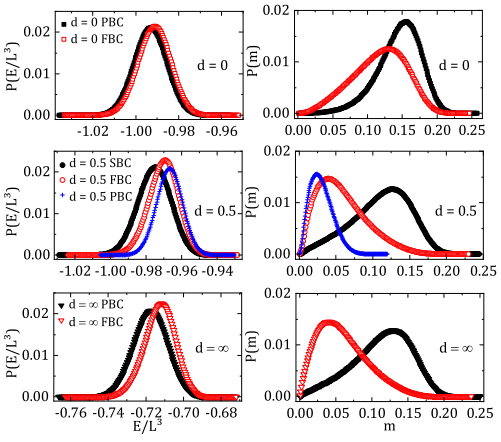

FIG. 4. Probability distributions of the energy per site $P(E/L^3)$ (left panels) and order parameter $P(m)$ (right panels) for values of d in the three chosen regimes and both SBC and FBC. The lattice size is $L = 48$ and the temperature is close to the critical temperature for each DM interaction. The middle panels for $d = 0.5$ also show the probability distribution with periodic boundary conditions (PBC). The legends on the left panels also apply to the right panels.

distributions at the temperature where the Monte Carlo simulations have been performed. As the crossing temperatures were not so far away from each other and from the temperature where the histograms were taken, and due to the sufficient amount of data from the MC simulations, no problems were observed in the distributions for any lattice sizes.

As an example, Fig. 4 show the energy per site and order parameter probability distribution function for the lattice size $L = 48$ in the three regimes of the DM interaction using both SBC and FBC. For each value of d, the probability distributions have been obtained using histograms at a temperature that is close to the critical temperature and different from the temperature where the histograms were measured. The smooth behavior of the curves shows that the temperature range is still within the region of validity. It is also clear that the shape of the distributions are indeed dependent on the type of the chosen boundary conditions.

Both $d = 0$ and $d = \infty$ are commensurate with the lattice size $L = 48$, and the use of either SBC or usual periodic boundary conditions (PBC) give the same result. The situation is different for $d = 0.5$, because there is an incommensurabilty with the lattice. The middle panels of Fig. 4 also show the corresponding probability distributions using PBC. However, the results with PBC for incommensurate lattices, shown in Ref. [32], do not produce coherent values with the expected FSS behavior. This can be clearly seen for $d = 0.5$, where $P(E/L^3)$ for PBC is clearly narrower with its χ^2 smaller than the other boundary conditions, and $P(m)$ has much smaller width and wings, resulting in much different susceptibilities and fourth-order cumulants.

B. Critical temperature T_c and fourth-order cumulant U_4^*

Figure 5 shows the order parameter fourth-order cumulants, defined in Eq. (6), as a function of the temperature T for $d = 0$, $d = 0.5$, and $d = \infty$. The temperature $T^{\rm DM}$, in the $d = \infty$ limit, is given by $T^{\rm DM} = [\beta_T J\sqrt{1+d^2}]^{-1}$. For each graph, there are two sets of curves constructed by using the histogram method and taking the data from MC simulations with SBC and FBC.

It is clear from Fig. 5 that, independent of the chosen boundary conditions, there are systematic deviations of the cumulant crossings for all considered values of d as the lattice size changes. Nevertheless, it was possible to compute the crossing temperatures $T_{\rm cross}(L, L_s)$ for $L_s = 8$, 12, 16, and 20, with $L > L_s$. The values of $T_{\rm cross}(L, L_s)$ and their error bars have been estimated by approximating the cumulants as linear functions of T in the regions where the crossings occur, with temperature steps $\Delta T = 0.0001$ (this procedure has already been used in a previous work [32] for the two-dimensional XY model). The above process has also been used in obtaining $T_{\rm cross}^{\rm DM}(L, L_s)$.

The results for the crossing temperatures $T_{\rm cross}(L, L_s)$ and $T_{\rm cross}^{\rm DM}(L, L_s)$, as a function of $[\log_{10}(L/L_s)]^{-1}$, are depicted in Fig. 6 for the three values of d and using SBC and FBC. The straight lines are fits to Eq. (7) that provide a partial estimate of the critical temperature $T_c(\infty, L_s)$. We have different scaling behaviors for different reference lattices L_s. Although for $d = 0$ the FSS functions are comparable for SBC and FBC, for $d \neq 0$ different boundary conditions lead to different scaling behavior.

Despite the difference in the scaling functions shown in Fig. 6, in all cases the extrapolated temperatures smoothly converge to a single value as the reference lattice gets larger. This convergence can be seen in Fig. 7, which depicts the $T_c(\infty, L_s)$ and $T_c^{\rm DM}(\infty, L_s)$ as a function of $1/L_s$ obtained for the values of d of Fig. 6, together with the results obtained for $d = 1$ with only SBC. One can clearly see that as L_s gets larger, the critical temperature tends to a constant, furnishing then $T_c = T_c(\infty, \infty)$, for any value of d. In the process of obtaining T_c, the smaller reference lattice $L_s = 8$ has been neglected in all cases, and an average has been made only considering the remain lattice results having values that agree within the error bars. With this process, some results come only from the largest reference lattice $L_s = 20$. The numerical results of the final critical temperature, for each value of the DM interaction of Fig. 7, are also depicted in Table I. As expected, the estimated values of T_c are the same, regardless of the type of boundary condition.

Evaluating the cumulants $U_4^*(L, L_s)$, and the corresponding errors at the crossing temperatures $T_{\rm cross}(L, L_s)$ or $T_{\rm cross}^{\rm DM}(L, L_s)$ is now straightforward using the already-computed histograms. In order to have the smallest possible errors, we have chosen the reference lattice L_s to compute the fourth-order cumulants. Figure 8 shows $U_4^*(L, L_s)$, as a function of $[\log_{10}(L/L_s)]^{-1}$, at the crossing temperatures $T_{\rm cross}(L, L_s)$. The lines are linear fits using Eq. (8), from which one gets the extrapolated cumulant $U_4^*(\infty, L_s)$. As for the crossing temperatures, different FSS behaviors occur for each reference lattice L_s and for all values of d. However, in this case, the extrapolated values of cumulants not only seem to depend

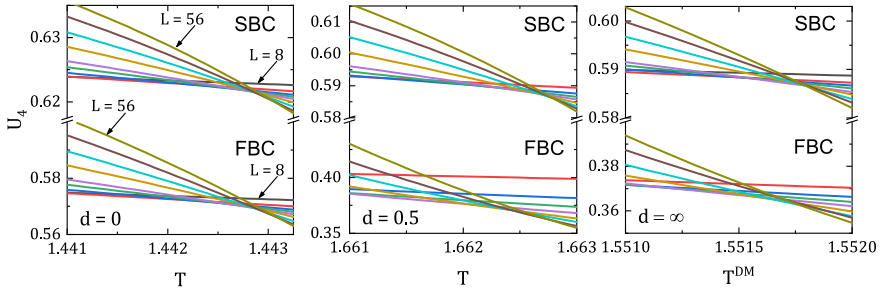

FIG. 5. Fourth-order cumulant of the order parameter U_4 as a function of temperature T for $d = 0$ (left panel), $d = 0.5$ (middle panel), and $d = \infty$ (right: where $T^{\rm DM} = [\beta_T J\sqrt{1+d^2}]^{-1}$ in the $d = \infty$ limit). The lattice sizes range from $L = 8$ to $L = 56$, as specified in the text. In each panel, the top curves are for SBC and the bottom curves are for FBC (note the different axis scale for each boundary conditions). The lattice size pattern in the left panel also applies to the other two panels.

on the boundary conditions but also whether d is zero or nonzero.

In order to better see the effects of the boundary conditions and the DM interaction on the cumulant value at the transition, Fig. 9 shows $U_4^*(\infty, L_s)$, as a function of $1/L_s$, for different values of d and also $d = 1$ with SBC. It has been performed extra linear fits to estimate U_4^*, as it can be seen by the full straight lines in Fig. 9. In this procedure, the points with $L_s = 8$ have not been taken in the fits for all of the d values and boundary condition, except for $d = 0.5$ FBC, which U_4^* was obtained from the vertical axis intercept of the straight line defined by the points with $L_s = 16$ and $L_s = 20$. For this case, the error associated with the U_4^* estimate was obtained by propagating the error from the two points used to define the straight line. For $d = 0$, the results are almost independent of L_s for both boundary conditions, and the fits yield $U_4^* = 0.6208(1)$ for SBC and $U_4^* = 0.5679(2)$ for FBC. This is clear evidence that, as in other models, the cumulant does depend on the boundary conditions [32,44].

For $d > 0$, the finite-size effects become stronger, mainly for FBC. Interestingly, with SBC, for different values of d the cumulants $U_4^*(\infty, L_s)$ clearly converge to the same result as L_s gets larger. On the other hand, despite stronger finite-size behavior for FBC, the results also seem to converge to the same result but with a different value as compared to the SBC. The corresponding final estimates of the cumulants at the transition temperature for $d > 0$ with SBC and FBC are listed in Table I. It is clear from Table I that, for any $d > 0$, the cumulants at T_c have the same value (within the error bars) with SBC. With FBC they are outside of the error bars

TABLE I. Final estimates of the critical temperature T_c, the value of the cumulant U_4^* at T_c, the critical exponent ν and the ratios β/ν, γ/ν, and α/ν, for several values of d and both SBC and FBC. $T_c^{C_{\rm peak}}$ and $T_c^{\chi_{\rm peak}}$ are also critical temperature estimates obtained from finite-size scaling analyses. Universal values are averages obtained from the top seven row data and also include the ratio $U_4^*/\nu_{\rm SBC}$ for SBC. Some results from the literature for the Heisenberg and XY models are also displayed for comparison.

d	T_c	U_4^*	ν	β/ν	γ/ν	α/ν	$T_c^{C_{\rm peak}}$	$T_c^{\chi_{\rm peak}}$
0 (SBC)	1.44293(5)	0.6208(1)	0.713(2)	0.5152(1)	1.963(6)	−0.33(7)	1.4419(6)	1.4424(4)
0 (FBC)	1.44296(2)	0.5679(2)	0.710(1)	0.5158(4)	1.969(5)	−0.25(9)	1.4420(4)	1.4428(4)
0.5 (SBC)	1.66281(1)	0.58434(9)	0.670(2)	0.5172(3)	1.997(8)	−0.18(5)	1.6621(4)	1.6629(3)
0.5 (FBC)	1.66272(3)	0.3488(2)	0.6726(7)	0.510(4)	1.984(22)	−0.23(9)	1.6629(2)	1.6630(2)
1 (SBC)	2.14692(5)	0.5854(1)	0.677(2)	0.5175(1)				
∞ (SBC)	1.55183(1)	0.5856(4)	0.674(2)	0.5186(4)	1.968(15)	−0.24(9)	1.5512(5)	1.5517(4)
∞ (FBC)	1.55181(2)	0.35836(4)	0.673(3)	0.515(1)	1.951(12)	−0.29(11)	1.5513(3)	1.5521(3)
				Our universal values				
d	U_4^* (SBC)	U_4^* (FBC)	ν	β/ν	γ/ν	α/ν	$U_4^*/\nu_{\rm SBC}$	Ref.
0	0.6208(1)	0.5679(2)	0.712(2)	0.5155(4)	1.966(4)	−0.29(6)	0.869(4)	
≠ 0	0.5851(7)	0.3536(69)	0.673(3)	0.516(3)	1.975(20)	−0.24(5)	0.872(2)	
				Heisenberg model				
0	0.6202(1)		0.7112(5)	0.5187(6)	1.963(2)	−0.188(2)	0.8727(6)	[47]
	0.6217(8)[a]		0.712(4)	0.515(5)	1.972(7)	−0.192(16)	0.873(5)	[48]
				XY model				
	0.5859(8)		0.669(6)	0.5179(24)	1.965(5)		0.876(8)	[49]
	0.5856(1)		0.6717(1)	0.5190(2)	1.9619(4)	−0.0225(5)	0.8718(2)	[50]

[a]From Ref. [40].

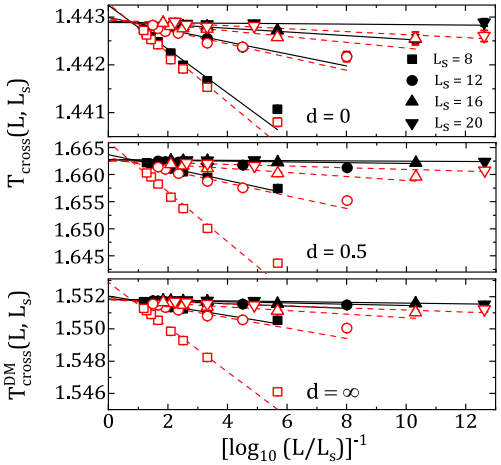

FIG. 6. Crossing temperatures $T_{cross}(L, L_s)$ and $T^{DM}_{cross}(L, L_s)$, as a function of $[\log_{10}(L/L_s)]^{-1}$, for $d = 0$ (top panel), $d = 0.5$ (middle panel), and $d = \infty$ (bottom panel). Different symbols correspond to different reference sizes L_s. Full symbols and full lines correspond to SBC, while open symbols and dashed lines to FBC. Both types of lines are linear fits according to Eq. (7). The legend in the top panel also applies to the other panels. Where not shown, the error bars are smaller than the symbol sizes.

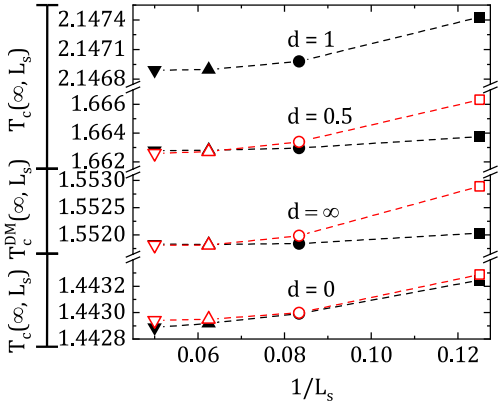

FIG. 7. Extrapolated values of the crossing temperatures $T_{cross}(\infty, L_s)$ and $T^{DM}_{cross}(\infty, L_s)$ from the fits of Fig. 6, as a function of $1/L_s$, for different DM interaction d. SBC correspond to full symbols and FBC to open symbols. The case $d = 1$ with only SBC has also been added in this figure. The temperature axis has different scales for different values of d. The error bars are smaller than the symbol sizes.

but still quite comparable. However, U_4^* for SBC and FBC are definitely different from each other. An average furnishes $U_4^* = 0.5851(7)$ for SBC and $U_4^* = 0.3536(69)$ for FBC. These results suggest that as soon as the DM interaction is present, the model changes its universality class. To check this point more carefully, the computation of critical exponents is valuable.

C. Critical exponent ν and β/ν ratio

The critical exponent ν and the ratio β/ν can be obtained from the simulations by using the already-computed histograms and relations (9) and (10). The top left and bottom left panels in Fig. 10 show, respectively, the derivative $dU_4(\beta_T; L)/d\beta_T$ and the order parameter m at T_c, both as a function of the lattice size L (the axes are in base-10-logarithmic scale and this base has been kept in other log-log plots that are shown ahead in the text). From the scaling relations, one expects the slopes to furnish ν in the former case and β/ν in the latter case. However, although not completely apparent in Fig. 10, in some cases, residual finite-size effects are still present. To better estimate the critical exponents, several linear fits have been made by progressively discarding the smaller lattices. With L_s now the smallest lattice size considered in the linear fit, we were able to get a good estimate of the critical exponents from $L_s = 8$ to $L_s = 32$. The corresponding results, as a function of $1/L_s$, are depicted in the right panels of Fig. 10, where it is easier to see that, in general, the finite-size effects are stronger for $d > 0$ and for FBC. These effects are more pronounced for $d = 0.5$ with FBC. The full lines in the right panels of Fig. 10 are additional linear fits to get the final estimate of the exponent.

As an example, for $d = 0$ (see the top right panel in Fig. 10), the extrapolated value of the correlation length critical exponent is $\nu = 0.713(2)$ with SBC and $\nu = 0.710(1)$

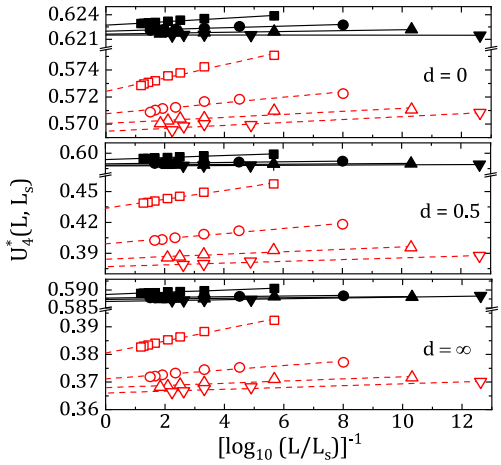

FIG. 8. Value of the cumulants $U_4^*(L, L_s)$, at the crossing temperatures $T_{cross}(L, L_s)$ or $T^{DM}_{cross}(L, L_s)$, as a function of $[\log_{10}(L/L_s)]^{-1}$, computed from the simulations on the reference lattice of size L_s. The description of DM interaction, symbols, and lines given in Fig. 6 also applies to this figure [with the linear fits coming from Eq. (8) instead]. The error bars are smaller than the symbol sizes.

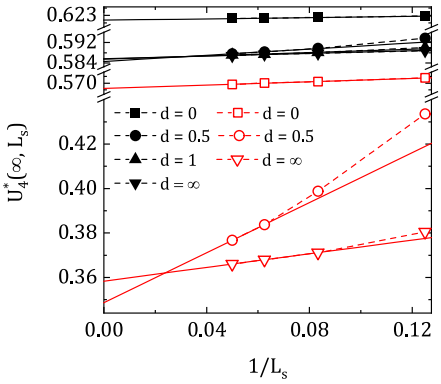

FIG. 9. Extrapolated values of the cumulants $U_4^*(\infty, L_s)$ from the fits of Fig. 8, as a function of $1/L_s$, for different DM interaction d (here represented by different symbols) and SBC (full symbols) and FBC (open symbols). The case $d = 1$ with only SBC has also been added in this figure. The cumulant axis has different scales for different values of d as well as for different boundary conditions. The full lines are linear fits, except for $d = 0.5$ FBC, which the straight line is defined by the two points that it passes through them. The dashed lines are just guides to the eye and the error bars are smaller than the symbol sizes.

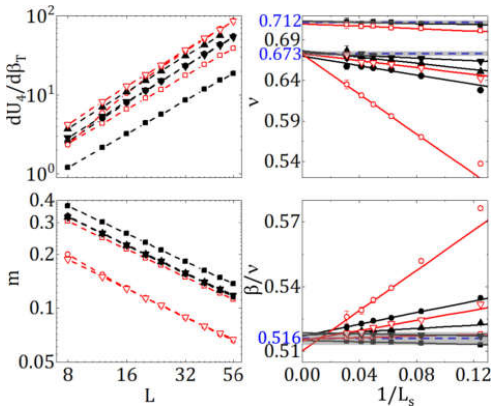

FIG. 10. Derivative of the order parameter fourth-order cumulant $dU_4(\beta_T; L)/d\beta_T$ (top left panel) and order parameter m (bottom left panel), both as function of the lattice size L and evaluated at $T = T_c$. In the left panels the axes scales are base-10-logarithmic and the dashed lines are just a guide to the eye. The linear fits, as described in the text, are shown for the critical exponent ν in the top right panel, and the ratio β/ν in the bottom right panel, as function of $1/L_s$ (L_s here means the smallest considered lattice size), where full lines are additional linear fits. Horizontal dashed-lines in the two right panels indicate the mean values with the shaded area giving an idea of the error bars. The legends of Fig. 9 also apply in this case.

with FBC. As expected, ν should be independent of the boundary conditions. The present estimate gives $\nu = 0.712(2)$. It is interesting to see that for $d > 0$, all the extrapolations tend to the same result, independent of the values of d and the type of boundary conditions. The corresponding average, represented by the horizontal dashed line in the top right panel in Fig. 10, gives $\nu = 0.673(3)$. This means, indeed, that the DM interaction does change the universality class of the model, as was suggested by the computation of the fourth-order cumulant in the previous subsection.

It is remarkable the extrapolations obtained for the ratio β/ν depicted in the bottom right panel of Fig. 10. Although for $d = 0.5$ and FBC we probably still need larger lattices with more MCS (which will take much more computational effort), for all the cases the extrapolations converge to the same region. This provides an estimate $\beta/\nu = 0.5155(4)$ for $d = 0$ and $\beta/\nu = 0.516(3)$ for $d \neq 0$, suggesting that besides having different exponents, the system satisfies the so-called weak universality class, where the exponents are different but their ratios are the same [45,46]. The final estimates of these critical exponents are listed in Table I.

In order to further seek whether the weak universality class really holds for this model, we have also computed the ratio γ/ν and α/ν by using less CPU time.

D. γ/ν and α/ν ratios

The order parameter susceptibility χ and the specific heat C have been obtained with less computational effort, as outlined by the second approach in Sec. III D, at the cost of having less precise data. Only one simulation comprising a total of 10^6 MCS after relaxation, generating 10^5 data points, was performed at temperature intervals $\Delta T = 0.001$ or $\Delta T = 0.0005$ close to the region of maximum values of the susceptibility and specific heat. In this way, for each lattice size L, not only χ_{peak} and C_{peak} have been obtained but also the corresponding temperatures where these peaks occur. It was also possible to simulate the $L = 64$ lattice for $d = 0$, 0.5, and $d = \infty$ with SBC and FBC.

The FSS behavior of χ and C are expressed by Eqs. (11) and (12). The peak temperature T_{peak}, where T_{peak} can be either $T_{\chi_{\text{peak}}}$ or $T_{C_{\text{peak}}}$ has, for large-enough systems, a finite-size scaling relation given by [40,41]

$$T_{\text{peak}} \approx T_c + bL^{-1/\nu}, \tag{18}$$

where b is a nonuniversal constant.

Figure 11 shows the peak temperature, T_{peak}, as a function of $L^{-1/\nu}$, obtained from the susceptibility and specific heat for different values of d and boundary conditions. The ν exponents have been taken from the final universal ones in Table I. For $d = 0$, $\nu = 0.712$ and for all values $d \neq 0$, $\nu = 0.673$. In each data set, two linear fits have been made, one with all lattices and another one neglecting the smallest lattice $L = 8$. When the linear fits are quite different, which are apparent only for some cases in Fig. 11, the estimates come from fits neglecting the smallest lattice size. The corresponding results are displayed in Table I. It can be seen that the critical temperature from the susceptibility and specific heat are, for all values of d and to within the error bars, in agreement

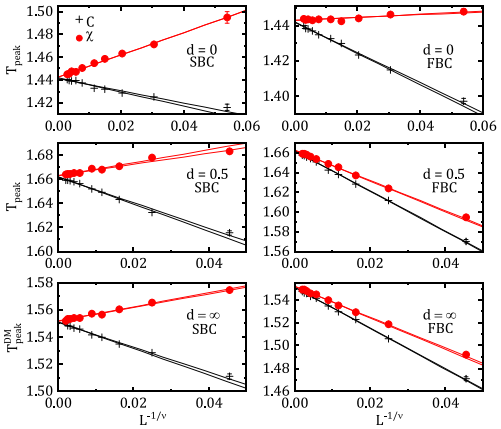

FIG. 11. Peak temperatures T_{peak} and $T^{\text{DM}}_{\text{peak}}$ of the susceptibility (circles) and specific heat (crosses) as a function of $L^{-1/\nu}$ for different values of d and respective boundary conditions. The exponents $\nu = 0.712(2)$ for $d = 0$ and $\nu = 0.673(3)$ for $d \neq 0$ are those obtained in this work and displayed in Table I. For each data set there are two lines coming from linear fits, one considering all lattices and another neglecting the smallest lattice size. The error bars are smaller than the symbol sizes.

with each other and also in agreement with the values of T_c obtained from the cumulant crossings.

Figure 12 shows the logarithm of the order parameter susceptibility peak χ_{peak} as a function of the logarithm of the lattice size L for different values of d. The slope of each data set furnishes, according to Eq. (11), the ratio γ/ν. In this case,

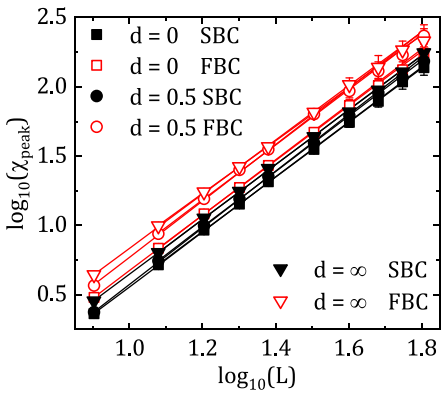

FIG. 12. Logarithm of the order parameter susceptibility peak χ_{peak} as a function of the logarithm of the lattice size L for different values of d with the boundary conditions specified in the legend. There are two lines corresponding to linear fits, one with all data and another neglecting the smallest lattice size. The error bars are smaller than the symbol sizes when they are not visible.

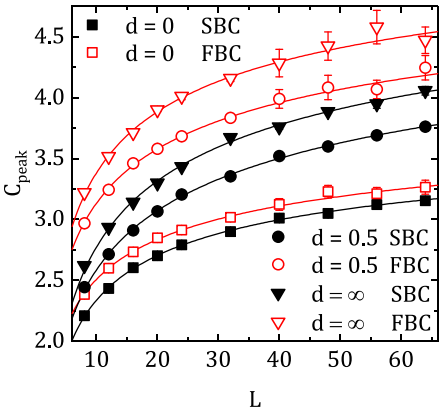

FIG. 13. Specific heat peak C_{peak}, as a function of the lattice size L, for different values of d with the boundary conditions specified in the legend. Full lines are nonlinear fits according to Eq. (12) and considering all data for each value of d. The error bars are smaller than the symbol sizes when they are not visible.

due to the shorter MC runs, it is not possible to do the same analysis as for β/ν. Nevertheless, for all values of d the slopes from the fits neglecting the smaller lattice size $L = 8$ are close together, and the mean value is listed in Table I.

The specific heat peaks, as a function of L, for the same values of d are shown in Fig. 13. It is clear that α is negative, since C goes to a constant as $L \to \infty$. The full lines in Fig. 13 are fits using Eq. (12) and considering all data points. The corresponding values for d different from zero have been averaged and are displayed in Table I. For comparison, the ratios α/ν for $d = 0$ with SBC and FBC have also been averaged and given in this same table.

E. Structure factor

The structure factor, $\mathcal{S}(\mathbf{q})$, has been measured for the same values of d as before using single simulations as described in the previous subsection. Lattice sizes $L = 8$, 12, 16, 20, and 24 have been used with SBC and FBC. The temperatures were T_c for each value of d. The pair-correlation functions $\Gamma(\mathbf{r}_{jk})$ have been estimated at the final of the simulation, with their corresponding uncertainties. In this way, $\mathcal{S}(\mathbf{q})$ can be calculated, as a function of any arbitrary wave vector $\mathbf{q}$, through Eq. (15). Here $\mathbf{q}$ is measured in radians per lattice spacing, with the lattice spacing being defined as unity. The uncertainty in the structure factor has been estimated from the error propagation coming from $\Gamma(\mathbf{r}_{jk})$.

As an example, the static structure factor $\mathcal{S}(\mathbf{q})$ is shown in Fig. 14 for wave vectors in the q_x-q_y plane for a lattice with size $L = 20$ at $T = T_c$ for various values of d. The same pattern is obtained when the wave vector lies either in the q_x-q_z or q_y-q_z planes. The intensity of the peaks, as well as their width, is indicated by the gradient scale on the right of each graph. Note that the peaks in $\mathcal{S}(\mathbf{q})$ occur at $q_x = q_y = \pm\phi$, where ϕ is the pitch angle. As one can see from the gradient intensities in

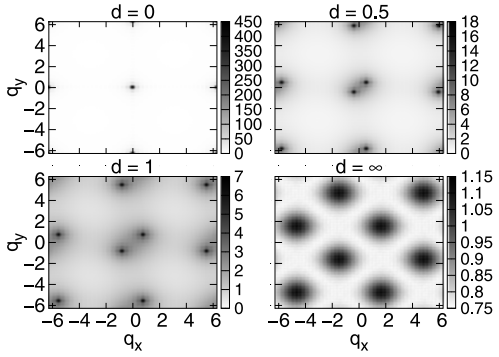

FIG. 14. Structure factor $\mathcal{S}(\mathbf{q})$ for the wave vector in the q_x-q_y plane with $q_z = 0$ and $T = T_c$ for different values of d. The lattice size is $L = 20$ and SBC has been used in the MC simulations. The intensity of $\mathcal{S}(\mathbf{q})$ is given by the gradient scale on the right side of each figure.

Fig. 14, the height of the peaks gradually decrease, with their widths becoming wider, as d increases from $d = 0$, ending up with the most spreading values, close to unity, for $d = \infty$.

In order to extract more quantitative results from these calculations, we have checked if there is any finite-size scaling of the maximum value of $\mathcal{S}(\phi, \phi, 0)$ on the system size L. The graph on the top panel in Fig. 15 shows, for the same d values considered in Fig. 14, a plot of the peak of $\mathcal{S}(\phi, \phi, 0)$, as a function of $L = 8$, 12, 16, 20, and 24, where both axes are logarithmic. In this case, we have also included some results from simulations with FBC performed at $T = T_c$. As it is expected, the model without DM interaction ($d = 0$ and $\phi = 0$) exhibits the usual long-range magnetic ordering along the planes in the lattice, as it can be clearly seen in the behavior of $\mathcal{S}(0, 0, 0)$ that increases as L increases and tends to infinity in the thermodynamic limit. However, for $d \neq 0$, the peaks $\mathcal{S}(\phi, \phi, 0)$ do not show any regular increase as L increases. Instead, the points tend to saturate or fluctuate around a horizontal line. This means that looking at x-y, x-z, and y-z planes in the lattice, one does not observe any long-range magnetic ordering.

On the other hand, it is interesting to analyze $\mathcal{S}(\mathbf{q})$ when $\mathbf{q} = \pm(\phi, \phi, \phi)$, a wave vector being parallel to the diagonal direction of the lattice or, in terms of crystallographic definitions, the [111] direction in a simple cubic lattice. The corresponding peaks of $\mathcal{S}(\mathbf{q})$ at $T = T_c$, as a function of L, in logarithmic scales, are shown in the bottom panel of Fig. 15. The two curves for $d = 0$ have not changed their behavior in relation to those in the upper panel. However, for all of the remaining curves with $d \neq 0$, $\mathcal{S}(\phi, \phi, \phi)$ follow now the same trend as for $d = 0$, namely increasing with L and diverging to infinity in the thermodynamic limit. In other words, the magnetic long-range ordering for $d \neq 0$ is observed when the wave vector $\mathbf{q}$ is oriented along the diagonal directions with specific values that depend on d through the pitch angle ϕ. This result agrees with a theoretical finding for this model [21], which shows that the magnetization changes in a spiral

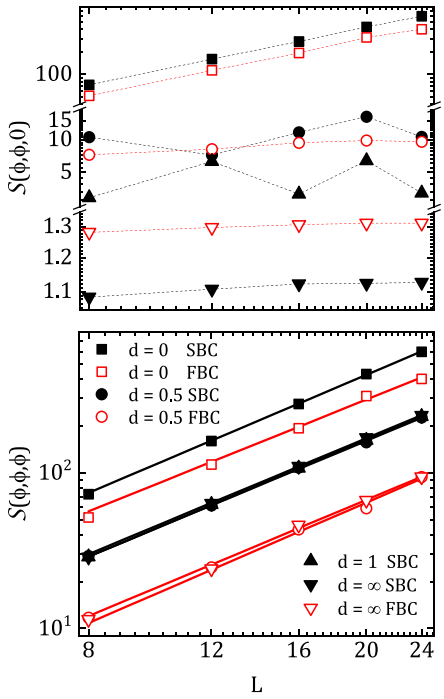

FIG. 15. Peak values of the static structure factor $\mathcal{S}(\mathbf{q})$, for wave vectors $\mathbf{q} = \pm(\phi, \phi, 0)$ (upper panel) and $\mathbf{q} = \pm(\phi, \phi, \phi)$ (bottom panel), as a function of the lattice size L. The results are at $T = T_c$ for each d indicated in the legends (valid also for the top panel). Both axes are base-10-logarithmic. Dashed lines are only guides for the eye while solid lines are linear fits to the data. The error bars are smaller than the symbol sizes.

way with rotations around the z axis with a wave vector $\mathbf{q} = \pm(\phi, \phi, \phi)$.

It is also remarkable that all curves in the bottom graph of Fig. 15 follow a power law and are almost parallel to each other. In fact, by the static structure factor definition in Eq. (15), one can verify that $\mathcal{S}(\phi, \phi, \phi) \approx \mathcal{S}_0 L^{\gamma/\nu}$ when $T = T_c$. Although the lattice sizes in this case are not as large as those used in the susceptibility and specific heat peaks analysis, we have additionally performed linear fits to all data in the bottom panel of Fig. 15. The estimate from the average is $\gamma/\nu = 1.9(1)$, in good agreement with the previous values from the order parameter susceptibility of the last section (despite the larger error due to the less statistics in this case).

The oscillations present in $\mathcal{S}(\phi, \phi, 0)$ as a function of L, depicted in the top panel of Fig. 15, deserve more attention. So in order to obtain extra insight about the $\mathcal{S}(\mathbf{q})$ behavior as a function of $\mathbf{q}$, ϕ and L, we defined the quantity $\widetilde{\mathcal{M}}(\mathbf{q}) = \| \sum_{j=1}^{L^3} \mathbf{S}_j e^{-i\mathbf{q}\cdot\mathbf{r}_j} \| / L^3$, analogously to an order parameter, although assuming complex values (the two double-vertical bars on the right hand side in the above equation represent

the vector modulus). Then, the structure factor is given by $\mathcal{S}(\mathbf{q}) = L^3|\widetilde{\mathcal{M}}(\mathbf{q})|^2$, where the vertical bars refer to the modulus of the complex $\widetilde{\mathcal{M}}(\mathbf{q})$.

Considering the ground-state spin configuration, the structure factor for a lattice size L can be written in analytical form,

$$\mathcal{S}(\mathbf{q}) = \frac{1}{2L^3}\prod_{j=1}^{3}\left(\left\{\frac{\sin[(\phi+q_j)L/2]}{\sin[(\phi+q_j)/2]}\right\}^2 + \left\{\frac{\sin[(\phi-q_j)L/2]}{\sin[(\phi-q_j)/2]}\right\}^2\right), \tag{19}$$

where the index $j = 1, 2, 3$ labels the x, y, and z wavevector components, respectively. In the case $\mathbf{q} = \pm(\phi, \phi, 0)$, Eq. (19) simplifies into

$$\mathcal{S}(\phi,\phi,0) = \frac{1}{2L^3}\left\{\left[\frac{\sin(L\phi)}{\sin\phi}\right]^4 + L^4\right\}\left[\frac{\sin(L\phi/2)}{\sin(\phi/2)}\right]^2. \tag{20}$$

Figure 16 is a plot of the above structure factor for $d = 0.5$, 1, and ∞ as a function of L, both quantities on logarithmic scale. It is patent the similarity of the data at $T = 0$ with those obtained at $T = T_c$ depicted in the top panel of Fig. 15. Nevertheless, here it becomes easier to understand the oscillations as L changes, because the structure factor is zero whenever $\sin(L\phi/2) = 0$. One can still infer that one has a FSS behavior for lattices that are commensurate with the pitch angle and a different FSS for incommensurate lattices. This is clearly seen for $d = 1$ and $d = \infty$, the latter one being valid for all data because all lattice sizes are commensurate with the pitch angle. However, for $d = 0.5$, none of the L values turn out to be commensurate and the data do not follow any special scaling.

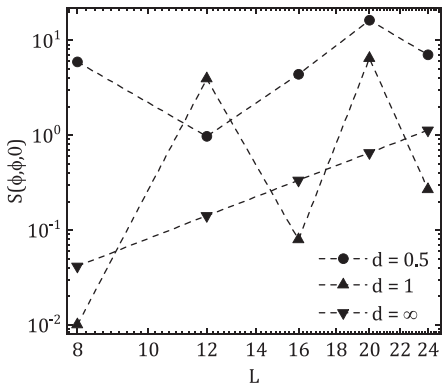

FIG. 16. Peak values of the static structure factor $\mathcal{S}(\mathbf{q})$, for wave vector $\mathbf{q} = \pm(\phi, \phi, 0)$ as a function of lattice size L according to Eq. (20). The results are at $T = 0$ for each d shown in the legend. Both axes are base-10-logarithmic. Dashed lines are only guides to the eyes.

Finally, for the wave vector $\mathbf{q} = \pm(\phi, \phi, \phi)$, Eq. (19) results in

$$\mathcal{S}(\phi,\phi,\phi) = \frac{1}{2L^3}\left\{\left[\frac{\sin(L\phi)}{\sin\phi}\right]^6 + L^6\right\}, \tag{21}$$

which does not have any zeros for $L > 0$ and increases as L^3.

F. Phase diagram

Still shorter simulations were done just to locate the transition temperature for further values of d. These transitions have been estimated using cumulant crossings between lattices $L = 32$ and $L = 24$ only, with SBC (FBC gives similar estimates). Although such estimates are, in fact, underestimated in comparison to that for the infinite system, the error in the values of T_c are relatively small when viewed in the whole temperature range under consideration. With this additional data it is possible to have a good picture of the global phase diagram in the T-d plane as depicted in Fig. 17.

The main figure shows the reduced temperature $T_c(d)/T_c^{\mathrm{DM}}$ as a function of d. With this definition, the asymptotic behavior of $T_c(d)/T_c^{\mathrm{DM}}$, in the $d = \infty$ limit (given by the dashed

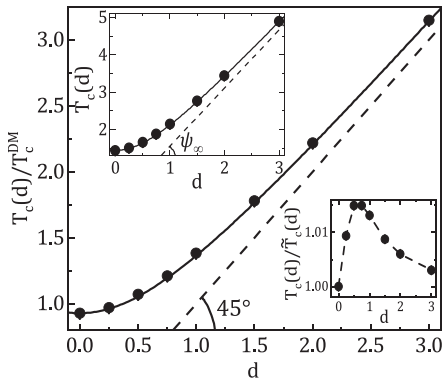

FIG. 17. Phase diagram in the temperature versus DM interaction plane. The circles are the present results and the full lines are fits to a hyperbolic function as described in the text. The dashed lines are the slopes of the transition lines in the limit $d = \infty$. The main graph shows the normalized transition temperature $T_c(d)/T_c^{\mathrm{DM}}$, where the asymptote slope is 45°. The top inset gives $T_c(d)$, where the asymptote slope is ψ_∞. The bottom inset shows the ratio $T_c(d)/\widetilde{T}_c(d)$. The error bars are smaller than the symbol sizes.

line), has a declivity of 45°. The top inset shows $T_c(d)$ as a function of d for comparison. In this case, the asymptotic behavior of the transition line is such that $\tan\psi_\infty = T_c^{\rm DM}$.

It is well known that the XY model with DM interaction has an exact hyperbolic expression for the critical temperature, as a function of DM interaction, that depends only on the critical temperature for $d = 0$ [32,35]. To test whether such behavior also applies to the Heisenberg model, we have performed a fit of the ratio $T_c(d)/T_c^{\rm DM}$ to a branch of a hyperbola defined as

$$\widetilde{T}_c(d) = T_c^{\rm DM}\sqrt{r^2 + d^2}, \tag{22}$$

$$r = \frac{T_c(0)}{T_c^{\rm DM}}, \tag{23}$$

where $T_c(0)$ is the critical temperature of the Heisenberg model and r is the only adjustable parameter. The full line in the upper inset in Fig. 17 is given by setting $T_c(0) = 1.44293(5)$ and $T_c^{\rm DM} = 1.55183(1)$ (see Table I), resulting in $r = 0.92982(3)$. The fit in the main graph, shown as a full line, gives $r = 0.92982(7)$. Naturally, the data do not follow a hyperbolic function, as can be seen in the bottom inset. It shows that the ratio $T_c(d)/\widetilde{T}_c(d)$ has a systematic deviation, with the largest deviation around $d \approx 0.625$ and asymptotically decreasing to unity as d tends to infinity. However, the fitted line can give good estimates of the critical temperature for any different values of the DM interaction d.

V. CONCLUDING REMARKS

The main results of the present Monte Carlo study of the Heisenberg model with DM interaction are conveyed in Table I. The first comparison is for the model with d=0, where there are ample results in the literature for the isotropic Heisenberg model from different techniques, including experimental measurements of the critical exponents. The transition temperature, in this case $T_c = 1.44295(3)$, is in excellent agreement with previous MC simulations, e.g., $T_c = 1.442987(1)$ [48] and $T_c = 1.44293(6)$ [51].

Unlike the critical temperature and critical exponents, the fourth-order cumulant of the order parameter depends on the boundary conditions. From an analysis of the universal quantities given in Table I, it is also apparent that the critical exponents along the transition line for $d > 0$ are different from the isotropic Heisenberg model. However, as the ratio of the critical exponents and the cumulants are the same, to within the error bars, it is evident that *weak universality* holds for the Heisenberg model with DM interaction. Moreover, from a comparison of the exponents for $d > 0$ and those in the literature for the XY model, it is evident that the Heisenberg model with DM interaction is in the same weak universality class as the XY model [19–21].

Additional numerical comparison to other MC simulations as well as different approximation methods can be found in Refs. [52,53].

ACKNOWLEDGMENTS

This work has been partially funded by CNPq, CAPES, and FAPEMIG (Brazilian agencies) and computationally supported, in part, by resources and technical expertise from the Georgia Advanced Computing Resource Center (GACRC), a partnership between the University of Georgia's Office of the Vice President for Research and Office of the Vice President for Information Technology. We also acknowledge Prof. Gerald Weber for the invaluable assistance in the use of the Statistical Mechanics Computer Lab facilities at UFMG.

[1] W. Heisenberg, Z. Phys. **49**, 619 (1928).
[2] R. A. Erickson, Phys. Rev. **90**, 779 (1953).
[3] A. S. Borovik-Romanov and M. P. Orlova, Sov. Phys. JETP **4**, 531 (1957).
[4] T. Matsubara and H. Matsuda, Prog. Theor. Phys. **16**, 569 (1956).
[5] T. Moriya, Phys. Rev. Lett. **4**, 228 (1960).
[6] A. Crépieux and C. Lacroix, J. Magn. Magn. Mater. **182**, 341 (1998).
[7] M. Uchida, Y. Onose, and Y. Matsui, Science **311**, 359 (2006).
[8] Y. Kousaka, S.-I. Yano, J.-I. Kishine, Y. Yoshida, K. Inque, K. Kikushi, and J. Akimitsu, J. Phys. Soc. Jpn. **76**, 123709 (2007).
[9] S. M. Stishov and A. E. Petrova, Phys. Usp. **54**, 1117 (2011).
[10] J. Kishine and A. S. Ovchinnikov, *Theory of Monoaxial Chiral Helimagnet*, edited by R. E. Camley and R. L. Stamps, Solid State Physics Vol. 66 (Academic Press, San Diego, CA, 2015), pp. 1–130.
[11] M. Bode, M. Heide, K. V. Bergmann *et al.*, Nature (Lond.) **447**, 190 (2007).
[12] P. Ferriani, K. von Bergmann, E. Y. Vedmedenko, S. Heinze, M. Bode, M. Heide, G. Bihlmayer, S. Blugel, and R. Wiesendanger, Phys. Rev. Lett. **101**, 027201 (2008).
[13] S. V. Grigoriev, Y. O. Chetverikov, D. Lott, and A. Schreyer, Phys. Rev. Lett. **100**, 197203 (2008).
[14] W. Jiang, G. Chen, K. Liu, J. Zang, S. G. E. te Velthuis, and A. Hoffmann, Phys. Rep. **704**, 1 (2017).
[15] B. Göbel, I. Mertig, and O. A. Tretiakov, Phys. Rep. **895**, 1 (2021).
[16] H. Yang, J. Liang, and Q. Cui, Nat. Rev. Phys. **5**, 43 (2023).
[17] Y. Tokunaga, T. Kimura, and T.-H. Arima, J. Phys. Soc. Jpn. **92**, 081008 (2023).
[18] T. Tolinski and K. Synoradzki, Intermetallics **47**, 1 (2014).
[19] J. H. H. Perk and H. W. Capel, Phys. Lett. A **58**, 115 (1976).
[20] M. Calvo, J. Phys. C: Solid State Phys. **14**, L733 (1981).
[21] L. Klein and A. Aharony, Phys. Rev. B **44**, 856 (1991).
[22] K. Y. Ho, T. R. Kirkpatrick, Y. Sang, and D. Belitz, Phys. Rev. B **82**, 134427 (2010).
[23] V. Laliena, J. Campo, and Y. Kousaka, Phys. Rev. B **94**, 094439 (2016).
[24] F. Azizi and H. Rezania, Physica E **114**, 113603 (2019).
[25] S. D. Yi, S. Onoda, N. Nagaosa, and J. H. Han, Phys. Rev. B **80**, 054416 (2009).
[26] A. Hamann, D. Lamago, T. Wolf, H. v. Löhneysen, and D. Reznik, Phys. Rev. Lett. **107**, 037207 (2011).
[27] S. Buhrandt and L. Fritz, Phys. Rev. B **88**, 195137 (2013).
[28] M. Shinozaki, S. Hoshino, Y. Masaki, J. Kishine, and Y. Kato, J. Phys. Soc. Jpn. **85**, 074710 (2016).

[29] Y. Nishikawa and K. Hukushima, Phys. Rev. B **94**, 064428 (2016).
[30] A. M. Belemuk and S. M. Stishov, Phys. Rev. B **95**, 224433 (2017).
[31] H. Liu, J. A. Plascak, and D. P. Landau, Phys. Rev. E **97**, 052118 (2018).
[32] G. A. Silva, J. A. Plascak, and D. P. Landau, Phys. Rev. E **106**, 044116 (2022).
[33] M. Elhajal, B. Canals, R. Sunyer, and C. Lacroix, Phys. Rev. B **71**, 094420 (2005).
[34] E. Y. Vedmedenko, L. Udvardi, P. Weinberger, and R. Wiesendanger, Phys. Rev. B **75**, 104431 (2007).
[35] F. C. Alcaraz and W. F. Wreszinski, J. Stat. Phys. **58**, 45 (1990).
[36] N. Metropolis, A. W. Rosenbluth, M. N. Rosenbluth *et al.*, J. Chem. Phys. **21**, 1087 (1953).
[37] W. H. Press, S. A. Teukolsky, W. T. Vetterling, and B. P. Flannery, *Numerical Recipes in C: The Art of Scientific Computing*, 2nd ed. (Cambridge University Press, Cambridge, UK, 1988 and 1992).
[38] P. Olsson, Phys. Rev. Lett. **73**, 3339 (1994).
[39] K. Binder, Z. Phys. B: Condens. Matter **43**, 119 (1981).
[40] C. Holm and W. Janke, Phys. Rev. B **48**, 936 (1993).
[41] D. P. Landau and K. Binder, *A Guide to Monte Carlo Simulation in Statistical Physics*, 5th ed. (Cambridge University Press, Cambridge, UK, 2021).
[42] W. Zhu, S.-S. Gong, and D. N. Sheng, Proc. Natl. Acad. Sci. USA **116**, 5437 (2019).
[43] R. Yadav, S. Nishimoto, M. Richter, J. van den Brink, and R. Ray, Phys. Rev. B **100**, 144422 (2019).
[44] W. Selke, Eur. Phys. J. B **51**, 223 (2006).
[45] M. Suzuki, Prog. Theor. Phys. **51**, 1992 (1974).
[46] N. Khan, P. Sarkar, A. Midya, P. Mandal, and P. K. Mohanty, Sci. Rep. **7**, 45004 (2017).
[47] M. Campostrini, M. Hasenbusch, A. Pelissetto, and P. Rossi, and E. Vicari, Phys. Rev. B **63**, 214503 (2001).
[48] Y. Nonomura and Y. Tomita, Phys. Rev. E **93**, 012101 (2016).
[49] M. Krech and D. P. Landau, Phys. Rev. B **60**, 3375 (1999).
[50] M. Campostrini, M. Hasenbusch, A. Pelissetto, and E. Vicari, Phys. Rev. B **74**, 144506 (2006).
[51] K. Chen, A. M. Ferrenberg, and D. P. Landau, Phys. Rev. B **48**, 3249 (1993).
[52] A. Pelissetto and E. Vicari, Phys. Rep. **368**, 549 (2002).
[53] W. Xu, Y. Sun, J.-P. Lv, and Y. Deng, Phys. Rev. B **100**, 064525 (2019).